MIB
MESTRADO INTEGRADO EM BIOENGENHARIA
ENGENHARIA BIOMÉDICA

Endoscopic Image Analysis of Aberrant Crypt Foci

Ana Priscila Vieira Alves

Universidade do Porto

Faculdade de Engenharia

FEUP

2011

Faculdade de Engenharia da Universidade do Porto

Endoscopic Image Analysis of Aberrant Crypt Foci

Ana Priscila Vieira Alves

Supervisor: Prof. João Manuel R. S. Tavares

Departamento de Engenharia Mecânica
Faculdade de Engenharia da Universidade do Porto

Dissertation Report

Integrated Master in Bioengineering

July, 2011

AGRADECIMENTOS

Terminar esta dissertação é muito mais do que finalizar um trabalho de faculdade. É o fim de um percurso de 5 anos ricos em experiências, descobertas e crescimento. Queria, por isso, deixar aqui umas palavras de gratidão às pessoas que percorreram este caminho de aprendizagem e perseverança ao meu lado.

Em primeiro lugar gostaria de agradecer ao Prof. Doutor João Manuel R.S. Tavares, pela disponibilidade e orientação não só deste trabalho, como também do projecto e monografia desenvolvidos neste último ano lectivo.

Em segundo lugar, um agradecimento especial à minha companheira de curso, Inês Odila Pereira, pela partilha de ideias, pelo companheirismo e amizade, pelos disparates e risadas, e pelo apoio em momentos de angústia, ansiedade e nervosismo.

À Célia Cruz e Andreia Silva um muito obrigada pela paciência, suporte, sugestões e momentos variados e ao Bruno Pinto pelo apoio informático intensivo em horas críticas.

Pelos almoços às 12h, pelos momentos de alegria e diversão, de cultura, de picnics à chuva e muito mais, queria agradecer a todos os pioneiros do MIB que comigo caminharam durante 5 anos, na procura de sempre mais e melhor. A todos os meus amigos, um muito obrigado porque vocês preenchem a minha vida e me fazem feliz.

À Oficina de Música da FEUP, uma palavra especial de agradecimento pelos momentos de descontracção às terças-feiras.

Ao meu avô Cláudio deixo aqui uma palavra de agradecimento pelas palavras de incentivo, pelo cuidado e preocupação.

Finalmente, uma palavra especial para os meus pais, Vítor e Raquel, pela paciência nos momentos mais difíceis, pelo apoio constante, pelo carinho e amor. São e sempre serão a minha fonte de inspiração!

RESUMO

Actualmente, o cancro é uma das doenças mais problemáticas, sendo responsável pela morte de cerca de 1.7 milhões de pessoas por ano. O cancro colorectal representa a segunda maior taxa de incidência de cancro em Portugal, mas, se detectada cedo, a morte pode ser evitada.

Pensa-se que os focos de criptas aberrantes (ACF) podem ter um papel importante na sequência adenoma-carcinoma, sendo um precursor do cancro colorectal. O seu reconhecimento através de imagens endoscópicas pode potenciar a sua detecção e diagnóstico. No entanto, a observação das imagens de diagnóstico é realizada manualmente por um médico especializado, tornando o processo muito demorado e sujeito a erros. Como tal, técnicas computacionais de processamento e análise de imagem são ferramentas importantes que podem ser usadas para facilitar e aumentar a eficiência de tal tarefa.

O objectivo principal desta dissertação foi estudar e implementar metodologias computacionais para detectar ACF em imagens adquiridas *in vivo* através de endoscopia.

Em primeiro lugar, foram testadas diversas técnicas de melhoramento de imagem, sendo concluído que a aplicação de um filtro mediana em conjunto com *Histogram Stretching* potencia a eliminação de ruído de alta frequência e aumenta o contraste da imagem original.

De seguida, foram testados diversos algoritmos de segmentação baseados nas fronteiras do objeto de interesse, em regiões e no histograma. Nenhuma técnica testada foi capaz de detectar unicamente os ACF. No entanto, o Canny edge detector e watershed conseguiram delimitar os focos e o método de contornos activos (*snakes*) mostrou-se promissor na delimitação das fronteiras dos ACF, embora com algumas limitações devido à difícil adaptação dos parâmetros para diferentes imagens.

Em suma, com base neste estudo poderão ser desenvolvidas novas técnicas, nomeadamente tirando partido das cores das imagens endoscópicas, ou ajustando os algoritmos para esta aplicação em específico.

Palavras-Chave: Cancro Colorectal, Focos de Criptas Aberrantes, Processamento e Análise de imagem, Melhoramento de Imagem, Segmentação de Imagem

ABSTRACT

Currently, cancer is one of the most problematic diseases, being responsible for the deaths of about 1.7 million people per year. The colorectal cancer represents the second highest incidence rate of cancer in Portugal, but it can be avoided if early detected.

It is believed that aberrant crypt foci (ACF) have a crucial role in the sequence adenoma-carcinoma, being a precursor of colorectal cancer. As such, its recognition through endoscopic images can potentiate the detection and diagnosis of this type of cancer. However, the observation of the images is usually done manually by a physician, making the process very time consuming and prone to errors. As such, the computational techniques of image processing and analysis are important tools that could be used to reduce this time and attain more efficient results.

The aim of this Dissertation was to study and implement computational methodologies that allow the detection of ACF of images captured *in vivo* by endoscopy.

At first, several techniques of image enhancement were tested, and it was concluded that the hybrid application of a median filter and histogram stretching potentiate the high intensity noise elimination and increases the image contrast.

Afterwards, various segmentation algorithms were used based on boundaries, regions and histogram. None of the techniques tested were able to detect only the ACF. However, the canny edge detector and the watershed transform were capable of delimiting the crypts and the algorithm of active contours (snakes) has shown promising results in defining the ACF boundaries, although it has some limitations due to the difficult adjustment of the parameters for different images.

Concluding, some improvements could be made considering the implementations and evaluations performed during this Dissertation, with special attention to the possible advantages if the color information of the endoscopic images is included or if some algorithms are adapted to this application.

Key Words: Colorectal cancer, Aberrant Crypt Foci, Image Processing and Analysis, Image Enhancement, Image Segmentation

x

"No meio de qualquer dificuldade encontra-se a oportunidade"

Albert Einstein

CONTENT

LIST OF FIGURES

LIST OF TABLES

LIST OF ABBREVIATIONS

ACF .... Aberrant Crypt Foci

ACWE... Active Contour without Edges

Ad UM .... Adaptive Unsharp Masking

AMBE.. Absolute Mean Brightness Error

ASIC .... Application Specific Integrated Circuit

CCD.. Charge-Coupled Device

CE .... Capsule Endoscopy

CLAHE .... Contrast Limited Adaptive Contrast Histogram Equalization

CMOS.. Complementary Metal Oxide Semiconductor

CRC .... Colorectal Cancer

CV .... Chan and Vese

DNA .... Deoxyribonucleic acid

FDA.. Food and Drug Administration

HSI .... Hue Saturation Intensity

LED .... Light Emitting Diode

MSE .... Median Square Error

PDE .... Partial Differential Equation

PDF .... Probability Density Function

PSNR.. Peak Signal to Noise Ratio

RGB.. Red Green Blue

SNR .... Signal to Noise Ratio

UM.. Unsharp Masking

Chapter 1

INTRODUCTION

1.1. Motivation

Cancer is one of the most problematic diseases in the modern world. In the United States, one in four deaths is due to cancer (Jemal, Siegel et al. 2008). In Europe, is estimated that 3.2 million people were diagnosed with cancer in 2006 and 1.7 million people died from this disease. Since 2004, the annual number of new cases has increased by 300,000 and due to ageing of the European population, these numbers will probably increase over the next few decades (Gouveia, Coleman et al. 2008). This current situation has promoted the emergence of several research studies with the main goal of early diagnosis and treat, avoiding the cancer. The cancer research could be divided into different areas. One of the two most prominent are: the biological mechanisms, related to the appearance and proliferation of the tumor cells, and the automatic detection of abnormal tissues in images acquired by diagnostic techniques, using methods of computational image analysis. This dissertation is focused on the second domain and studies a particular type of cancer: Colorectal.

In Portugal, this is a growing problem since the latest cancer registries showed that 14.6 % of cancer deaths in 2005 were due to Colorectal Cancer (CRC). Moreover, its incidence ranks second among all cancers in men and women and, from 2000 to 2005, the number of CRC deaths increased at an annual average growth rate of 3% (Pinto, Paquete et al. 2010), Figure 1.1.

The research development on this particular type of cancer achieved some conclusions. As such, it is generally accepted that most CRC arise from preexisting adenomas (Shpitz, Bomstein et al. 1998). In the large intestine, adenomas are polypoid dysplastic foci that are thought to be precursors of cancer. Moreover, in the last few years the early events of human colorectal tumorigenesis have been extensively investigated and since 1987, when Bird first described aberrant crypt foci (ACF) in rodents, it is thought that they may have a crucial role, as they are thought to be a possible precursor of colorectal cancer (Bird 1987). The ACF have been described topologically as clusters of abnormally large colonic crypts identified on the mucosal surface of the human colon after staining with methylene blue (Roncucci, Modica et al. 1998).

Considering this, the identification of ACF in endoscopic images will probably allow the diagnosis and detection of this cancer (Adler, Gostout et al. 2002). Furthermore, since CRC develops over 10–20 years, it provides sufficient time for disease identification and interruption, long before it poses a clinical threat (Hawk, Umar et al. 2004). In this context, the regular analysis through endoscopy or colonoscopy and the detection of ACF on the colon and rectum mucosa will contribute to the early detection of these structures, contributing to the reduction of CRC related deaths.
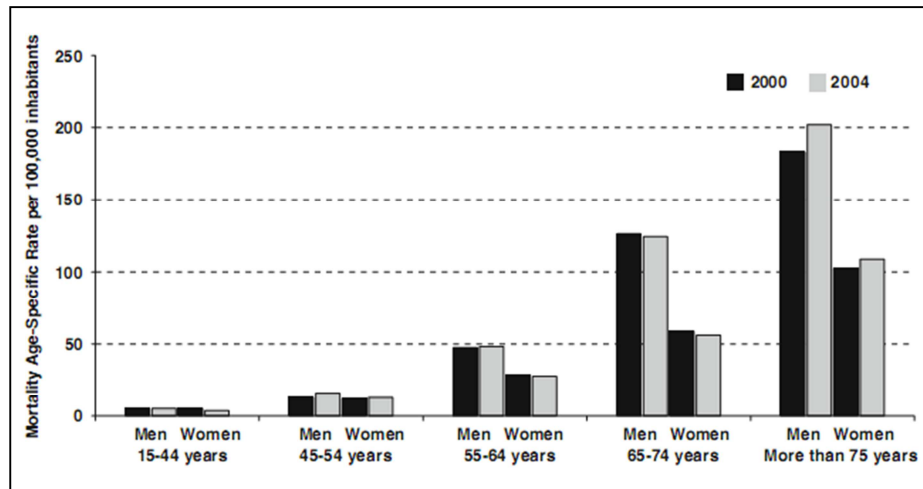
Figure 1.1 – CRC mortality: age-specific rate per 100,000 inhabitants (from (Pinto, Paquete et al. 2010)).

The endoscopic image analysis is generally performed manually by an experienced medical doctor. However, this process is slow and fallible since when using the capsule endoscopy, the amount of information is normally high. To improve the speed and quality of the ACF detection, or to automatically detect the presence of these structures in real time, during the exam, there are several methods of computational analysis that could be used, contributing to the CRC diagnosis.

1.2. Aims

The main purpose of this work was to:

- Study, test and implement image enhancement algorithms to eliminate noise and improve the quality of the endoscopic images acquire *in vivo*;
- Study and test image segmentation algorithms that will allow the identification of ACF structures in an endoscopic image;

- Compare the different algorithms applied and identify the best option to identify ACF in endoscopic images.

1.3. Dissertation overview

This dissertation was divided into five chapters.

In the next chapter, chapter 2, the anatomy, physiology and histology of the colon and rectum is detailed in order to understand the main characteristics of these organs. Moreover, it is described the two principal techniques used to acquire colon images, used in colorectal cancer diagnosis.

Chapter 3 presents a review of literature of the most important algorithms used on medical image processing, with emphasis on enhancement and segmentation methods.

In chapter 4 image enhancement and segmentation methods are implemented and used in endoscopic images and the results are evaluated and compared.

Finally, chapter 5 presents the main conclusions about the experimental results obtained and the comparison done among the different algorithms used. It is then highlighted some of the main advantages and disadvantages of the algorithms cited and indicated some of the possible directions for future research.

Chapter 2

COLON AND RECTUM BIOLOGY AND ENDOSCOPY TECHNIQUE

2.1. Introduction

The biological mechanisms of the colon and rectum are strictly related with its anatomy, physiology and histology. These three topics are essential to characterize the functionality of the colon and rectum in the human organism, in order to understand the normal pathways and the trigger mechanisms involved in Colorectal Cancer (CRC) and Aberrant Crypt Foci (ACF) formation. Furthermore, the diagnosis of CRC is based on images captured by endoscopic technique. Such techniques permit detailed and reliable analysis and represent the best nonsurgical tool available today to manage some diseases of the digestive tube. Nevertheless, they are considerably invasive and frequently ill tolerated by patients (Carpi, Galbiati et al. 2007). Consequently, several advances were pursued leading to the appearance of the capsule endoscopy (CE).

In this chapter is presented the biological basis of the colon and rectum, and the two principal techniques used to acquire colon images to identify ACF structures: colonoscopy and capsule endoscopy.

2.2. Anatomy and Physiology of the Colon and Rectum

The large bowel, located in the abdominal cavity, can be seen as a pipe with a 6 cm diameter and approximately 1.20 cm length. It is subdivided into: the caecum and appendix, the ascending colon, hepatic flexure, transverse colon, splenic flexure, descending and sigmoid colon and the rectum and anal canal, Figure 2.1. Although the large bowel has a bigger diameter than the small one, the epithelial surface area is much smaller, since the colon is about half the length of the small intestine, lacks villi in its mucosa and has a sacculated shape (Widmaier, Raff et al. 2004; Ellis 2011).

The colon represents the terminal segment of the digestive tract and is approximately 1.50 m in length (Moreira Jr and Wexner 2005). However, the human colon should not be considered as one functional unit since the proximal and distal colon differs in many properties.

First part of the duodenum
Right lobe of the liver
Hepatic flexure
Transverse colon
Third part of the duodenum
Right kidney
Ascending colon
Anterior taenia (libera)
Caecum
Vermiform appendix

Spleen
Tail of pancreas
Splenic flexure
Anterosuperior taenia
Left kidney
Descending colon
Anterior taenia (libera)
Left iliac crest
Sigmoid colon
Rectum
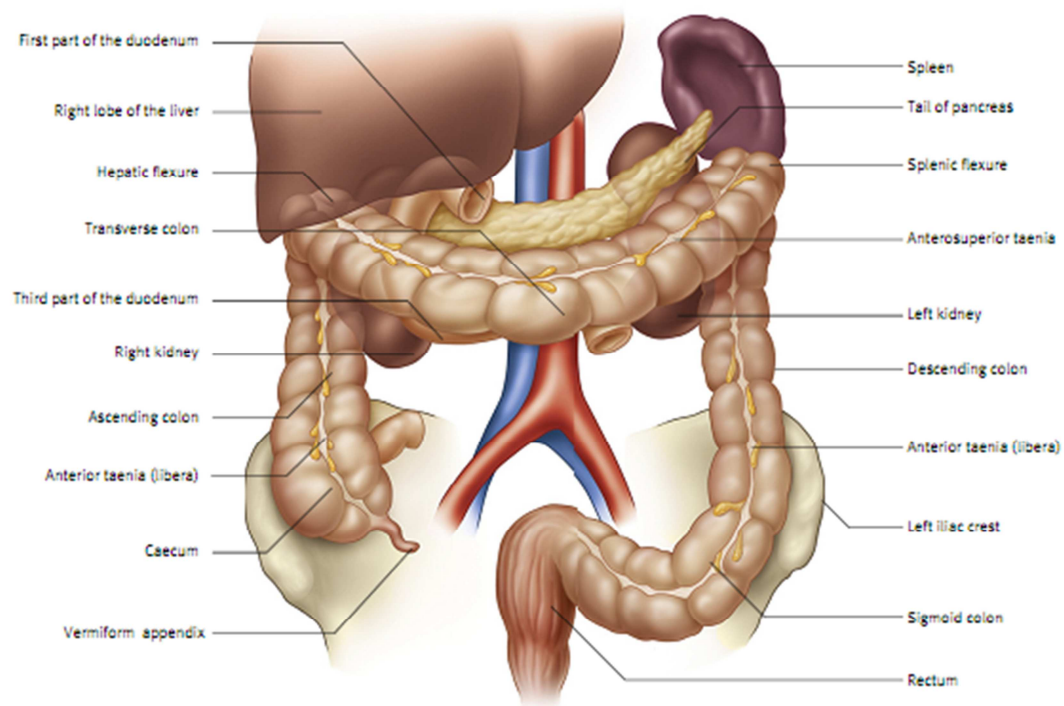
Figure 2.1 – The large bowel (from (Ellis 2011)).

There are differences in the anatomy, neural and blood supply, and absorption characteristics as the length of the colon is traversed. The motility patterns, residence time and properties of luminal contents also differ (Edwards 1997). From the caecum to the sigmoid portion, the size decreases gradually, starting with 7 cm in diameter and finishing with 2.5 cm. The colon has been identified as an organ of importance for the nutrition and health of man having a large metabolic activity, through its intestinal micro flora, and it has a significant ability to absorb water and electrolytes from fecal material (Edwards 1997). It can absorb up to 5 liters of water in 24 hours. The motility of the colon is more complex than observed in either the stomach or the small bowel, and is divided into two functional units: rhythmic peristalsis and tonic contractions (Moreira Jr and Wexner 2005). Moreover, it houses a variety of bacteria, known as commensals, which ferment carbohydrates and release hydrogen, carbon dioxide and methane gas. They also synthesize vitamin K and some B vitamins and are responsible for breaking down the bilirubin into urobilinogen (Porrett and McGrath 2005).

Although the human colon has a lower absorption capacity than that of the small intestine, the material remains in the colon for much longer. Colonic residence time is 2-3 days, whereas food is in the small intestine for as little as 5 hours. This long colonic residence time provides a significant opportunity for the slow absorption of drugs and other materials, either targeted specifically at the large intestinal mucosa or designed to act systemically (Edwards 1997).

The Colon vascularization is dependent on the superior and inferior mesenteric arteries (Mazzucchelli and Maurer 2004).

The rectum, situated at the end of the sigmoid colon, is approximately 13 cm in length and begins where the colon loses its mesentery. It is divided into an upper third, middle third and lower third, lies in the posterior aspect of the pelvis and ends 2-3 cm anteroinferiorly to the tip of the coccyx, where it bends downwards to form the anal canal (Moreira Jr and Wexner 2005; Porrett and McGrath 2005). The rectum exhibits a different mode of motor activity as rhythmic peristalsis is absent most of the time. The mechanism of evacuation is complex and involves voluntary and involuntary muscle activity, mediated by mucosal and pelvic receptors. The interior iliac arteries supply the rectum and anus, and the venous drainage is manly by internal iliac veins. The nerves supplying the large bowel are via the sympathetic and parasympathetic nerves (Porrett and McGrath 2005).

2.3.   Histology of the Colon and Rectum

The large bowel consists of a mucosal membrane with no folds except in its distal (rectal) portion. No villi are present in this portion of the intestine. The intestinal glands are long and characterized by a great abundance of goblet and absorptive cells and a small number of enteroendocrine cells. The absorptive cells are columnar and have short, irregular microvilli (Junqueira and Carneiro 2004).

Analyzing the colon in particular, it consists of a series of concentric layers. Starting in the lumen, these layers are: columnar mucosa, basement membrane, lamina propria, muscularis mucosae, submucosa, muscularis propria, inner circular layer, outer incomplete longitudinal layer (*taenia coli*) and serosa (Ellis 2011), Figure 2.2.

The outer layer of the large bowel, the serosa, is over the colon and is covered by adventitia. The muscularis propria in the colon has the longitudinal muscle layer arranged into three longitudinal bands, the teniae coli. The mucosal surface of the colon at birth is similar to that of the small intestine but rapidly changes with the loss of the villi leaving a flat mucosa with deep crypts. There are stem cells aligned along the crypt wall, and they are believed to

reside in the bottom of the crypt, while transit cells are disposed along the middle part of the crypt axis and the differentiated cells are at the top. As such, the stem cells present at the base of crypts divide and the progeny migrates upward, enter cell cycle arrest, and differentiate before finally reaching the luminal surface epithelial layer, where they undergo apoptosis and shed into the lumen (MacFarlane and Stover 2008), Figure 2.3.
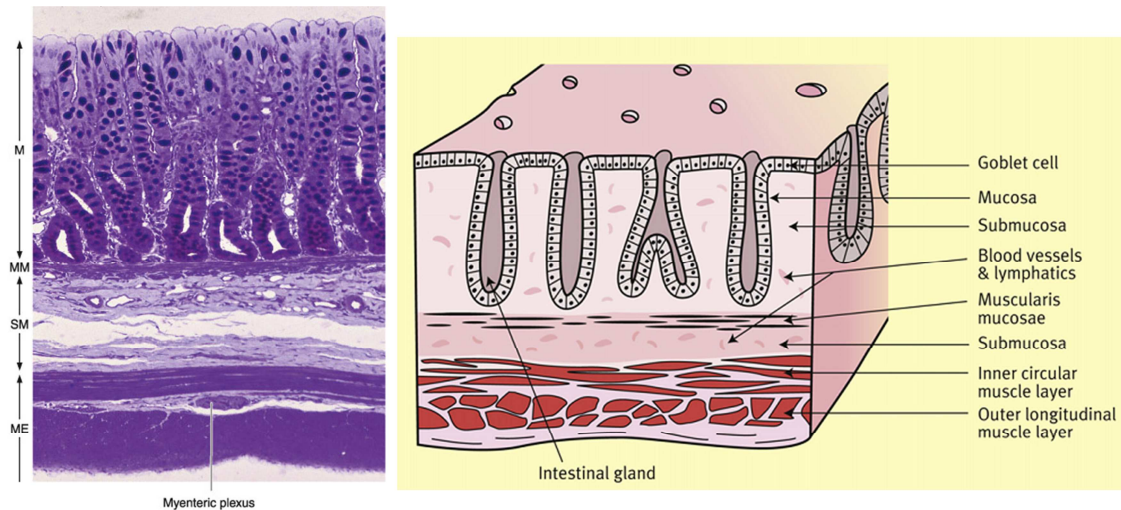
Figure 2.2 – Photomicrograph of a section of large intestine with various structures (left) and a diagram of the histological features of the colon (right). (M - Mucosa, MM - muscularis mucosae, SM -submucosa, ME - muscularis externa (from (Junqueira and Carneiro 2004; Amerongen 2010).
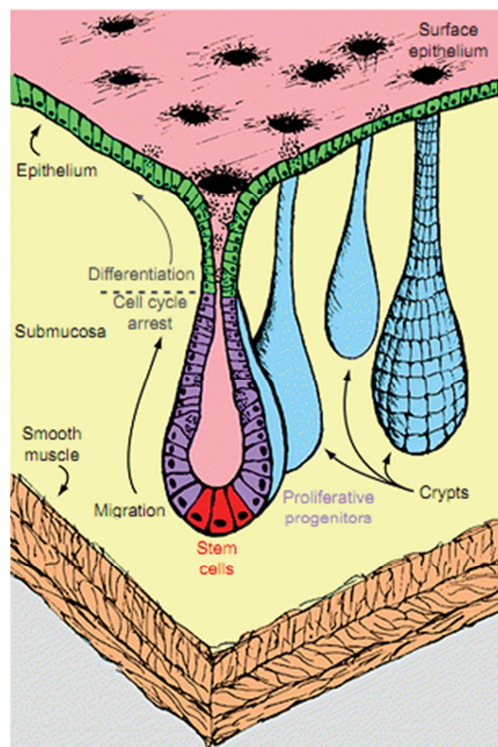
Figure 2.3 – Anatomy of colon and stem cells cycle (from (MacFarlane and Stover 2008)).

There is a decrease in the number of non-goblet crypt cells as the gut ages, which is related to an increase in faecal water. Moreover, in normal colonic crypts, the cells renew completely each three to four days, through a programmed mechanism. If this programmed mechanism changes, a disease may appear: the shapes of the crypts change, they become aberrant crypts, aggregate in clusters, and thus aberrant crypt foci (ACF) appear (Figueiredo, Figueiredo et al. 2010). This event could lead to the appearance of Colorectal Cancer, which is explained in section 2.4.

Finally, the mucosa has a simple columnar epithelium composed of the same cell types as are found in the small intestine, except that Paneth cells are present only in the proximal part of the large intestine, goblet cells are more numerous and absorptive cells are correspondingly fewer. The colonic crypts in the distal colon are longer than those in the proximal colon. At the rectoanal junction, there is an abrupt transition from simple columnar to stratified squamous epithelium. Lymphoid follicles are common, especially in the distal colon and the rectum (Edwards 1997; Amerongen 2010).

2.4. Colorectal Cancer

The complex process of cancer formation is characterized by alterations in the morphology and behavior of normal cells. In a balanced organism, all cells have molecular mechanisms regulating their growth, differentiation and death. However, cells can accumulate a succession of genetic mutations leading to corrupted Deoxyribonucleic Acid (DNA) information (Grady 2004; Doucas and Berry 2006). This information leads to abnormal patterns of gene expression and, as a result, the effects of normal genes that control cell growth, survival and spread are enhanced and those of genes that suppress these effects are repressed. Even after a cancer has been formed, the genetic instability of the malignant cell means that changes in the nature of the cancer continue to occur, creating difficulties regarding treatment strategies. Most cancers result from a series of genetic errors occurring over a prolonged period; hence, the incidence of most cancers increases with age. Aberrant gene expression leads to a number of key changes in fundamental biological processes within cancer cells (Doucas and Berry 2006; Harrington 2008).

Cancer is fundamentally a molecular and a genetic disease, characterized by two classes of genes, oncogenes and tumor suppressor genes, which provide an essential function in normal cells. Oncogenes are the mutation result of the proto-oncogenes, which control cell proliferation, survival and spread. In this way, after the occurrence of mutation, the cancer cell

is capable of uncontrolled cell division, enhanced survival and dissemination. Tumor suppressor genes code for inhibitory proteins that normally act to prevent cell growth. When gene mutation occurs, this function is lost, allowing cancer cells to grow uncontrollably and contributes to tumor formation (Doucas and Berry 2006; Harrington 2008).

The cancer formation is not a simple process, since it involves an initial mutation that must be coupled to cell proliferation and must promote the clonal expansion of the cells. From studies of colon cancer, it appears that at least five mutations in stem cells are needed to trigger the cancer formation (Grady 2004).

The colorectal cancer, so called since it occurs at the colon and rectum, is characterized by these general mutations and processes, but it has several particularities that are going to be detailed henceforward.

Ninety-eight percent of all malignancies that develop within the large intestine arise from glandular mucosa and are thus classified as adenocarcinomas by histology (Limburg and Ahlquist 2004). Malignant transformation of the colorectal epithelium typically occurs as a multistep, multipath, multifocal process that requires sequential or concomitant damage to several genes within and across cellular generations (Hawk, Umar et al. 2004).

The carcinogenesis multistep process begins with the clonal expansion of genetically altered epithelial cells, followed by the formation of clusters of these abnormal cells. The resulting cluster formation is generally denominated Aberrant Crypt Foci (ACF) and represents the earliest stage of dysplasia that can be recognized using current technology. In response to poorly understood molecular signals, a subset of ACF advances to become adenomatous polyps, which are often referred to simply as adenomas (Limburg and Ahlquist 2004), Figure 2.4.

Therefore, ACF are thought to have a crucial role in the multistep process, the adenoma-to-carcinoma sequence, and is explored in section 2.5.

The colorectal cancer screening can reduce substantially the number of deaths, and it is suggested to be performed every 10 years, after completing 50 years old. Colonoscopy remains the gold standard for colorectal exploration. It has the advantage of allowing assessment of the entire colon with the possibility of simultaneous biopsy and removal of any polyps (polypectomy) (Mitry 2008).

Concluding, the progressive findings about CRC and its screening can provide new ways of control cancer dissemination, since at early stages, there are no symptoms or they are non-specific. An effort at detection through screening programs is essential and, in the future, it will certainly contribute to the reduction of the death number (Labianca, Beretta et al. 2004).
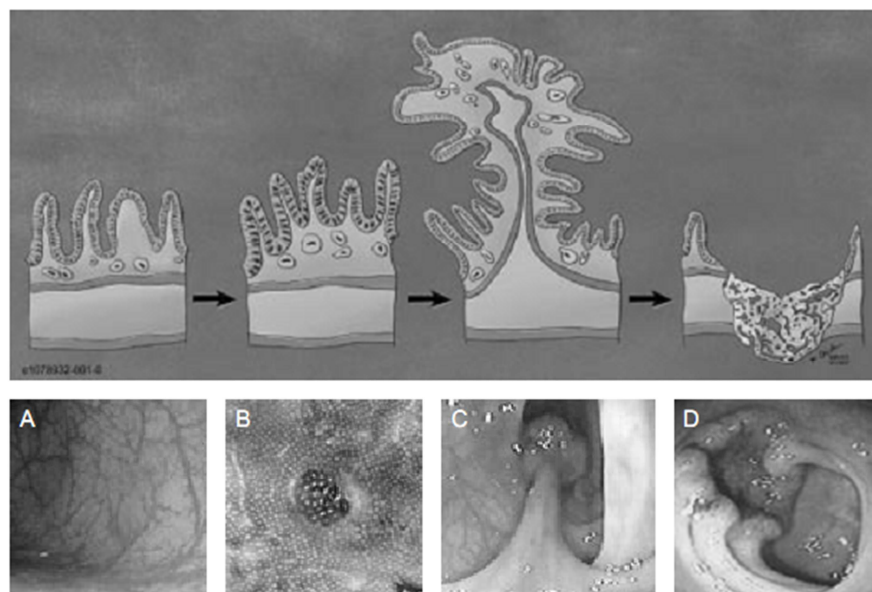
Figure 2.4 – The process of colorectal carcinogenesis, as represented by schematic (upper image) and endoscopic images: A) Normal colorectal mucosa, B) Aberrant Crypt Foci, C) Adenomatous polyp, D) Adenocarcinoma (from (Limburg and Ahlquist 2004)).

2.5. Aberrant Crypt Foci

Aberrant Crypt Foci (ACF) has been studied since 1987, when Bird (1987) first identified these structures in the colon of carcinogen treated rodents. In that study, the mucosal surface of whole rodent colons was examined microscopically after stained with methylene blue. In the next years, several studies have been done using animal models, in an attempt to understand the role of ACF as possible putative preneoplastic lesions, i.e. as an indicator of tumor formation. In these studies, animals were injected repeatedly with a colon specific carcinogen and sequential analysis of histological sections of colonic tissues were performed. The findings have been promising and generally favor the use of ACF as end points in assessing the risk of colon cancer incidence or as biomarkers in the identification of cancer modulators (Pretlow, Barrow et al. 1991; Bird 1995). Considering these facts, the next steps involved studies in human colons.

In 1998, Shpitz el al (1998), Roncucci et al (1998) and Takayama et al (1998) studied several aspects related to the hypotheses that ACF may be an indicator of colon malignancy. The main conclusions achieved by these authors showed that significantly more ACF were observed in patients with carcinoma than in patients with benign colonic disease and that experimental evidence supports the view that density of ACF is strictly related to initiation in colon carcinogenesis. As such, the large number of ACF and those who have dysplastic features may

be precursors of adenoma and cancer. Presently, several studies indicate that the number of ACF increases in patients with colon carcinoma, and that there are more rectal ACF in persons with adenomas (Adler, Gostout et al. 2002; Rudolph, Dominitz et al. 2005).

However, It is also known that a number of compounds with the ability to reduce the occurrence of ACF, e.g. 2-(carboxyphenyl)retinamide or genistein, may actually enhance the development of colon cancers (Mori, Yamada et al. 2004). Moreover, Rudolph et al. (2005) suggests that neither ACF size nor number has been shown to be predictive of progression. Therefore, neither of these ACF characteristics can be considered valid intermediate end points for cancer prevention studies at this time. As such, a better description of the distribution of ACF in the general population, and the relation of ACF to demographic, dietary, and personal habits will be necessary to advance our understanding of the biological meaning of these lesions (Stevens, Swede et al. 2007).

Regarding the influence of age, different studies suggested that the number of ACF in a colon varies with time. Shpitz et al. (1998) observed that the overall prevalence of ACF increased slightly with age, although these differences were not statistically significant. Roncucci et al. (1998) and Takayama et al. (1998) did not observe significant differences that could confirm a relation between the number of ACF and age in patients with colon carcinogenesis. Nevertheless, Takayama et al. (1998) observed an increased prevalence of ACF after 40 years old, and suggested that after this age, periodic endoscopic surveillance of patients is recommended.

Another relevant aspect verified was the existence of gradient of ACF number along the colon. According to Shpitz et al. (1998) and Roncucci et al. (1998), the number of ACF per square centimeter of mucosal surface increased gradually from proximal colon to distal. This fact is consistent with the usual incidence of colorectal cancer, normally situated at the distal colon and rectum.

According to heredity, Stevens et al. (2007) observed a higher mean number of ACF in patients with a family history of CRC than in those without this risk factor. Furthermore, ACF does not appear to be dependent on patient gender, as Roncucci et al. (1998) suggested.

The detection of ACF in the colon mucosa is usually performed by magnifying colonoscopies, an instrument exceptionally well suited for determining the presence or absence of ACF in humans, according to Adler et al. (2002), Figure 2.5. To perform this detection, it is essential to establish a definition of ACF. In this way, according to Mori et al. (2004), ACF are defined as single or multiple crypts that: have altered luminal openings; exhibit thickened epithelia; and are larger than adjacent normal crypts (Fulmanski, Laurain et al.). Additionally, Figueiredo et al. (2009) suggested that ACF were lesions in which the crypts were

more darkly stained with methylene-blue than normal crypts, and that they are often elevated from the focal plane of the microscope, Figure 2.5 and Figure 2.6.
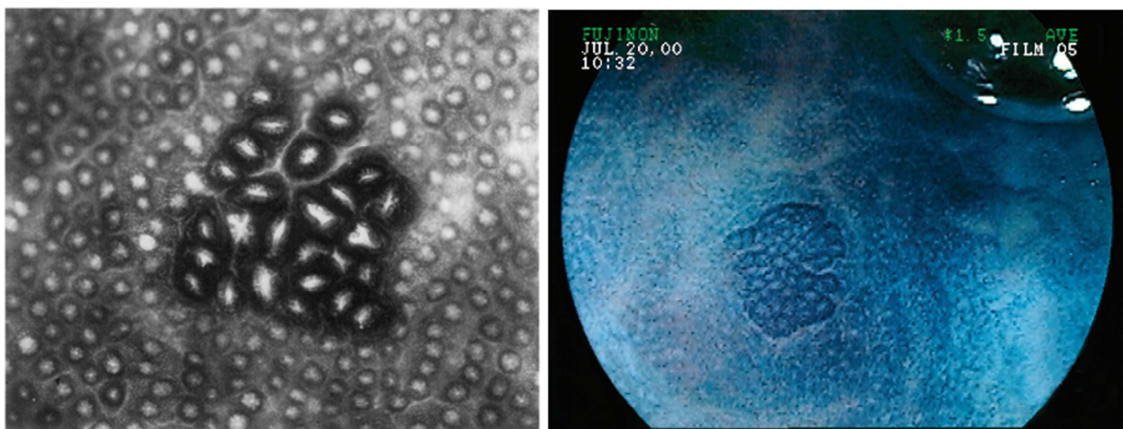
Figure 2.5 – En face photomicrograph of sporadic aberrant crypt focus in sheet of colonic mucosa stained with methylene blue (left) (from (Nucci, Robinson et al. 1997)) and typical endoscopic appearance of an ACF (from (Rudolph, Dominitz et al. 2005); This image was acquired with a Fujinon EC-410 CM magnifying colonoscope after the rectal mucosa had been stained with 0.2% methylene blue.
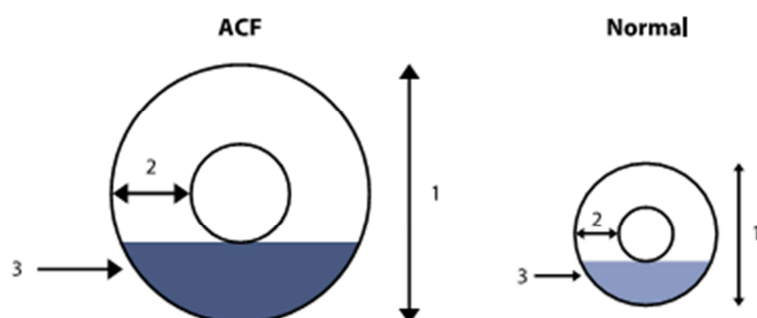
Figure 2.6 – Graphic detection of ACF: 1 – Crypt diameter; 2 – epithelial thickness; 3 – epithelial staining intensity (from (Schoen, Mutch et al. 2008)).

Finally, different studies were performed using only rectal mucosa, since it is easier to use in experimental studies with magnification chromoendoscopy. Figueiredo et al. (2009) used this technique to investigate the possibility of ACF being a carcinogenesis precursor, and found that rectal ACF could be an indicator of a carcinoma elsewhere in the colon.

In conclusion, ACF behavior is still uncertain, but several steps have been made in order to understand its role on the sequence adenoma-carcinoma. Moreover, Akshay et al. (2009) concluded that there are considerable variability among endoscopists about whether or not a lesion is ACF, and about the presence of endoscopic criteria in the lesion under observation.

However, digitally enhanced images, as used by some investigators, may be a solution, but whether they can be implemented for use in large-scale studies is unclear.

2.6. Magnification Chromoscopic Endoscopy

The diagnosis of diseases related to the gastrointestinal tract is based on a particular technique: Endoscopy. In what concerns to ACF, Adler et al. (2002), Takayama et al. (1998) and Figueiredo et al. (2010) suggested that they can be detected *in vivo* with magnification chromoscopic endoscopy. The resultant acquired images will be the basis of the computational analysis performed in this Dissertation project.

The endoscopy technique is used to examine the interior of the gastrointestinal tract and is based on the insertion of an endoscope with special characteristics. According to the American Society for Gastrointestinal Endoscopy (Bosco, Barkun et al. 2003), the flexible endoscopes are composed of three sections: the control section, the insertion tube and the connector section. The control section is outside the patient and directs the insertion tube. The upper front portion of the control section is composed of air/water and suction valves. There are remote switches to modify or acquire the image sequences (Bosco, Barkun et al. 2003).

The insertion tube is attached to the control section and is the portion of the endoscope that is inserted into the patient. It consists of one (or two) instrument channel(s), one (or two) light guide bundle(s), an air channel, a water channel, either an image guide bundle or a charge-coupled device (CCD) chip with wire connections, and angulation wires.

The endoscope tip contains an opening(s) to the accessories/suction channel, an air/water nozzle positioned to clear the lens of debris and permit air insufflation, a light guide illumination system, and an objective lens system (Fulmanski, Laurain et al.), Figure 2.7.

Finally, the connector section of the endoscope has a light guide, an air pipe, and electrical contacts compatible with the processor/light source. This section also has side connectors for a water container, suction, CO_2, insertion tube venting, and a safety-cord connecting mount, which grounds the endoscope, reducing the electrical shock hazard to the operator.

Concluding, the endoscope is a complex equipment which allows the visualization of the gastrointestinal tract, acquiring the images necessary for diagnosis. The signals captured by the endoscope are converted to a color image by one or two systems: (1) Color CCD has a multicolor mosaic filter affixed to the surface of the CCD with illumination by a steady white light (Fulmanski, Laurain et al.), (2) RGB sequential imaging has a rotating multicolor wheel

filter (red-green-blue) located between the light source and the light guide, yielding a visual strobe effect (Bosco, Barkun et al. 2003).
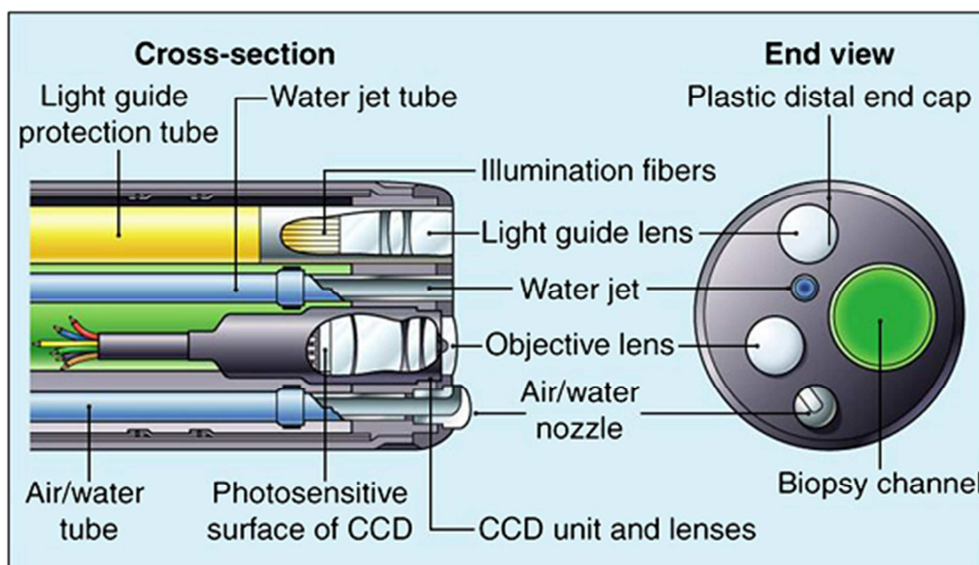
Figure 2.7 – The interior of a videoendoscope (from (Baillie 2007)).

In what concerns to Chromoendoscopy, it is a technique in which tissue stains are applied to the gastrointestinal mucosa at endoscopy to better characterize, delineate, or high-light specific gastrointestinal findings. At times, it may be used with an endoscope that also magnifies the image (magnification endoscopy). Stains of the current generation often are classified according to their interaction with gastrointestinal mucosa (Schwartz and Lichtenstein 2004). The ACF lesions are stained using methylene blue, a vital stain that is taken up by absorbent tissue such as the small intestinal and colonic epithelium. A total of 10-20 ml of methylene blue is sprayed with a spraying catheter directly over the mucosa, and after 1-2 min the mucosa is washed with water to allow examination of the staining effects (Kida, Kobayashi et al. 2003).

The magnification includes two different concepts: high resolution and amplification. As such, a magnification endoscopy is described by the ability to discriminate small objects with 10-17 µm and the amplification of the lens can achieve 105 times. The dimension of a normal human crypt is approximately 74 and 433 µm, for horizontal and vertical cross sections. In this way, the magnification chromoscopic endoscopy is a valuable tool in the diagnosis of ACF lesions.

2.7. Capsule Endoscopy

In spite of the significant advances in digestive tube diagnostic, there are still some problems to solve. One of the major concerns was related to the inaccessibility of exploring the small bowel, since there are only 2 types of endoscopes using probes which are introduced into the oral or rectal cavities by means of insertion tubes. Such techniques allow detailed and reliable analyses and represent the best nonsurgical tool available today to manage some diseases of the digestive tube. Nevertheless, both gastroscopy and colonoscopy are considerably invasive and frequently ill tolerated by patients. Moreover, they have to be performed by skilled personnel (Carpi, Galbiati et al. 2007). Consequently, several advances were pursued leading to the appearance of the capsule endoscopy (CE), Figure 2.8.

Since 2000, when Iddan et al. (2000) first reported the CE, it has developed rapidly with important technical improvements. Initially, CE was created to explore the small bowel, but currently there are other solutions where it is applied to esophagus and the colon (Michel and Gérard 2008). The system consists of the following components: a capsule endoscope, a sensing system composed of sensing pads attached to the trunk, a data recorder, a battery pack, and a personal computer workstation with proprietary software that reviews and interprets the images (Mishkin, Chuttani et al. 2006). With ethical committee approval, the first human volunteer study was performed in August 1999. The wireless capsule endoscope has received a CE mark and FDA approval in August 2001 for use in patients (Swain 2003). The main specifications of the capsule endoscope can be found in (Mishkin, Chuttani et al. 2006).

The intestinal endoscopic capsule was designed to be swallowed and to go through the digestive tube, capturing approximately 50000 frames during 8 hours of examination. After that time, it is normally expelled by the organism and the resulting data are downloaded, processed and finally viewed on a monitor (Michel and Gérard 2008). Considering the large amount of information captured by a capsule endoscopy and the posterior time of analysis by a physician (usually, between 40 and 60 min, depending on the experience), several solutions have been created to reduce this time, and to process automatically the resultant images in an attempt to identify some pathologies, like small bowel inflammation, ulcers, and cancer cells (Dias, Correia et al. 2007; Natalin and Landman 2009; Iakovidis, Tsevas et al. 2010). Another innovative investigation with CE is trying to control its navigation, since the impossibility of any motion control of the capsule makes the visceral exploration not accurate enough (Carpi, Galbiati et al. 2007).

Despite the advantages of the endoscopic capsule, it can cause some problems such as obstruction, particularly in presence of some diseases as Crohn's, or influence on electrical devices as pacemakers (Adler and Goustout 2003).

In this Dissertation, it will be performed endoscopic image analysis acquired by endoscopy in an attempt to automatically detect aberrant crypt foci, since they are thought to be colorectal cancer precursors. However, in the future this analysis would be extent to capsule endoscopy and will contribute to help physicians in their process of diagnosis.
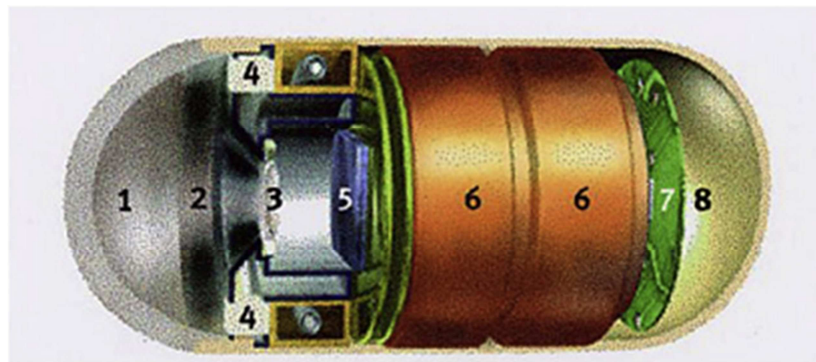
Figure 2.8 – Internal view of an endoscopic intestinal capsule showing the different technical elements: 1 – Optical Dome; 2 – Lens Holder; 3 – Optical Lens; 4 – Light Emitting Diodes (LEDs); 5 – CMOS Imager; 6 – Batteries; 7 – ASIC Transmitter; 8 – Antenna (from (Michel and Gérard 2008).

Summary

The colon and rectum represent the terminal portion of the gastrointestinal tract. Their main function is to absorb water from the remaining food digested. The mucosa is characterized by the absence of villi and the presence of deep crypts. When the cell differentiation mechanisms change, those crypts became aberrant, and ACF appear. These lesions could be precursors of Colorectal Cancer and, as such, its detection may prevent the evolution of this disease.

The principal techniques used to diagnose diseases associated with the gastrointestinal tract are endoscopy or capsule endoscopy. The second has the advantage of being no invasive and more tolerated by patients. The images acquired by endoscopy will be used to detect ACF using algorithms of image processing.

Chapter 3

METHODS OF COMPUTATIONAL ANALYSIS

3.1. Introduction

The detection of pathologies through endoscopic images has been performed by medical doctors, usually trained for that. However, in spite of being good in their tasks, they are also affected by fatigue, boredom, environmental factors, are susceptible to committing errors, and they are regularly subjective and qualitative (Rangayyan 2005). Hence, there are several computational techniques of image processing and analysis capable of detecting patterns, edges, clusters, etc., that can aid medical doctors in their diagnosis.

Concerning to endoscopic images, acquired by capsule endoscopy, there are approximately 50000-60000 images per examination, and it takes experienced medical clinician over an hour to view and analyze all the video data. Moreover, the physicians might miss some abnormalities if they were present only in one or two frames of the image sequence, or if that cannot be detected by the naked eyes due to their size, color, texture and distribution. Furthermore, distinct clinicians may have different findings when come to the same image data. All these problems motivate the researchers to develop reliable and uniform assisting approaches to reduce the great burden of the physicians (Baopu and Meng 2007).

Techniques of biomedical image processing and analysis can be powerful tools that can aid the answering to these issues discussed above. Considering this, an overview of the principal techniques used in biomedical image processing is detailed in this section and, later, a review about what is specifically applied to endoscopic images is presented.

3.2. Digital Image

To understand the basis of techniques of image processing is important to define first the properties of a digital image. At the most basic level, a digital image is represented by a rectangular array of numbers, divided into small regions: pixels. The intensity number inserted in each pixel reflects the brightness of the image at the corresponding point (Castleman 1996).

In Figure 3.1, the amplification of an image reveals the matrix composed by pixels with the intensity values. Since this image is in the gray scale, each array of the matrix corresponds to a gray level from 0 (zero) to 1 (one), where 0 is white and 1 is black.
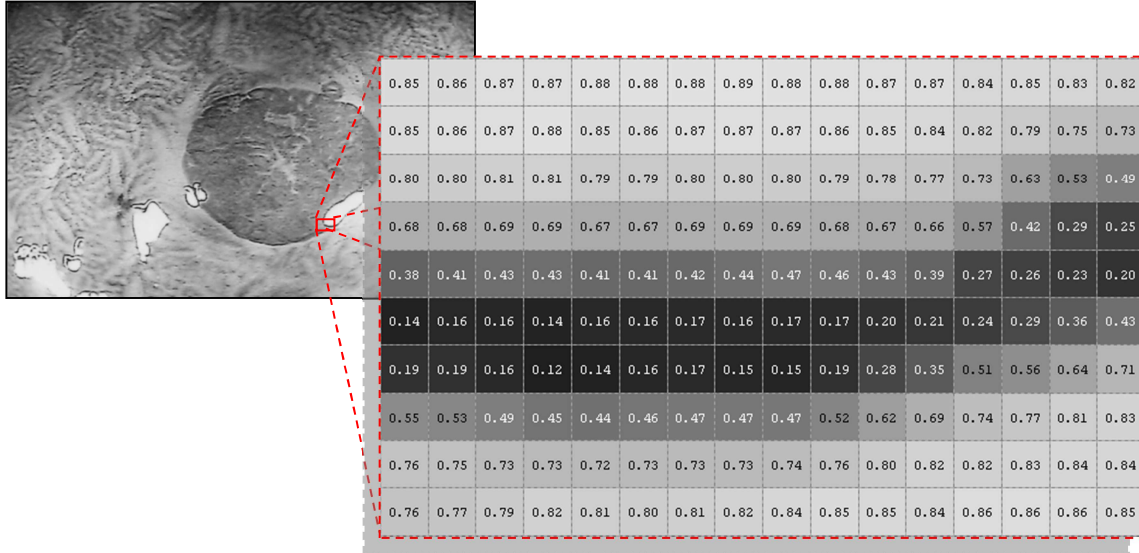
Figure 3.1 – Digital image matrix.

However, there are several formats in which an image can be represented. The two principal formats of color images referred in the literature are RGB (Red, Green and Blue) and HSI (Hue, Saturation and Intensity). In the RGB model, each color appears in its primary spectral components of red, green and blue. As such, an image is represented by 3 matrixes, each one representing the intensity level in the red, green and blue domain.

The HSI model is composed of three main characteristics: Intensity, Saturation and Hue. Intensity is the average of the R, G and B grey levels, although different schemes with unequal weighting of the colors are also used. The intensity does not have any information about color and, as such, Hue and saturation are responsible for that information. Hue is expressed as an angle and it refers to the spectral wavelength that most closely matches with the original image. The saturation parameter is described as the radius of the point from the origin of a color circle. Around the periphery of the circle, fall the saturated color and at the center lie neutral (gray) shade (zero saturation) (Castleman 1996).

Any solution of digital image processing and analysis can be divided in fundamental steps. According to Gonzalez and Wood (2002), such steps are image enhancement, image restoration, compression, morphological processing, segmentation, representation and description, and recognition. However, the aims of this Dissertation are based on just some of the steps enumerated. Hence, only the relevant methods of these steps will be detailed.

3.3. Image Enhancement

Image pre-processing is usually performed in order to reduce or eliminate noise and to reduce system invariance to acquisition settings. Yu and Jan (2009) suggested that the pre-processing stage consists of several subtasks, including image enhancement, noise reduction, gradient magnitude estimation and preliminary LOI (layer of interest) extraction. Moreover, pre-processing could be used to normalize size and intensity value scale, in order to obtain process and analyze the images with less variability.

One of the main topics in this issue is image enhancement, which purpose is to process an acquired image for better contrast and visibility of features of interest for visual examination (Sternberg 1983). Moreover, the principal objective of image enhancement is to modify attributes of an image to make it more suitable for a given task and a specific observer (Maini and Aggarwal 2010). However, in some cases the enhancement could lead to loss of relevant information.

To better understand the methods involved in image enhancement, this section will explore the most relevant algorithms used in this medical image processing step.

The aim of image enhancement is to enhance contrast, edges and general detail visibility in the image, without causing any distortion or artifact. There are two different domains, in which this image processing task can be done: Spatial and Frequency. Based on Rangayyan (2005), the fundamental algorithms used in this step of image processing are depicted in Figure 3.2.
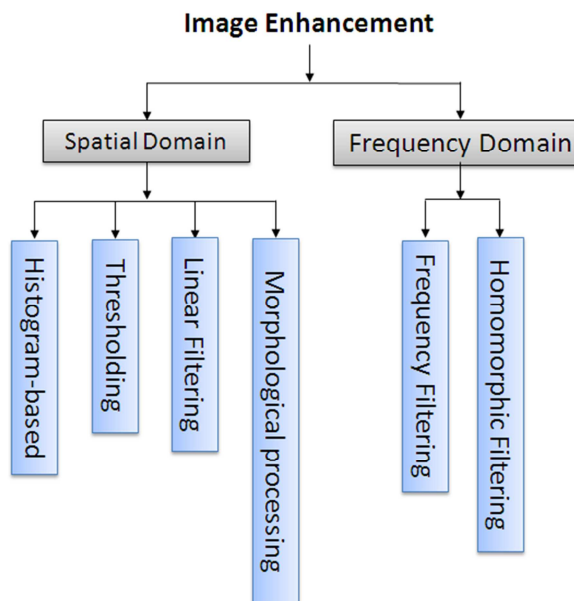
Figure 3.2 – Image Enhancement algorithms.

The spatial domain methods are performed in the image matrix, varying the pixel intensity value directly, while the frequency domain methods imply the Fourier Transform. In order to understand the basic principles involved in these algorithms, they are explained in the next sections.

3.3.1. Spatial Domain

3.3.1.1. Thresholding

Based on image histogram, which indicate the gray level intensity distribution, it is possible to improve the visibility of selected details and alter the overall appearance of the image.

When the gray level of the object of interest in an image is known or can be determined, the image may be thresholded to separate the object from the image background. Otsu (1979) proposed a method to automatically determine the threshold value from the histogram information. This method is simple and may be considered to be a form of image enhancement in the sense that the objects of interest are perceived better in the resulting image. The equation used to describe this method is:

$$g(m,n) = \begin{cases} 0 \; if \; f(m,n) \le L1 \\ f(m,n) \; if \; f(m,n) > L1' \end{cases} \tag{3.1}$$

where $g(m,n)$ is the output image, $f(m,n)$ is the input image and $L1$ is the threshold established or determined automatically.

If the region of interest has a specific range of gray levels (between $f1$ and $f2$), it could be performed a threshold in a window:

$$g = \begin{cases} 0 \; if \; f(m,n) \le f1 \\ \frac{f(m,n) - f1}{f2 - f1} \; if \; f1 < f(m,n) < f2. \\ 0 \; if \; f(m,n) > f2 \end{cases} \tag{3.2}$$

3.3.1.2. Histogram-based

The histogram of an image represents the number of occurrence of each intensity level providing the distribution of intensities in such image. Usually, the histogram is normalized,

dividing each of its components by the total number of pixels in the input image, allowing a better comparison between images.

Histograms are the basis for numerous spatial domain processing techniques and could be used for image enhancement, as shown in this section. In comparison to other methods, the advantages of histogram based techniques are simplicity and less computational demanding. The two principal methods are histogram equalization and histogram stretching. They have a common objective: improve the image contrast, enhancing the separation between the object of interest and the image background (Gonzalez and Woods 2002).

a) *Histogram Equalization*

The histogram equalization is a non-linear transformation that stretches the histogram of the input image such that the gray level occurs in the output image with equal probability, performing a contrast adjustment. The uniform distribution of the output image histogram is limited by the discrete computation of the gray-level transformation (Yeganeh, Ziaei et al. 2008).

This algorithm can be applied to the entire image (global) or be performed locally (adapted). The adapted histogram equalization operates on small data regions (tiles) rather than the entire image. Each tile's contrast is enhanced so that the histogram of the output region approximately matches the specified histogram. The neighboring tiles are then combined using bilinear interpolation in order to eliminate artificially induced boundaries (Pizer, Johnston et al. 1990).

In cases of images with varying background, the adapted algorithm is the best choice, since it is not affected by this variation.

b) *Histogram Stretching*

The histogram stretching consists in distributing the pixel appearance frequencies over the entire width of the histogram. Thus, the gray values of the input image are scaled to the range defined, expanding the histogram and enhancing the contrast. This is an attempt to improve an image making full use of the possible intensity values.

The first step is to determine the lower (a) and upper (b) limits over which image intensity values will be extended. Posteriorly, the minimum (c) and maximum (d) values of the image

are calculated and if these were equal to the limits determined, then there will be no stretching. Otherwise, for each pixel, the original value r is mapped to output value s using:

$$s = (r - c)\left(\frac{b-a}{d-c}\right) + a. \tag{3.3}$$

However, if the original image has outliers, i.e., pixels with an intensity value very high or low when compared to the whole image, the stretching will be done based on those values, resulting in lower contrast (Gonzalez and Woods 2002).

3.3.1.3. Linear Filtering

The spatial filtering is focused on local operators that allow using the context of the image in which each pixel is inserted. It involves the convolution of the input image with a specific mask to enhance the image (usually of size 3x3), moving the filter mask from point to point in an image, calculating the sum of products of the filter coefficients and the corresponding image pixels in the area spanned by the filter mask, Figure 3.3.
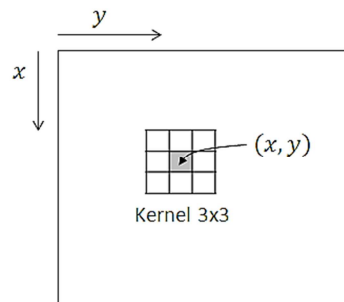
Figure 3.3 – The application of the convolution mask in an image in the spatial domain (adapted from (Gonzalez and Woods 2002))

The convolution mask (Figure 3.3) is the key factor in linear filtering since its coefficients determine the filtering desired, being usually descried in the literature two types of filters that could be applied: Smoothing and Sharpening.

a) Smoothing

The smoothing filters are commonly used to reduce noise with high intensity variation values, since they calculate the average of the pixels contained in the neighborhood of the

filter mask, being sometimes called average filters. The output image is blurred since every high intensity variations are averaged, which lead to an image without well-defined edges. Considering this, this method should be used in situations where the losses of sharp edges compensate the noise reduction.

There are three different methods used in this topic: mean filter, Gaussian filter and median. The first two are very similar, but while the mean filter calculates the arithmetic average of the pixel and its neighbor, the Gaussian filter is based on a normal distribution, with two parameters: average and standard deviation. The median filter is very useful to reduce noise with high-intensity values, as salt & pepper. In each pixel with a neighborhood defined, the algorithm sorts in crescent order the intensity values and attribute the median value to the pixel, allowing the elimination of the higher and smaller values (Gonzalez and Woods 2002).

b)   Sharpening

In opposite to smoothing algorithms, sharpening spatial filters are used to highlight transitions in intensity, making the edges more evident. The most common methods are based on spatial differentiation, in particular first and second order derivatives. The definition of the first order derivatives of the function $f(x)$ in one dimension is expressed as:

$$\frac{\partial f}{\partial x} = f(x + 1) - f(x).$$

(3.4)

Moreover, any definition used for a first derivative must be zero in areas of constant intensity, nonzero at the onset of an intensity step or ramp and must be nonzero along ramps.

The second order derivative is defined as:

$$\frac{\partial^2 f}{\partial x^2} = f(x + 1) + f(x - 1) - 2f(x).$$

(3.5)

Similarly, any definition used for a second derivative must be zero in constant areas, nonzero at the onset and end of an intensity step or ramp, and must be zero along ramps of constant slope.

The most common algorithms used for first and second order derivative are, respectively, Sobel and Laplacian. The implementation of these methods will sharp the edges of the image.

Finally, there is another method to sharpen images that consist of subtracting an Unsharp (smoothed) version of an image from the original image (Rangayyan 2005). This process is called Unsharp Masking and comprises the steps schematized in Figure 3.4.
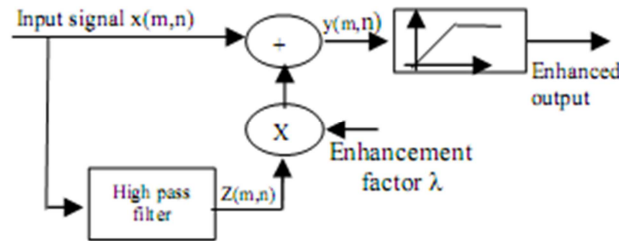
Figure 3.4 – Conventional Unsharp Masking technique (from (Badamchizadeh and Aghagolzadeh 2004)).

3.3.1.4. Morphological processing

The mathematical morphology investigates the geometrical structure of sets and consists of four basic transformations: erosion, dilation, opening and closing. In image processing, these transformations are defined in terms of a structuring element which interacts with the input image in order to extract useful information. A structuring element is an object, other than the image object, of simpler shape than the original image object, and it is chosen according to its geometrical properties.

The erosion of an image has the effect of shrinking the image with respect to the geometry of the structuring element and could be implemented using OR boolean logic. In opposition to this is the dilation, which effect expands the image and could be implemented using the AND boolean logic (Schonfeld 1991).

The operations of opening and closing are related to the erosion and dilation. As such, the opening consists of erosion followed by dilation with the same structuring element, and the closing is the opposite, i.e., a dilation followed by erosion.

3.3.2. Frequency Domain

The frequency domain image processing is based on the Fourier transform and the mathematical operations that could be performed in this domain. Hence, frequency domain is the space defined by values of the Fourier transform ad its frequency variables.

3.3.2.1. Frequency Filtering

Filtering in the frequency domain is simple and straightforward. Generally, the Fourier transform of the image is multiplied by the filter function and then the inverse Fourier of the product will present the resulting image (Bansal, Bajpai et al. 2007). Thus, given an image $f(x, y)$, of size $M \times N$, the basic filtering equation in which we are interested has the form:

$$g(x, y) = \Im^{-1}[H(u, v)F(u, v)], \tag{3.6}$$

where $\Im^{-1}$ is the inverse of Fourier Transform, $F(u, v)$ is the Fourier Transform of the input image, $f(x, y)$, $H(u, v)$ is a filter function and $g(x, y)$ is the filtered (output) image.

The result of this filtration is based on the filter function that could represent a High pass or Low pass filter. The edges and noise in the image are the result of high frequencies, while low frequencies are responsible for the general gray-level appearance over smooth areas. Hence, a low pass filter will attenuate high frequencies and the resulting image will smooth. On the contrary, the high pass filter will enhance the edges (Gonzalez and Woods 2002).

Concluding, the frequency filtering could be compared to the linear filters of smoothing and sharpening, but the implementation is easier.

3.3.2.2. Homomorphic Filtering

The Homomorphic filtering is a technique that defines an image $F(x, y)$ as a product of illumination $I(x)$ and reflectance $R(x, y)$, and can be expressed as:

$$F(x, y) = I(x, y) \times R(x, y). \tag{3.7}$$

The illumination component of an image generally is characterized by slow spatial variations, while the reflectance component tends to vary abruptly, particularly at the junctions of dissimilar objects. However, these two components expressed at the equation 3.7 cannot be used directly since the Fourier transform of the product of two functions is not separable. Hence, if the equation is represented as a logarithmic function, then the product is transformed in a sum operation:

$$\ln(x, y) = \ln\big(I(, xy)\big) + \ln(R(x, y)). \tag{3.8}$$

The implementation of the Homomorphic filtering is summarized in the diagram presented in Figure 3.5.

The filter $H(u,v)$ is chosen respecting the tendency of decreasing the contribution made by the low frequencies (illumination) and amplifying the contribution made by high frequencies (reflectance). The result will show simultaneous dynamic range compression and contrast enhancement (Gonzalez and Woods 2002; Rangayyan 2005).

$$f(x,y) \Rightarrow \boxed{\text{ln}} \Rightarrow \boxed{\begin{array}{c}\text{Fourier} \\ \text{Transform} \\ (\Im)\end{array}} \Rightarrow \boxed{H(u,v)} \Rightarrow \boxed{\Im^{-1}} \Rightarrow \boxed{\text{exp}} \Rightarrow g(x,y)$$
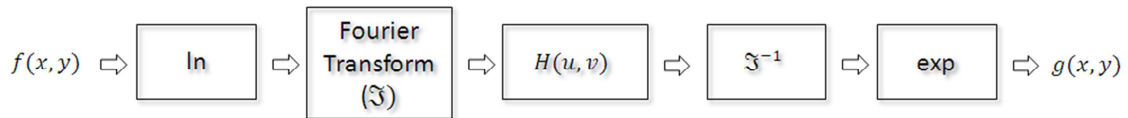
Figure 3.5 – Steps in Homomorphic filtering (from (Gonzalez and Woods 2002)).

3.4. Image Segmentation

One of the most critical steps in the process of reducing images to high-level information is segmentation. It subdivides an image into its constituent regions or objects and the level to which it is applied depends on the desired result, that is, segmentation should stop when the objects of interest in an application have been isolated (Gonzalez and Woods 2002).

Rangayyan (2005) proposed that image segmentation could be divided into four main categories, Figure 3.6. These techniques are detailed in this section.
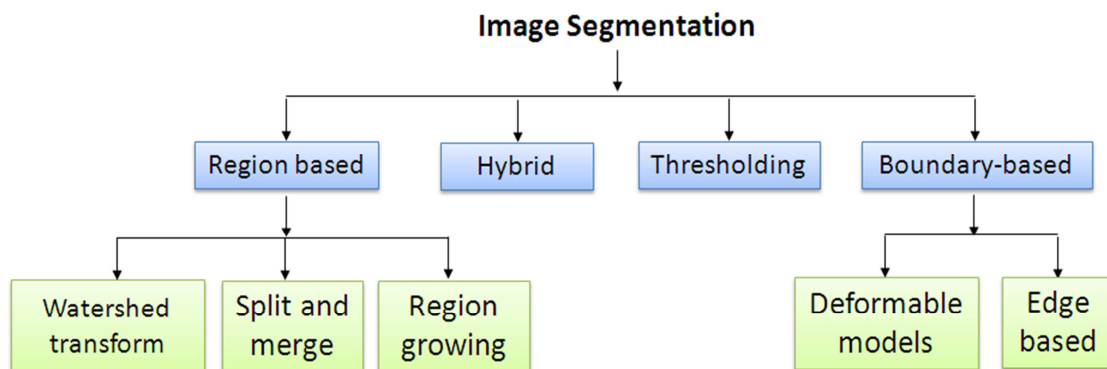
Figure 3.6 – A classification of image segmentation approaches.

3.4.1. Thresholding

The process of image thresholding is used to separate an object from the image background. As such, one simple way is to define a range of brightness values in the original image, select the pixels within this range as belonging to the foreground, and reject all the other pixels to the background, dividing an image into two levels: usually black and white (binary image) (Russ 2002). Mathematically, it could be defined as:

$$g(x,y) = \begin{cases} 1, & f(x,y) < T \\ 0, & f(x,y) \geq T' \end{cases} \tag{3.9}$$

where $g(x,y)$ is the output image, $f(x,y)$ the input image and T the defined threshold value.

Moreover, the definition of the threshold value can be manual, requiring previous knowledge or iterative experiments, or automatically, which combines the image information to get the threshold value to be used. Otsu (1979), as mentioned previously, suggested a method to automatically find the value of the threshold based on the image histogram, and it is generally applied on the entire image. However, the global technique could not be the best option when the image has illumination variability. Thus, it was developed an adaptive threshold that is processed locally.

Wellner (1993) described a new quick adaptive threshold based on the more complex algorithm proposed by R. J. Wall (Castleman 1996). The basic idea is to run through the image while calculating a moving average of the last pixels seen. When the value of a pixel is significantly lower than this average, it is set to black, otherwise it is left white. Only one pass through the image is necessary, and the algorithm is simple enough to be implemented in hardware.

3.4.2. Boundary-based

An image boundary is defined as a discontinuity in pixel intensity and corresponds to the contour that separates the object from the background. Thus, the aim of the algorithms included in this topic is to segment an image based on the edges of each region by locating the pixels whose intensity varies abruptly.

The image gradient is a powerful tool in the edge-based algorithms, since it is capable of detecting the intensity variability over the image. Moreover, in what concerns to deformable models, the active contour (snake) algorithm also uses this information to move the initial contour toward the object of interest.

3.4.2.1. Edge-based

An image edge is generally defined as a boundary between two regions with different grey-level properties. The algorithms of segmentation based on edge detection try to separate the interested regions according to its boundaries. Hence, the edge detection algorithms can be simple as Sobel, Laplacian, Prewitt and Roberts, or more complex as Canny, which are the most preeminent examples of this type of segmentation.

The Laplacian edge detection is based on the calculation of the second derivative of the image that will produce an abrupt zero-crossing at an edge (Davis 1975). It is commonly implemented digitally by a 3x3 convolution kernel that will convolve with every pixel of the image, resulting in an output image with the edges detected.

The Sobel edge detector uses two kernels with horizontal and vertical direction. It calculates the magnitude and direction gradient of each pixel and its neighborhood. Since an edge is characterized by a higher magnitude value when compared to its neighborhood, this detector will be able to detect every edge and construct an output image with a black background and white edges. Alternatively, Roberts and Prewitt edge detector are also based on the image gradient, but uses different mask coefficients to highlight the image edges.

Finally, Canny (1986) proposed a new method based on finding the zero-crossing of the laplacian of Gaussian (LoG), a bandpass filter that calculates the second derivative of a smoothed image (Canny 1986; Russ 2002).

3.4.2.2. Deformable models-based

The algorithms included in this group can be viewed as a modeling of curve evolution. They could be divided into parametric and geometric.

Starting with parametric models, they track the evolution through sample contour points. The moving equation for the contour can be derived through energy functions or defined directly through dynamic forces (Ma, Tavares et al. 2009).

One of the most common deformable models is the snake method. It was developed by Michael et al (1988), who described this method as a matching of a deformable model to an image by means of energy minimization. From any starting point, the snake deforms itself into conformity with the nearest salient contour. Normally, it is used an edge detector based on the image gradient to detect the boundary of the desired object. As such, a snake is an energy-

minimizing spline that pulls it toward features such as edges, and constrained by internal spline forces that impose piecewise smoothness (Rangayyan 2005).

Concerning to geometric deformable models, there are two principal methods described: Level-set and Chan and Vese model.

The Level-set method was fists introduced by Osher and Sethian (1988) and is based on a partial differential equation (PDE), the Hamilton Jacobi equation. The main idea is to implicitly embed the moving contour into a higher dimensional level set function and view the contour as its zero level set. Then, instead of tracking the discrete contour points, one can track the zero level set of the level set function. Formally, the evolution of the interface is driven by a time-dependent PDE where the so-called velocity term reflects the image features characterizing the object to be segmented. The level set methods have been successfully applied to structural shape and topology optimization problems (Gelas, Bernard et al. 2007; Wang, Lim et al. 2007; Ma, Tavares et al. 2009).

The Chan and Vese (2001) model can be described as an active contour without edges. As such, contrary to snakes, this method is not based on an edge function to stop the evolving curve on the desired boundary. It is based on Mumford–Shah (1989) segmentation techniques and the level set method and is capable of detecting objects whose boundaries are not necessarily defined by gradient or when they are very smoothness, for which the classical active contour models are not applicable. The algorithm extracts the desired object through simultaneously minimizing the intensity variations inside and outside the contour. The most appreciable advantage of Chan and Vese model is that it can obtain a boundary of discrete points, which is quite useful when the objects of interest are represented by discrete pixel clusters and have no clearly defined boundaries (Ma, Tavares et al. 2009).

3.4.3. Region-based

Algorithms based on regions are used to separate objects from the background, taking into account the pixels' properties of a region. The three principal methods cited are region growing, split and merge and Watershed transform. The result of these three methods is the identification of the objects of interest, distinguishing them from the image background.

3.4.3.1. Region Growing

Region growing, initially proposed by Adam and Bischof (1994), is a procedure that groups pixels with similar characteristics as gray level, texture or color. The simplest approach starts with a "seed" point, that could be a single pixel, and according to the properties of the seed,

the group is formed through attachment of other pixels with the same characteristics. The process of growing should stop when no more pixels satisfy the criteria for inclusion in that region (Gonzalez and Woods 2002; Jun 2010).

3.4.3.2. Split and Merge

The region splitting and merging is an alternative image segmentation algorithm that aggregate pixels according to their similarity. It was first proposed by Pavilidis (1974) and is widely used directly or indirectly in image processing. This algorithm initiates with the subdivision of the image into a set of arbitrary disjoint regions and then, it starts to merge according to the similarities between them. Hence, it is defined a threshold that establishes the conditions of merging.

3.4.3.3. Watershed

Watershed is a method that often produces more stable segmentation results. It is based on a geographical concept, where the watershed is an area of land that could be flooded with water, maintaining the watershed lines visible at the end. These lines will correspond to the objects' boundaries and will contribute to segment the image into regions (Castleman 1996).

3.5. Application on Endoscopy Images

Different investigation work has been made to detect the presence of colon cancer from two perspectives: in histological colon tissues, or through detection of polyps or, more recently, ACF in endoscopic images. In this Dissertation project, the aim is to detect Aberrant Crypt Foci using endoscopic images.

In the literature, there are several algorithms that have been applied to segment medical images. Regarding the segmentation of endoscopy images, Liedlgruber (2009) proposed several important measures to improve the quality of the acquired images. In Figure 3.7, the usual steps performed to process and analyze endoscopic images are depicted. Due to the fact that images taken using a traditional endoscope often suffer from various kinds of degradations, usually, techniques of pre-processing are applied on the original images. The most common problems found in endoscopy images are related to undesired noise caused by

Charge-Coupled Device (CCD) or Complementary Metal Oxide Semiconductor (CMOS) chips, inhomogeneous brightness and poor contrast and blurred images due to the focus problems and peristaltic movements. Authors have been proposed several solutions to overcome these problems, including linear filtering with appropriate filters or low pass filtering in the frequency domain to reduce noise, histogram equalization to enhance contrast and high pass filtering to reduce blur.
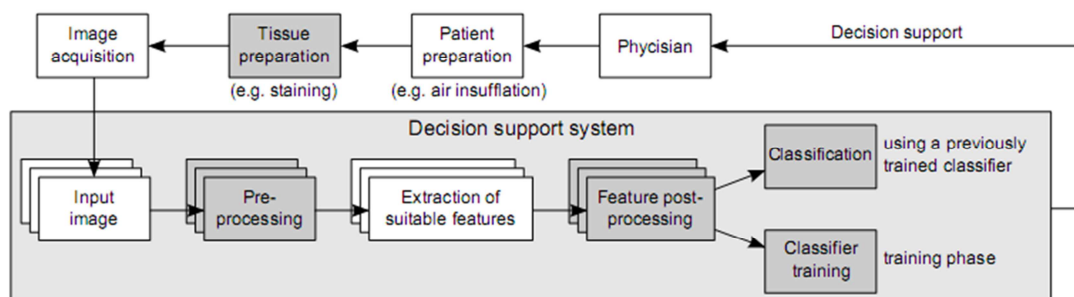
Figure 3.7 – Common steps involved in a decision support system to analyze endoscopic images (from (Liedlgruber and Uhl 2009)).

For example, Wang et al. (2002) proposed a segmentation method applied to endoscopic images based on adaptive histogram thresholding, morphological processing and centroid calculation.

Tjoa et al. (2002) based their approach on color feature hue measure, since colonoscopic images contain rich color information, and it can provide better results for the segmentation of the colonoscopic images than approaches using merely intensity information.

In the 90's decade, Krishnan (1997; 1999) based their work in a procedure, including two steps: image segmentation and labeling. The color image segmentation was based on the histogram analysis using a scale-space filter. From these segmented regions, it was possible to extract some features and attribute a label based on fuzzy rules, i.e. attribute some conditions to the features measured in order to aggregate them. For example, if the area is middleand the mean value of intensity and saturation is low, then the region is classified as lumen.

In what concerns to Capsule Endoscopy, the aim is to analyze all images and identify image frames that contain abnormalities, reducing significantly the examination time by the physician. One example is the detection of Gastrointestinal bleeding that is based on segmentation, histogram thresholding, texture properties (e.g. local binary patterns or variants), histogram based features (Mackiewicz, Berens et al. 2008), or chromaticity moments.

Since the wireless capsule endoscope cannot influence the travel speed and direction, the resulting images have poor quality and pre-processing steps are required.

Finally, concerning to specifically ACF detection, Figueiredo et al. (2010) proposed recently a method to detect ACF in endoscopic images based on partial differential equations, more exactly, active contours without edges (Chan and Vese model). However, there is still much work to do, since there are few articles in the literature reporting image segmentation to detect these structures in endoscopic images *in vivo*.

Summary

Any solution of image processing and analysis is based on two fundamental steps: image enhancement and image segmentation. The first is used to reduce noise, to improve the image quality and enhance contrast. As such, the output image potentiates the detection of the object of interest and simplifies the image segmentation process. It could be divided into two domains: spatial and frequency, processing in the matrix of the input image or after the Fourier transform, respectively.

The image segmentation algorithms try to separate the objects from the image background using different approaches that are essentially based on boundaries and/or regions.

In what concerns to endoscopic images, the problems related to image acquisition and the time spend by physicians motivate the research and application of image processing and analysis algorithms that enhance the image quality and identify frequent pathologies.

The detection of ACF is rarely described in the literature, and since it is indicated as a possible precursor of colorectal cancer, the development and implementation of image processing and analysis methods to detect these lesions will contribute positively to the efficient and fast diagnosis of this disease.

Chapter 4

IMPLEMENTATIONS, RESULTS AND DISCUSSION

4.1. Introduction

The study on image processing algorithms reveals that different approaches have been used to achieve image enhancement and segmentation of the object of interest. In chapter 3, a briefly explanation was made of those techniques. In this chapter, the most relevant methods are explained in more detail and the results of their implementation are presented and discussed.

Considering the human aberrant crypt foci (ACF) endoscopic images used in this project, they were acquired at the Faculty of Medicine of the University of Coimbra and at the Department of Gastroenterology of University Hospital of Coimbra.

Originally, the images were in the RGB domain. However, a large part of the mentioned algorithms cannot be implemented in this domain, since it has three matrixes instead of the common one with the pixels' intensities. Thus, in some cases it was necessary to convert the images to different domains, in particular, to gray scale or to HSI (Hue, Saturation and Intensity) space.

In the RGB model, each color appears in its primary spectral component of red, green and blue. To understand the color distribution, this model is represented in Figure 4.1 as a cube, where the extremities represent one color. Hence, the RGB images are composed of three matrixes, each one representing the intensity of red, green and blue, and from these it is possible to derive other colors.

Although the RGB model is suitable for color display, it is not good for image segmentation and analysis since the components R, G and B are high correlated, that is, if the intensity changes, all the three components are changed accordingly. Also, the measurement of a color in RGB space does not represent color differences in an uniform scale; hence, it is impossible to evaluate the similarity of two colors from their distance in such space (Cheng, Jiang et al. 2001). Considering this, the RGB model could be converted to other models available, as HSI, which separates color information from its intensity.
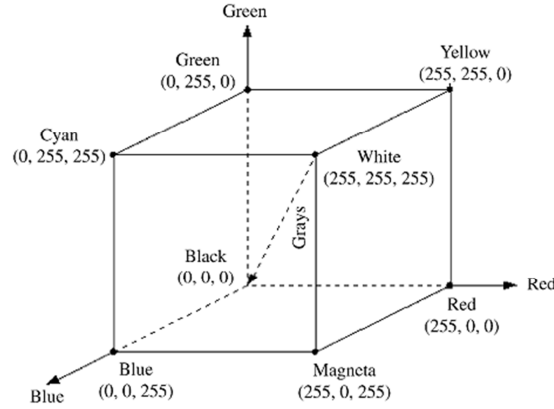
Figure 4.1 – Schematic of the RGB color cube (from (Gonzalez and Woods 2002)).

The HSI model is represented by three matrixes, each one representing Hue, Saturation and Intensity. The color information is contained in hue and saturation values, while the intensity is determined by the amount of light. As a result, the HSI model is an ideal tool for developing image processing and analysis algorithms based on color descriptions (Gonzalez and Woods 2002).

Hue represents basic colors, and is determined by the dominant wavelength in the spectral distribution of light wavelengths. The saturation is a measure of the purity of the color, and signifies the amount of white light mixed with the hue. It is the height of the peak relative to the entire spectral distribution.

The HSI color space can be described geometrically as in Figure 4.2. Generally, hue is considered as an angle between a reference line and the color point in RGB space. The saturation component represents the radial distance from the cylinder center so that the nearer the point is to the center, the lighter is the color. Finally, intensity is the height in the axis direction where zero (minimum) intensity is black and full (maximum) intensity is white.

The HSI coordinates can be obtained from the RGB space using:

$$Hue = arctan\left(\frac{\sqrt{3}(G-B)}{(R-G)+(R-B)}\right), \tag{4.1}$$

$$Intensity = \frac{(R+G+B)}{3}, \tag{4.2}$$

$$Saturation = 1 - \frac{\min(R,G,B)}{I}. \tag{4.3}$$

The hue is undefined if the saturation is zero, and the saturation is undefined when the intensity is zero.

36
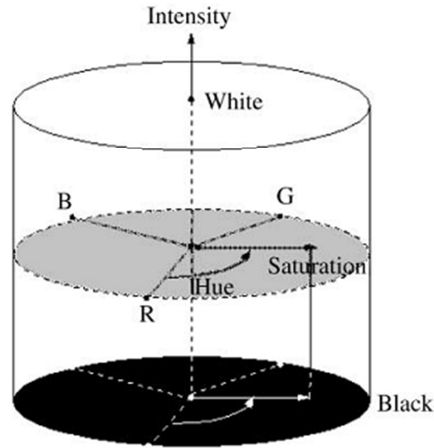
Figure 4.2 – HSI color space (from(Cheng, Jiang et al. 2001)).

Concluding, the image processing algorithms in the HSI domain may be performed only in the intensity matrix, maintaining the color information intact. However, to segment objects with different colors, it could be useful to apply the segmentation algorithms to the hue component only, since it represents the basic colors (Cheng, Jiang et al. 2001).

Another approach used is the conversion of the RGB image to gray scale. In this case, the three matrixes will end up in one representing the intensity in gray levels. The disadvantage of this conversion is that an important part of the image information is lost. However, in this chapter, the image enhancement and segmentation algorithms will be implemented in those two domains and the result will be compared. The conversion is based on a weighted sum of R,G and B components:

$$Gray\ level = 0.2989 \times R + 0.5870 \times G + 0.1140 \times B. \qquad (4.4)$$

An example image in the RGB space, in gray scale and in the HSI space is shown in Figure 4.3. The algorithms' implementations were developed and evaluated in Matlab®.

Figure 4.3 – An endoscopic image in the three domains: RGB (left), gray scale (middle) and HSI (right)

4.2. Image Enhancement

Generally, the medical images have problems with noise, which impoverishes the images' quality and makes the diagnosis a difficult process, particularly when it is automatic, as is intended in this project. The image enh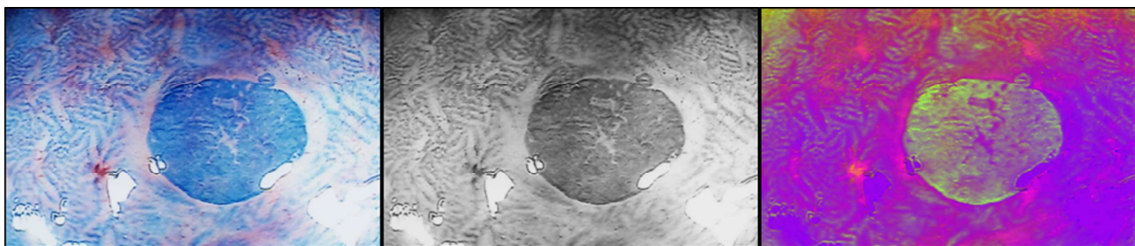ancement could potentiate the segmentation of the object of interest, which corresponds to ACF lesions in this particular study. Considering this, this section explores the capacities of the image enhancement algorithms previously introduced in chapter 3, and evaluate the effects produced by changing their parameters using an endoscopic test image, displayed in Figure 4.3.

4.2.1. Spatial Domain

4.2.1.1. Smoothing

The most common algorithms used to smooth images are: average, Gaussian and median filters. The implementation of these filters is based on a basic linear filtering operation, the convolution. This calculus is done between every pixel and the characteristic mask of the filter. Giving an image $x(n,m)$ and the mask h, the output image $y(n,m)$ is the result of the calculation given by equation 4.5 (see Figure 4.4) where the mask coefficients will be the basis of the filtering desired.

$$
\begin{aligned}
y(n,m) = {}& h(1,1) \times x(m-1,n-1) + h(1,0) \times x(m-1,n) + h(1,-1) \\
& \times x(m-1,n+1) + h(0,1) \times x(m,n-1) + h(0,0) \times x(m,n) \\
& + h(0,-1) \times x(m,n+1) + h(-1,1) \times x(m+1,n-1) \\
& + h(-1,0) \times x(m+1,n) + h(-1,-1) \times x(m+1,n+1)
\end{aligned}
$$

(4.5)
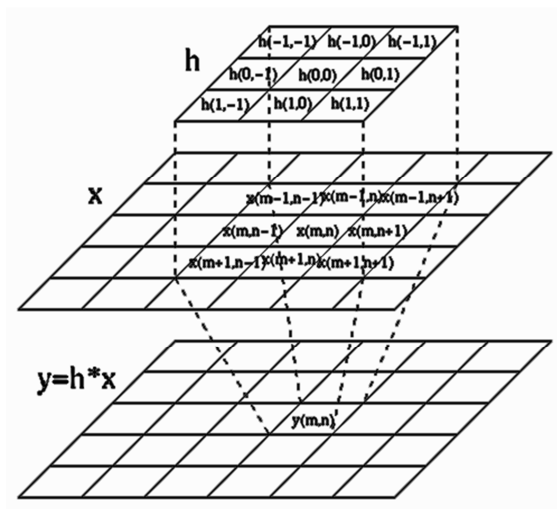
Figure 4.4 – The convolution operation (from (Wang 2009)).

38

The average filter computes the sum of the pixels in the local neighborhood established and divides by the total number of pixels in use. The mask filter of size 3x3 is represented in Figure 4.5a. The mask size is a parameter that could be changed and that directly influences the filters' result.

The Gaussian filter is similar to average, but attributes different weights to the pixels in the neighborhood, following a normal distribution. Moreover, it depends on the standard deviation and mask size to smooth more or less the image. An example of mask coefficients is presented in Figure 4.5b.
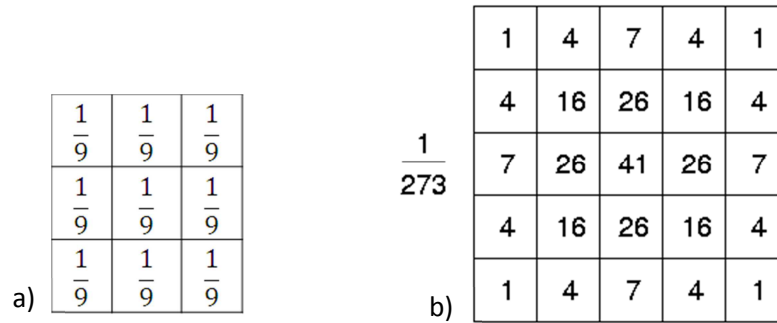
Figure 4.5 – Masks used in average (a) and Gaussian (b) filtering.

The Gaussian filter is characterized by a bell shape curve dependent on mean and standard deviation σ:

$$G(x,y) = \frac{1}{2\pi\sigma^2} e^{-\frac{x^2+y^2}{2\sigma^2}},$$
(4.6)

where x is the distance from the origin in the horizontal axis and y in the vertical axis. As the standard deviation increase, the Gaussian curve is larger, Figure 4.6.
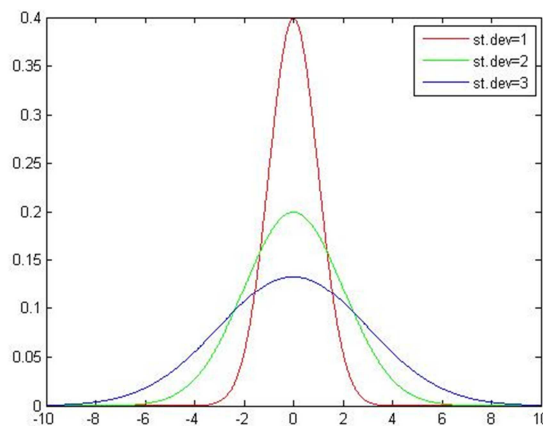
Figure 4.6 – The influence of standard deviation on Gaussian curve.

The median filter is based on different assumptions, Figure 4.7. The use of this algorithm is very valuable when in the presence of high intensity noise or outliers, as, for example, the "salt and pepper" noise, since the highest and lowest intensity levels are usually removed.
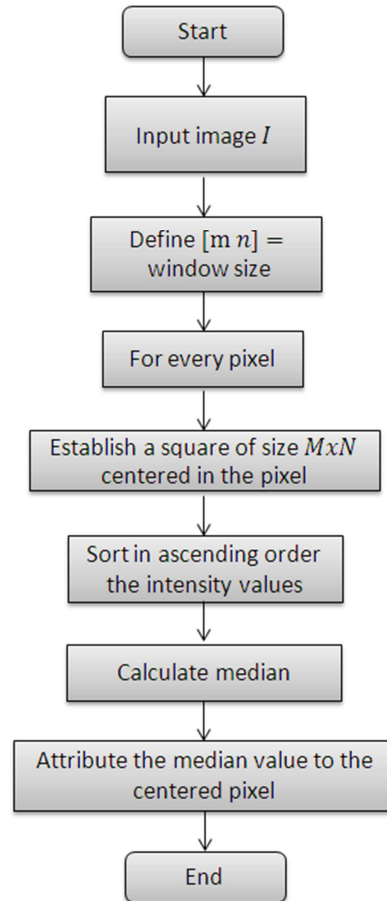
Figure 4.7 – Flowchart of median filter.

The mask size variation plays an important role in the smooth intensity of the filter. The results represented in Figure 4.8 for the three different filter algorithms have the same conclusion: as the mask size increase, the image becomes smoother, in a direct proportionality. However, the Gaussian filter seems to be almost invariant as the mask size increase. This is related to the fact that sigma (standard deviation) parameter plays a central role in the Gaussian filter, having a direct proportionality with smoothness, i.e., the increase of sigma leads to smoother images, as can be seen in Figure 4.9. The results show just a small part of the original image in order to visualize better the smooth effect.

| Mask size | [3 3] | [5 5] | [10 10] | [20 20] |
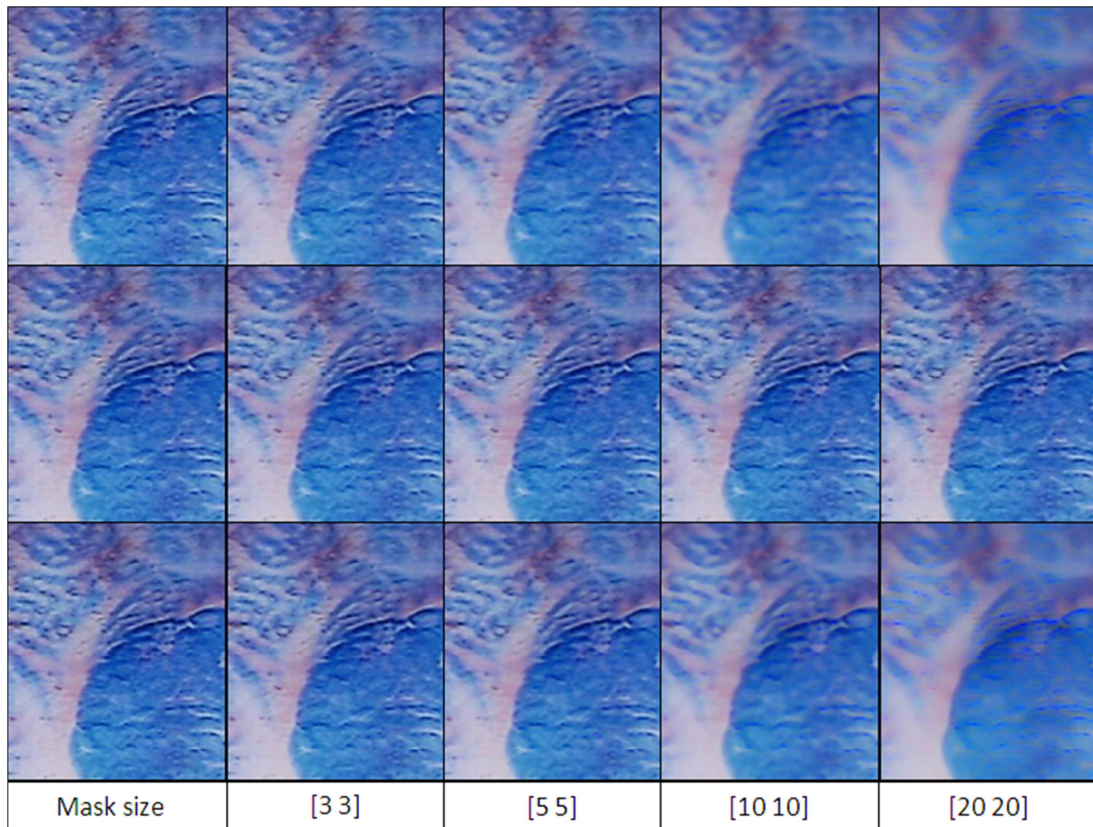
Figure 4.8 – The influence of mask size in average (1st row), Gaussian (2nd row) and median filters (3rd row).

| Sigma | 0.5 | 5 | 10 |
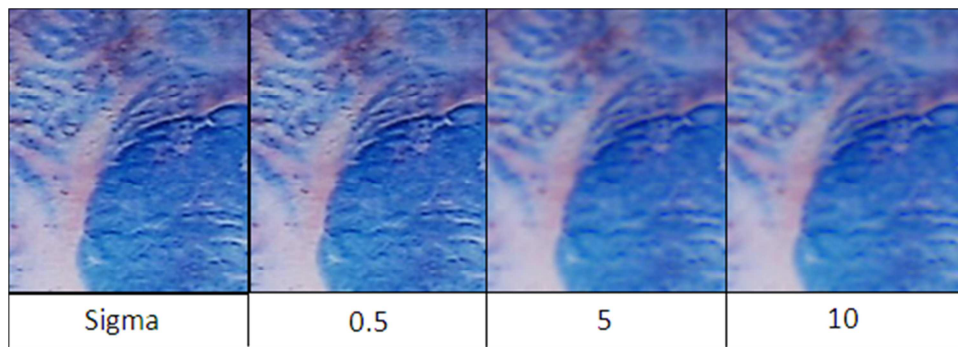
Figure 4.9 – The influence of sigma in the Gaussian filter.

4.2.1.2.   Sharpening

The methods used to sharp the images, turning the edges more evident, are commonly divided into two main equations: the first and second order derivatives.

The first order derivative function of $f(x, y)$ is defined as:

$$\frac{\partial f}{\partial x} = f(x + 1) - f(x).$$

(4.7)

When it is computed at location x, the value of the function at that location is subtracted from the next point. As such, when the neighbor pixels have similar intensity values, the function generates null responses while in transitions it responds positively.

First derivatives in image processing are implemented using the magnitude of the gradient. For a function $f(x, y)$, the gradient of f at coordinates (x, y) is defined as the two-dimensional column vector:

$$\nabla f = \begin{bmatrix} g_x \\ g_y \end{bmatrix} = \begin{bmatrix} \frac{\partial f}{\partial x} \\ \frac{\partial f}{\partial y} \end{bmatrix}. \tag{4.8}$$

This vector provides information about the direction of the greatest rate of change of f at location (x, y). Moreover, the magnitude of the vector can be calculated to indicate the rate of change value at each pixel in the image:

$$M(x, y) = \sqrt{g_x^2 + g_y^2}. \tag{4.9}$$

Sobel operator is an example of a first derivative method and it operators through mask convolution with the input image. It has two convolution masks, one oriented horizontally and another one vertically, g_x and g_y, respectively. When applied on an original image, the resulting magnitude image enhances the edges and intensity transitions, and neutralizes the homogeneous regions, Figure 4.10.
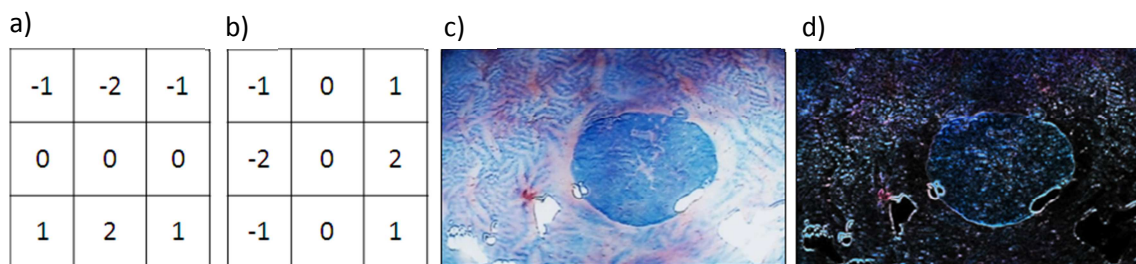
Figure 4.10 – Sobel sharpening filter: a) and b) horizontal and vertical masks, respectively; c) original input image; d) output image.

In this case, the resultant image had the intensity variations quite well distinguished. However, this algorithm is not a good option when in the presence of noisy images since it emphasizes the high intensity values.

Another approach frequently used to perform image sharpening is the second order derivative. The definition of this function $f(x, y)$ is:

$$\frac{\partial^2 f}{\partial x^2} = f(x+1) + f(x-1) - 2f(x). \tag{4.10}$$

The non-null responses of this derivative occur in transitions of the first order derivative. The simplest derivative operator is the Laplacian, which, for an image $f(x, y)$ is defined as:

$$\nabla^2 f = \frac{\partial^2 f}{\partial x^2} + \frac{\partial^2 f}{\partial y^2}. \tag{4.11}$$

To express this equation in its discrete form, it is divided in two directions. In the x direction it is:

$$\frac{\partial^2 f}{\partial x^2} = f(x+1, y) + f(x-1, y) - 2f(x, y), \tag{4.12}$$

and, similarly, in the y direction it is defined as:

$$\frac{\partial^2 f}{\partial y^2} = f(x, y+1) + f(x, y-1) - 2f(x, y). \tag{4.13}$$

The junction of the equations 4.11, 4.12 and 4.13 defines the discrete Laplacian with two variables as:

$$\nabla^2 f(x, y) = f(x+1, y) + f(x-1, y) + f(x, y+1) + f(x, y-1) - 4f(x, y). \tag{4.14}$$

This equation could be implemented using the mask shown in Figure 4.11a.

a)

-1	-1	-1
-1	8	-1
-1	-1	-1

b)

c)

Figure 4.11 – Laplacian sharpening filter: a) mask; b) original image; c) filtered image.

In the experimental image that has been used up to now, the results obtained with the Laplacian filtering are similar to Sobel, but with less noise and thinner edges.

4.2.1.3. Unsharp Masking

As mentioned by Liedlgruber (2009), the endoscopic images acquired are sometimes blurred since the current endoscopes do not provide the ability to focus. Hence, the edges enhancement could assist the identification of ACF lesions from the images' background.
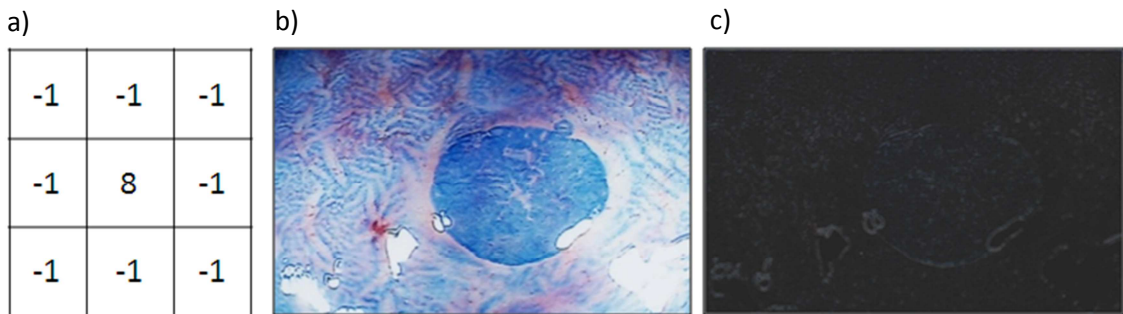
The Unsharp Masking (UM) algorithm is a widely used technique for improving the perceptual quality of an image by emphasizing its high-frequency components (Polesel, Ramponi et al. 1997). It can be described by equation 4.15, where $y(n,m)$ is the enhanced image, $x(n,m)$ is the input image, $z(n,m)$ is the correction signal computed as the output of a linear high pass filter, and λ is a suitable positive scaling factor which controls the contrast enhancement at the output.

$$y(n,m) = x(n,m) + \lambda z(n,m) \qquad (4.15)$$

The simplest implementation of this method is traduced in three steps:

1. Blur the original image;
2. Subtract the blurred image from the original (the difference is called the mask);
3. Add the mask to the original, with a specified weight.

It was developed an implementation in Matlab® consisting of these three steps, using two different domains, grey-scale and HSI, as previously referred.

The first step was performed by a Gaussian filter, that is, a low pass filter that smooths the edges and blurs the image, as explained in section 4.2.1.1. To use this filter, it is necessary to define the mask size and standard deviation. In the experimental evaluation done, the best results were obtained using a mask size of 10 pixels and sigma 20, for an image with size 741x1170 pixels.

To understand the influence of the parameter λ, the method was used adopting λ equal to 0.5, 1 and 2, Figure 4.12. The results obtained show that the unsharp is more evident as λ increases, i.e., when the mask component of the equation 4.15 has more weight. However, the global application of Unsharp masking to image processing makes the method extremely sensitive to noise, enhancing not just the region of interest, but the whole image.

The answer to this problem was first proposed by Polesel et al. (1997), who based their approach in an adaptive algorithm that change the value of the scaling factor λ at each location, according to the intensity values of the pixels in a neighborhood. Bae et al. (2003) suggested a new fast adaptive unsharp masking algorithm, which was the basis of the implementation developed in Matlab®, Figure 4.13.

The main difference between the global and local approach is based on λ calculation. The algorithm implemented initiated with Sobel filtering, obtaining the gradient magnitude. Then, it was followed by maximum filtering, which selected the maximum magnitude value in a 3x3 pixels neighborhood. Finally, the nonlinear function used was a median filter (5x5 window size), that eliminated local noise. In Figure 4.14, the results of Adaptive UM in comparison to Global UM are represented.

The adaptive algorithm reduced significantly the undesired enhance. However, the object of interest (ACF lesion) boundary is less evident.
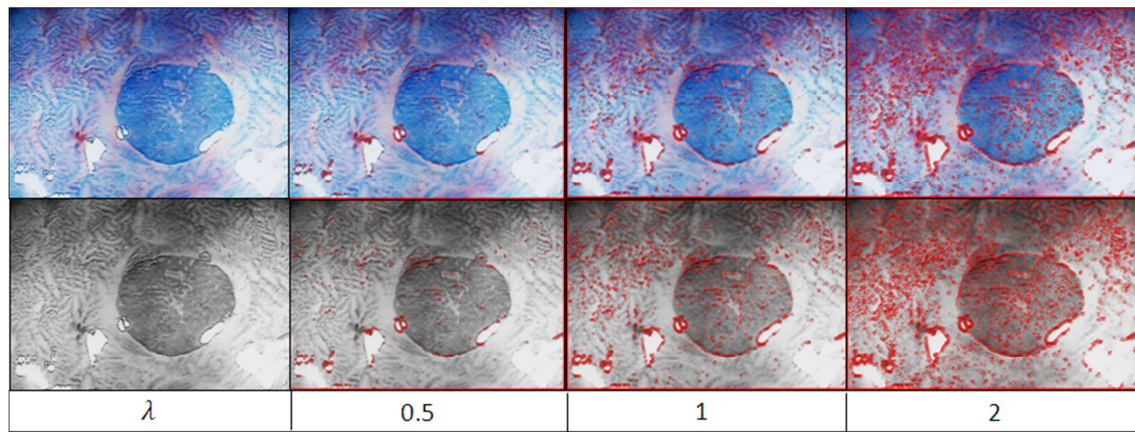
Figure 4.12 – Unsharp masking implementation in the HSI domain, with results in RGB domain (first row), and gray scale (second row). (The results in red evidence the difference between the input and output image.)
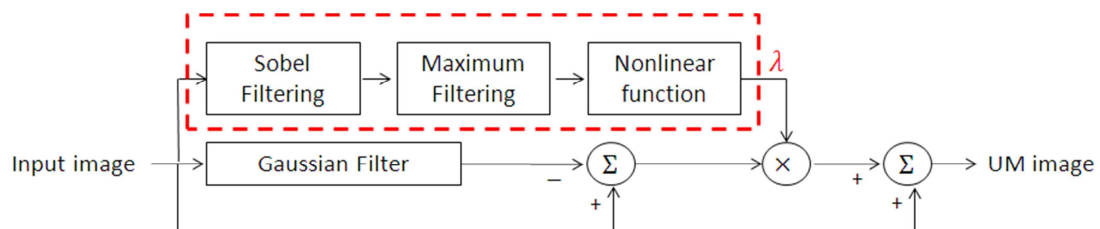
Figure 4.13 – An adaptive Unsharp masking algorithm (adapted from (Bae, Shamdasani et al. 2003)).
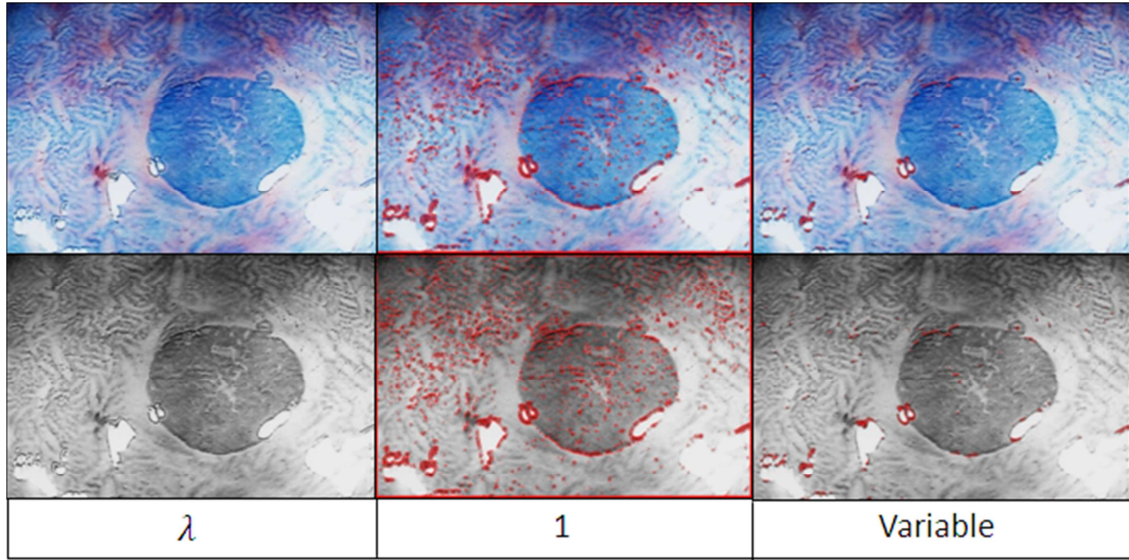
Figure 4.14 – Results of Unsharp Masking (2nd column) and Adaptive Unsharp Masking (3rd column) filtering.

4.2.1.4. Thresholding

The histogram is a powerful measure of the intensity level occurrences in an image. In some cases, there are distinct intensities associated with the image background and foreground (object of interest), representing two separate groups visible in the histogram. In such cases, threshold is the limit defined from which every pixel with intensity values superior to that will be, for example, zero (black) and all the others will be one (white). The mathematical expression that traduces this technique is:

$$g(m,n) = \begin{cases} 0 \; if \; f(m,n) \leq L1 \\ f(m,n) \; if \; f(m,n) > L1' \end{cases} \tag{4.16}$$

where $g(m,n)$ is the output image, $f(m,n)$ is the input image and $L1$ is the threshold established or determined automatically.

When the object of interest is in a specified window of intensity values, the threshold can be performed according to equation 4.17, where $f1$ and $f2$ define the region of interest:

$$g = \begin{cases} 0 \; if \; f(m,n) \leq f1 \\ \frac{f(m,n)-f1}{f2-f1} \; if \; f1 < f(m,n) < f2. \\ 0 \; if \; f(m,n) > f2 \end{cases} \tag{4.17}$$

46

The algorithm developed traverses all pixels in the image, comparing their values to the threshold establish. According to the comparison result, they acquire a new level.

The threshold value could be determined manually or automatically, using the method proposed by Otsu (1979). This algorithm computes image histogram and probability of each intensity level and exhaustively search for the threshold that minimizes the intra-class variance, defined as a weighted sum of variances of the two classes. The classes are the intensity groups separated by the threshold value.

In Figure 4.15, the implementation of the thresholding technique, which was developed in this project, was performed in Matlab®, at two different levels. The manually choice of threshold was 0.5 and 0.8 and it was based on the histogram appearance, since the valleys usually indicate the separation between two regions. On the other hand, after applying the Otsu's algorithm, it was obtained a threshold value of 0.58, corresponding to one of the valleys.

The results obtained in this experimental case did not contribute positively to image enhancement, since the background presents significant luminance variations.
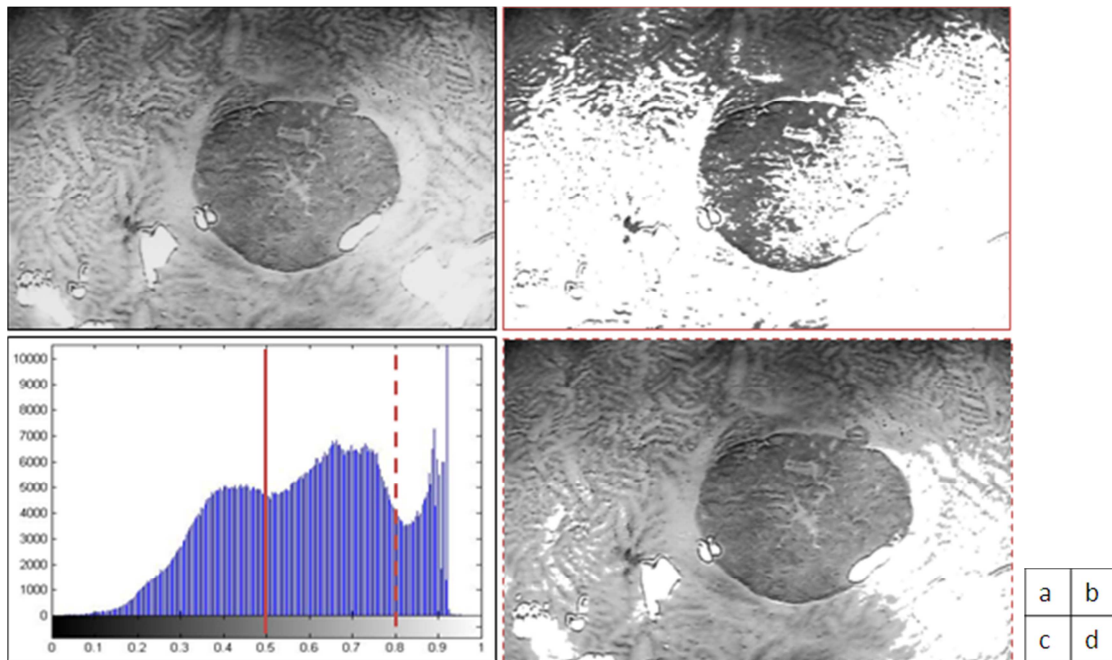

Figure 4.15 – Thresholding use with two different threshold values: a) original gray image; b) image with 0.5 threshold; c) histogram of input image; d) image with 0.8 threshold.

In what concerns to windowing threshold, Figure 4.16, the best result was obtained using values between 0.1 and 0.7. However, as noticed previously, this technique did not improve

the quality of the test image. In fact, thresholding do not have the capacity to eliminate noise, but it can contribute to contrast enhancement.

a)   b)   c)
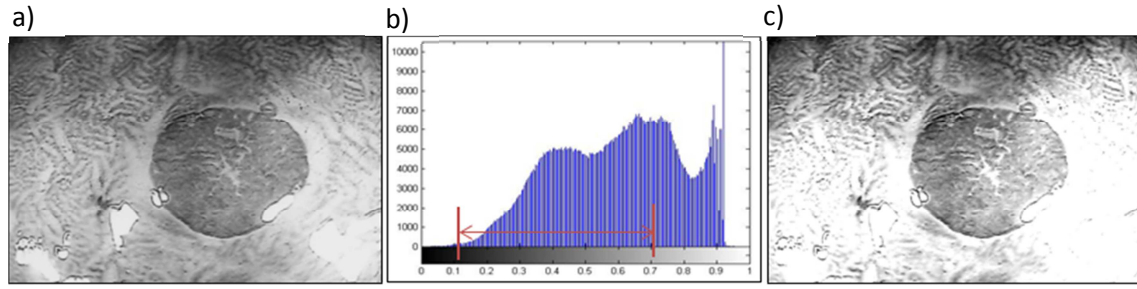
Figure 4.16 – Using a threshold windowing between 0.1 and 0.7: a) input gray image; b) histogram; c) thresholded image.

The problems encountered with the luminance variance of the input image background can be overcome if an adaptive method is used; this approach is exploited in the section concerning image segmentation algorithms.

4.2.1.5.   Histogram Equalization

The histogram equalization method is used to increase the global contrast of an image, since the intensities are better distributed on the histogram. This method is particularly useful when the image background and foreground have the similar luminosity. The main advantage of this technique is the contrast image enhancement in a straightforward technique, that is, if the histogram equalization function is known, then the original histogram can be recovered. However, it does not discriminate the background from the region of interest, and it may increase the contrast of the background noise and decrease the foreground perception.

The implementation of this algorithm is based on some mathematical assumptions.

Consider an image $f(n, m)$ of size $M \times N$ pixels with gray levels $l = 0, 1, 2, \dots L - 1$. The histogram of the image may be defined as:

$$P_f(l) = \sum_{m=0}^{M-1} \sum_{n=0}^{N-1} \delta_d[f(m, n) - l], \qquad 0 \leq l < L - 1, \qquad (4.18)$$

where the function δ_d is defined as:

$$\delta_d(k) = \begin{cases} 1 \ if \ k = 0 \\ 0 \ otherwise \end{cases}. \qquad (4.19)$$

Thus, the function $P_f(l)$ provides the number of pixels in the image $f(m,n)$ that possess the gray level l. In order to normalize the gray levels in the histogram, they are divided by the maximum value available, as $r = \frac{l}{L-1}$, such that $0 \leq r \leq 1$. Hence, the $p_f(r)$ represents the normalized histogram or the probability density function (PDF).

If one wants to apply the transformation $s = T(r)$ to the random variable r, it is given by:

$$s = T(r) = \int_0^r p_f(w)dw; \quad 0 \leq r < 1. \tag{4.20}$$

This is the cumulative (probability) distribution function of r.

In what concerns to the discrete version, the histogram equalization is approximated by:

$$s_k = T(r_k) = \sum_{i=0}^{k} p_f(r_i) = \sum_{i=0}^{k} \frac{n_i}{P}; \quad k = 0,1,\dots,L-1, \tag{4.21}$$

where $P = MN$, representing all the pixels of the image $f(n,m)$ and k is the variable which includes all gray levels. The output image will attribute new intensity levels based on the cumulative distribution function that is equal to s_k (Rangayyan 2005).

The global application of histogram equalization clearly enhances the images' contrast, as can be verified in Figure 4.17. However, since the image background has a varied luminosity, the local version of this algorithm can improve the aim of this method.
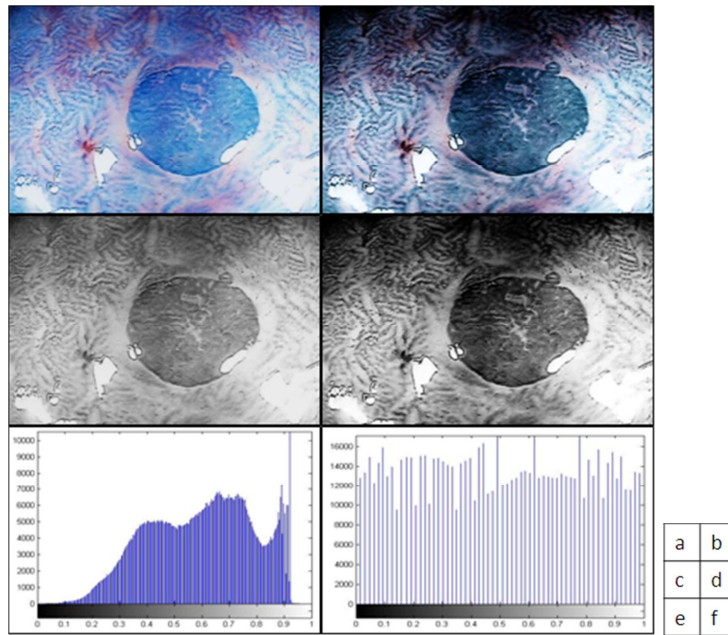

Figure 4.17 – Using the Histogram equalization algorithm: a)Original RGB image; b) output image using HSI processing; c) original gray image; d) output image with gray scale processing; e) input image histogram; f) output image histogram.

The adaptive histogram equalization uses the same function as the global application but applied in a local window that acts through all pixels. The transformation is based on local histogram, centered at the current pixel being processed and the resulting transform is applied only to the central pixel (Pizer, Amburn et al. 1987). In this method, the contrast enhancement mapping is a function of the intensity values immediately surrounding the pixel, so that the number of times that this calculation should be repeated is the same as the number of pixels in the image. Hence, it is computationally demanding (Reza 2004) and despite the advantages of local processing, this method has some problems when in the presence of areas with uniform intensity. In these cases, the contrast should not be amplified in order to avoid noise enhancement. Considering this, there is an alternative algorithm that limits the contrast obtained by histogram equalization and is called Contrast Limited Adaptive Histogram Equalization (CLAHE) and has produced good results on medical images.

The fundamental steps of the CLAHE algorithm are (Garg, Mittal et al. 2011):

1. <u>Obtain all the inputs:</u> Image, Number of regions in row and column directions, Number of bins for the histograms used in building image transform function (dynamic range), Clip limit for contrast limiting (normalized from 0 to 1);

2. <u>Pre-process the inputs:</u> Determine real clip limit from the normalized value if necessary, pad the image before splitting it into regions;

3. <u>Process each contextual region (tile) thus producing gray level mappings:</u> Extract a single image region, make a histogram for this region using the specified number of bins, clip the histogram using clip limit, create a mapping (transformation function) for this region;

4. <u>Interpolate gray level mappings in order to assemble final CLAHE image:</u> Extract cluster of four neighboring mapping functions, process image region partly overlapping each of the mapping tiles, extract a single pixel, apply four mappings to that pixel, and interpolate between the results to obtain the output pixel; repeat on the entire image.

The Matlab® implementation used was based on the one proposed by Zuiderveld (1994).

There are three important parameters that could be selected: tiles number, distribution and clip limit. At first, tiles number represents the window size of the local operations. This parameter was evaluated using the test image, Figure 4.18, and it can be observed that as the size increased, the contrast was more uniform, which was expected since the equalization is more homogeneous when window size includes distinct regions. The best result was obtained with the size 40x40.

| Tiles number | [8 8] | [40 40] | [80 80] |
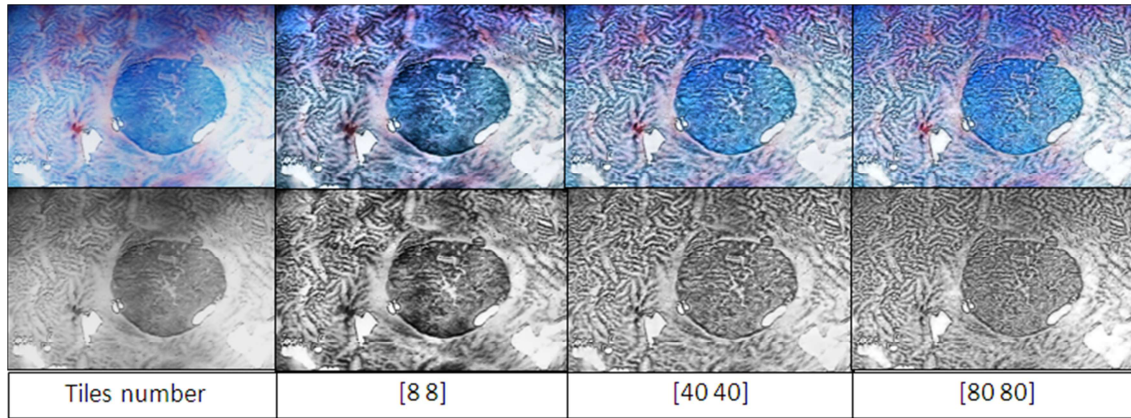
Figure 4.18 – The influence of tiles number in the CLAHE algorithm using HSI domain (1st row) and gray scale (2nd row).

The distribution parameter includes three types available in the algorithm proposed by Zuiderveld (1994): Uniform, Rayleigh and Exponential. These distributions allow the histogram to have different shapes.

The uniform distribution equalizes the histogram using all the gray levels with approximately the same probability. The Rayleigh distribution has a histogram with bell shape, giving more importance to median gray level intensities. In what concerns to exponential, the histogram has an ascendant shape, increasing the overall luminosity of the image. The application of different distributions to the endoscopic test image resulted in small differences between them, so in the further experiments was adopted the default uniform distribution.

Finally, the 3rd parameter is the clip limit, a contrast factor that prevents over-saturation of the image specifically in homogeneous areas. These areas are characterized by a high peak in the histogram of the particular image tile due to many pixels falling inside the same gray level range. The default value used was 0.01, which produced the images shown in Figure 4.18. As clip limit increases, the contrast also increases but the image information is lost. As such, smaller values for this parameter were experimented, Figure 4.19.

| Clip limit | 0.001 | 0.005 | 0.01 |
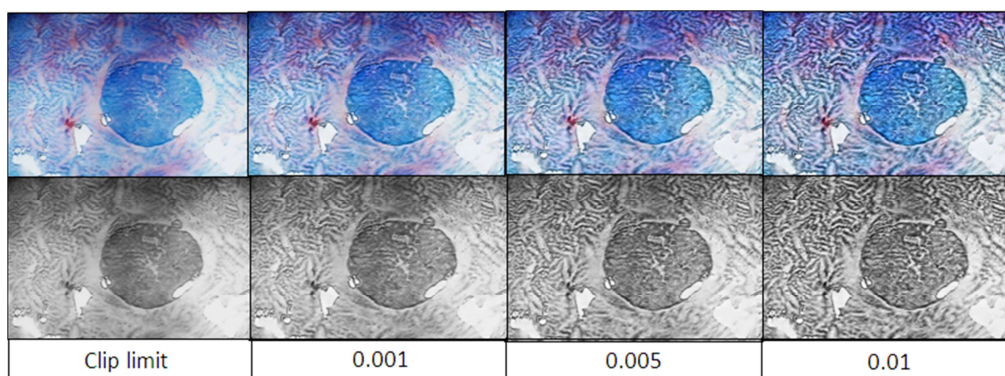
Figure 4.19 – The influence of clip limit in CLAHE algorithm, using HSI domain (1st row) and gray scale (2nd row).

According to the image under analysis and the results expected, the clip limit should be used higher for more contrast.

4.2.1.6. Histogram Stretching

The histogram stretching algorithm is a simple method used to enhance contrast. In some cases, the image represented is using only part of the gray levels available. This technique stretches the histogram of the original image so that all the gray levels available are used.

The algorithm flowchart of this algorithm is shown in Figure 4.20, and a result example is presented in Figure 4.21.
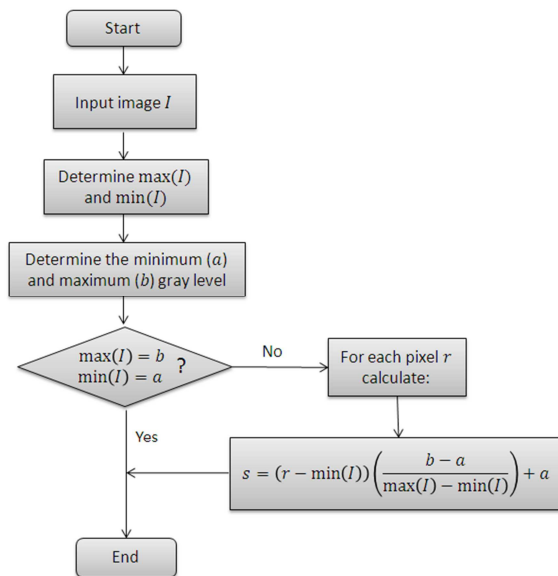
Figure 4.20 – Histogram stretching flowchart.
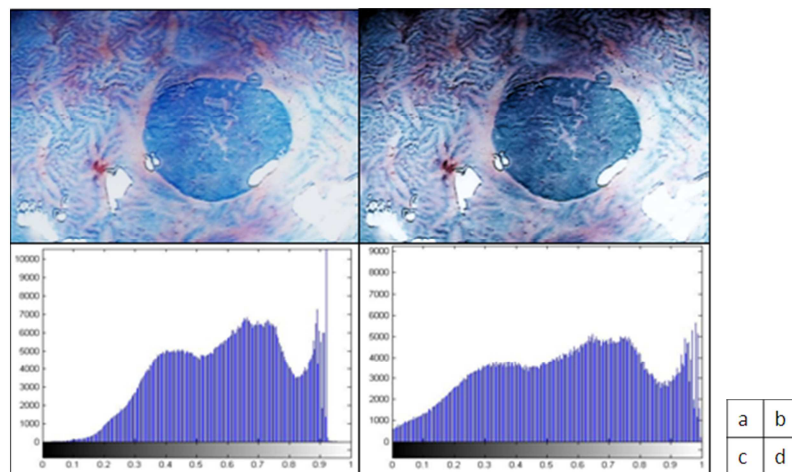
Figure 4.21 – Result of histogram stretching: a) original image; b) output image;
c) original histogram; d) output image histogram.

4.2.1.7. Morphological Processing

The essence of mathematical morphology is comprised of a set algebra consisting of four basic transformations: erosion, dilation, opening and closing (Schonfeld 1991). These techniques are suitable for extracting image features that are useful in representing and describing region shapes. Information about the objects' size, shape, connectivity, smoothness and orientation can be obtained by using various structuring elements and morphological operators (Pitas 1993). Morphological operations apply a structuring element to an input image, creating an output of the same size. In a morphological operation, the value of each pixel in the output image is based on a comparison of the corresponding pixel in the input with its neighbors, Figure 4.22. By choosing the size and shape of the neighborhood, one can construct a morphological operation that is sensitive to specific shapes in the input image.

The most basic morphological operations are dilation and erosion. Dilation adds pixels to the boundaries of objects in an image, while erosion removes pixels on objects' boundaries. The number of pixels added or removed from the objects in an image depends on the size and shape of the structuring element used to process the image (Mathworks 2011).

The dilation and erosion respond in opposite ways, i.e., the output pixel of dilation is the maximum value of all the pixels in the neighborhood, while in erosion it outputs the minimum value.
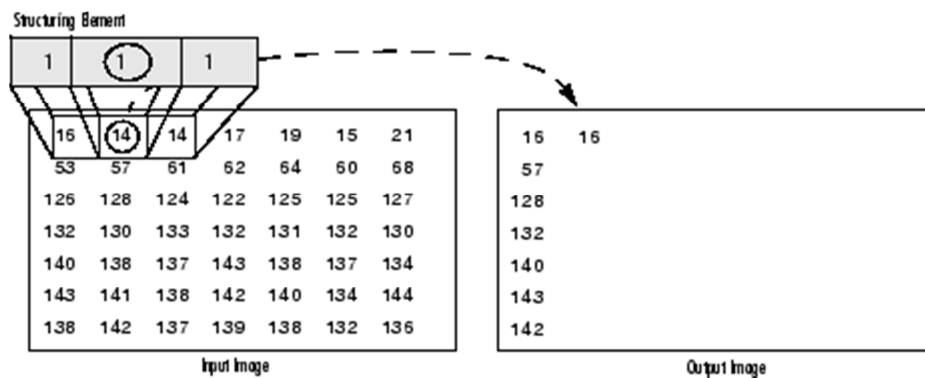
Figure 4.22 – Morphological dilation of a grey scale image (from (Mathworks 2011)).

Based on dilation and erosion arises two more morphological operations: opening and closing. As seen, dilation expands the components of an image and erosion shrinks them; however, to maintain the same size, opening and closing are the best solution.

Opening consists in erosion followed by dilation with the same structuring element. The particular interest of this operation consists on the elimination of isolated points without changing the objects' size in the image.

Closing has the opposite operation, i.e., it consists on dilation followed by erosion. The principal advantage of this operation is to join neighboring objects and then return to same or similar size of the regions.

The structuring elements can have diverse shapes and sizes, resulting in images smoothed or sharped according to the parameters and the morphological operations chosen. To understand the influence of these parameters, the dilate operation was used with a 'disk' shape structuring element available in Matlab® function *strel* and adopting different dimensions, Figure 4.23.
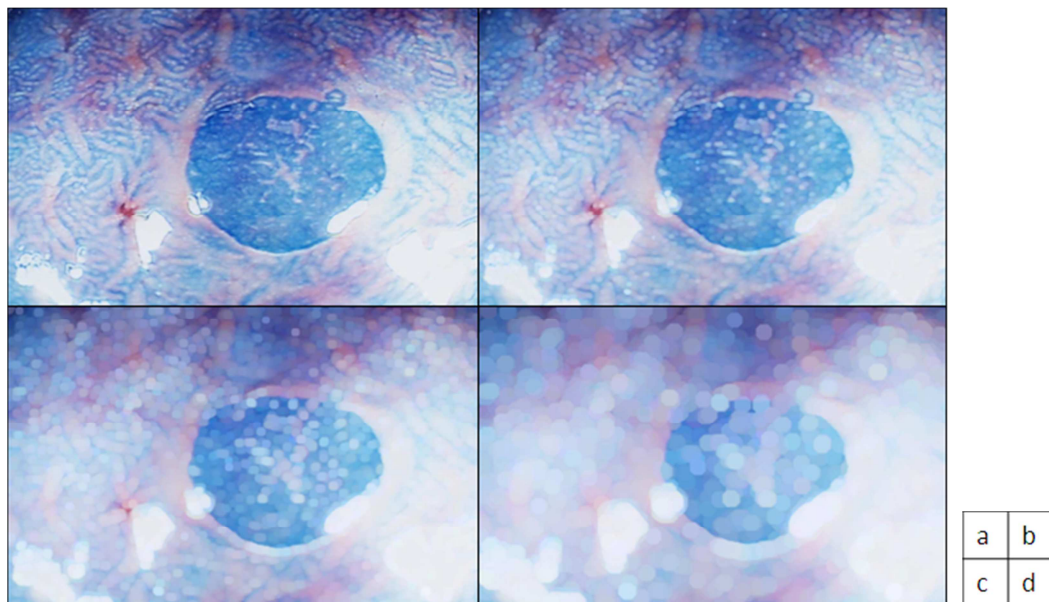
Figure 4.23 – The result of a morphologic dilation with a 'disk' shape structuring element of size: a) 2, b) 5, c)10 and d) 20.

The results suggested that as the structuring element size increases, more effect it has on the image, and the output image starts to show more clearly the shape chosen, in this case, the disk shapes.

The results of the four morphological operations can be compared from the images in Figure 4.24. From figure, one can realize that, depending on the operation, the image became smoother (dilation and closing) or sharper (erosion and opening). Hence, these operations can be useful to enhance objects of interest and to eliminate speckle noise.
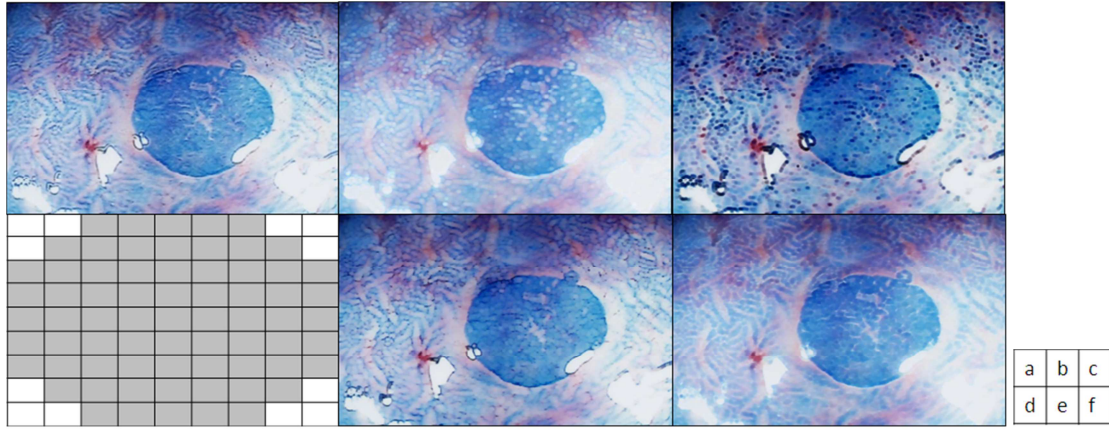
Figure 4.24 – Comparison of the four principal morphologic operations: a) original image; b) result after dilation, c) result after erosion; d) the structuring element shape used; e) result after open; f) result after close.

4.2.2. Frequency Domain

The frequency domain techniques are performed after the input image is converted by the Fourier transform, which is defined by equation 4.22, where $f(t)$ is a continuous function and μ is a continuous variable.

$$\Im\{f(t)\} = \int_{-\infty}^{+\infty} f(t)e^{-2j\pi\mu t}dt \qquad (4.22)$$

After transforming the input image into its frequency representation, the image processing is performed, finalizing with the computation of the inverse transform to return to the spatial domain.

In the frequency domain, the values should be interpreted in a different way, since the filtering process does not act directly on pixels' intensity values. However, some general statements can be made about the relationship between the frequency components of the Fourier transform and spatial features of an image. At first, the slowest varying frequency component is proportional to the average intensity of an image. Moreover, the low frequencies correspond to the slowly varying intensity components of an image while the higher frequencies correspond to faster intensity changes, i.e., regions with abrupt intensity changes.

Considering these properties, the frequency filtering can enhance the images according to the filter applied as it is discussed in the following sections.

4.2.2.1. Frequency Filtering

Filtering in the frequency domain consists of processing the Fourier transform of the input image and then computing the inverse transformation to obtain the filtering result. Hence, for a digital image $f(x, y)$, of size $M \times N$, the basic filtering equation is defined as:

$$g(x, y) = \Im^{-1}[H(u, v)F(u, v)], \tag{4.23}$$

where $\Im^{-1}$ is the inverse Fourier transform, $F(u, v)$ is the input image after the Fourier transform, $H(u, v)$ is a filter function and $g(x, y)$ is the output image, being all images of size $M \times N$ (Gonzalez and Woods 2002).

The filtering process, Figure 4.25, returns a different output image according to the filter used. There are two fundamental filters that promote smoothing and sharpening: Low pass and High pass, respectively.
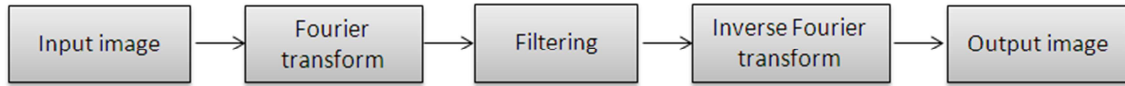
Figure 4.25 – Usual frequency filtering process.

A low pass filter attenuates all frequencies higher than the cutoff frequency established. Since the edges and other sharp intensity transitions (such as noise) contribute to the high frequency content, their attenuation generates smoothed (blurred) images. There are three categories of low pass filtering: Ideal, Gaussian and Butterworth.

The ideal low pass filter multiplies all the values inferior to the cutoff frequency by the filter function $H(u, v) = 1$, while the superior values will be multiplied by $H(u, v) = 0$, attenuating completely those frequencies and obtaining a transition represented as a vertical line, Figure 4.26 (left).

The cutoff frequency is defined as a circle of radius D_0 from the origin that attenuates all the frequencies outside this radius:

$$H(u, v) = \begin{cases} 1 & if \ D(u, v) \leq D_0 \\ 0 & if \ D(u, v) > D_0 \end{cases} \tag{4.24}$$

where D_0 is a positive constant and $D(u, v)$ is the distance between a point (u, v) in the frequency domain and the center of the frequency rectangle, that is equal to:

$$D(u,v) = \sqrt{(u - P/2)^2 + (v - Q/2)^2},\tag{4.25}$$

where P and Q are the padded sizes, i.e., the discrete frequency variables are in the range $u = 0,1,2,\dots,P-1$ and $v = 0,1,2,\dots,Q-1$. However, it is clear that ideal low pass filtering is not very practical.

The Gaussian low pass filter is based on the normal distribution graph, Figure 4.26 (middle), i.e., the attenuation is not as abrupt as the ideal filter, but decreases softly until the frequencies are totally annulated. The filter can be express as:

$$H(u,v) = e^{-D^2(u,v)/2D_0^2},\tag{4.26}$$

where D_0 is the cutoff frequency, and when $D(u,v) = D_0$ the filter is down to 0.607 of its maximum value.

Finally, the Butterworth low pass filter is characterized by a curve with oscillations, Figure 4.26, and its transfer function of order n and cutoff frequency D_0 is given as:

$$H(u,v) = \frac{1}{1+[D(u,v)/D_0]^{2n}}.\tag{4.27}$$

As the filter order increases, the oscillation rises, causing the appearance of ringings in the spatial domain. As such, the order 2 generates a good compromise between effective low pass filtering and acceptable ringing.

Concluding, the tree types of low pass filter, Figure 4.26, cover the range from very sharp (ideal) to very smooth (Gaussian) filtering, with the Butterworth in the intermediate behavior since the defined order could produce the effect desired.
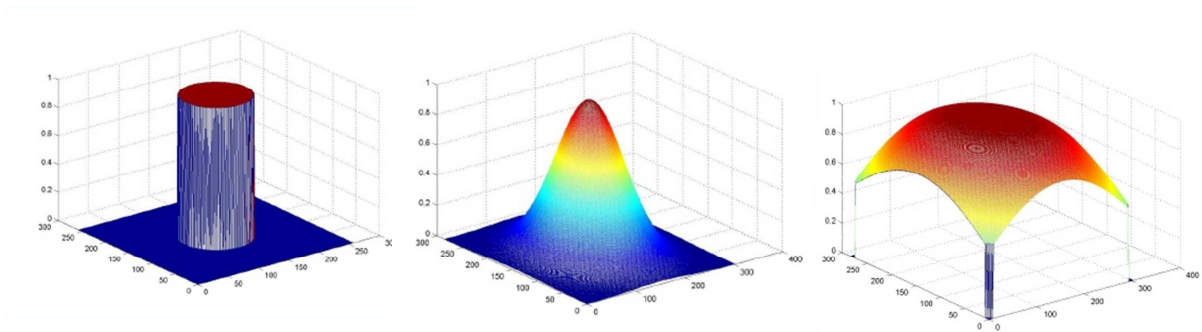
Figure 4.26 – Perspective plots of ideal (left), Gaussian (middle) and Butterwhorth (right) low pass filter of order two filters (from(Gonzalez and Woods 2002)).

The High pass filters are also divided into these three types. However, they act In opposite ways, attenuating the low frequencies and enhancing edges and sharp intensity transitions (Gonzalez and Woods 2002). To obtain the high pass filter transfer function, $H_{HP}(u,v)$, it is only necessary to perform the operation described as:

$$H_{HP}(u,v) = 1 - H_{LP}(u,v). \qquad (4.28)$$

The results displayed in Figure 4.27 did not show visible differences between the three types of low pass filters. In what concerns to cutoff frequency, as it decreased, the image became smoother. When it was used a high pass filter, the effect was different, that is, as the cutoff frequency decreased, the image became sharper.
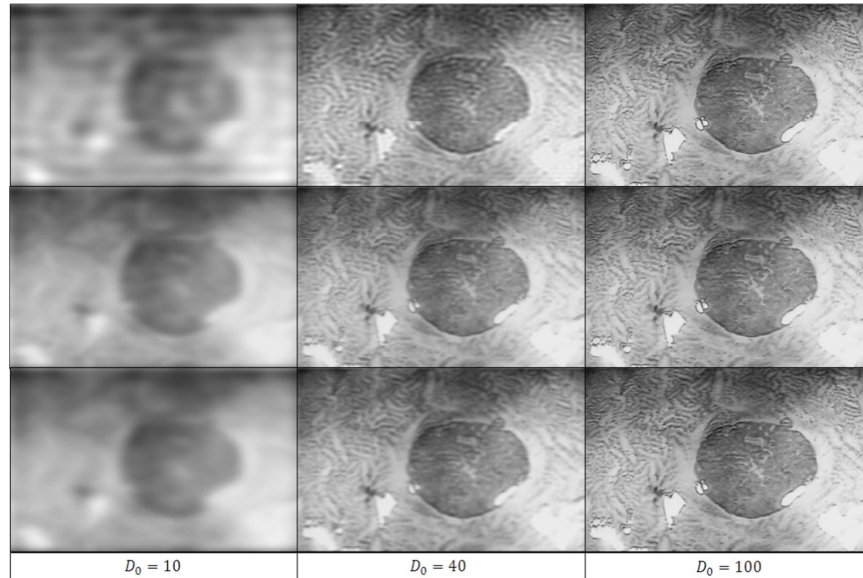
Figure 4.27 – Influence of the cutoff frequency in the ideal (1st row), Gaussian (2nd row) and Butterworth (3rd row) low pass filters.

Concluding, these methods generated results similar to those obtained in smoothing and sharpening in the spatial domain (section 4.2.1). Hence, there was not an important advantage in processing the test image with low and high pass filters in the frequency domain.

4.2.2.2. Homomorphic Filtering

The Homomorphic filtering based their approach in the information of illumination and reflectance. As mentioned in section 3.3.2, it uses the logarithm to implement the filtration, so that the two components of the test image could be used.

This filter allows the control of the low and high frequency image components, attenuating the contribution made by the low frequencies (illumination) and amplifying the contribution made by high frequencies (reflectance). Hence, the result will be simultaneous dynamic range compression and contrast enhancement (Gonzalez and Woods 2002).

Ahmed (2008) proposed a Matlab® implementation that uses a Butterworth low pass $H(u, v)$ function that filters the input image, after performing logarithm and Fourier transform. The output image, Figure 4.28, was obtained using a Butterworth filter of order 2 and $D_0 = 40$ and it results is a brighter image, when compared to the original test image.
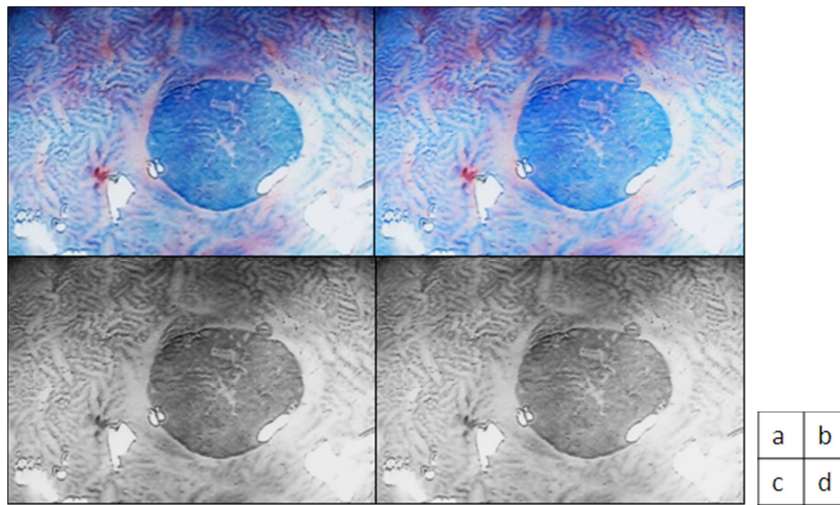
Figure 4.28 – Result of the homomorphic filter implementation: a) original RGB image; b) output image processing in HSI domain; c) original gray image; d) output gray image.

4.2.3. Comparison among enhancement algorithms on endoscopic images

To compare the enhancement quality provided by each enhancement algorithm previously described, it is important to define quantitative measurements beyond the visual perception, which is highly subjective. Hence, different authors have been proposing parameters that can help in measuring the quality of the resultant images (Eskicioglu and Fisher 1995; Sakuldee and Udomhunsakul 2008; Garg, Mittal et al. 2011). Nevertheless, just some of them were used in this project, Table 4.1. In this table, $x(m, n)$ is the input image, $y(n, m)$ the enhanced image, MxN the size of the images, and $mean(x)$ the average intensity value of image $x(m, n)$.

One of the main problems of these measurements is their only suitability to gray images. However, it was clear that the enhancement using the HSI model achieved better results, since it took advantage of color information. Hence, the results obtained from these calculations are extrapolated to the image processing in general.

A lower value for mean square error indicates less error, and, since it is inversely correlated to peak signal to noise ratio (PSNR), as can be seen in Table 4.1, it means higher PSNR (Adler, Gostout et al.). Logically, a higher value of PSNR is good because it signifies that the Signal to Noise Ratio is higher, that is, the signal is bigger than noise, which is the purpose of image enhancement (Sakuldee and Udomhunsakul 2008).

In what concerns to absolute mean brightness error (AMBE), its values should be as small as possible, which indicates that difference between the original and enhanced image brightness should be minimum.

Table 4.1 – Used image quality objective measurements.

Mean Square Error	$MSE = \dfrac{1}{MN} \sum\limits_{m=1}^{M} \sum\limits_{n=1}^{N} (x(m,n) - y(n,m))^2$
Peak Signal to Noise Ratio	$PSNR = 10 log \dfrac{255^2}{MSE}$
Absolute Mean Brightness Error	$AMBE = |mean(x) - mean(y)|$
Contrast	$C = \dfrac{f - b}{f + b}$

Finally, contrast is calculated based on foreground (f) and background (b) intensities of the enhanced image (Rangayyan 2005). It was established that f and b should be calculated in a defined square with size 20x20, so that the foreground and background could be represented by a small sample instead of just one pixel, which would be more sensitive to errors. Hence, the mean intensity values in this square represented f and b. Higher values of C mean that the image has more contrast.

Considering these assumptions, the measurement result is depicted in Figure 4.29, where the values of the objective measurements referred in Table 4.1 were normalized, and the processing time of each algorithm was included, considering that it was processed in a PC with Operative System Windows XP, Intel Pentium Dual Core 2310 processor and 1 GB DDR2 of memory RAM. The algorithms in the frequency domain were not considered, since they were very similar to those presented in the spatial domain and did not show an important contribution to this study.

The lower value of MSE and maximum of PSNR resulted from Adaptive Unsharp Masking implementation while the minimum processing time obtained was 0.08 seconds for Laplacian filter. On the other hand, the worst results were attained for Sobel and Laplacian, which presented the highest MSE and lowest PSNR. In what concerns to AMBE, the smallest value was obtained for Adaptive Unsharp Masking and the highest for Sobel and Laplacian.
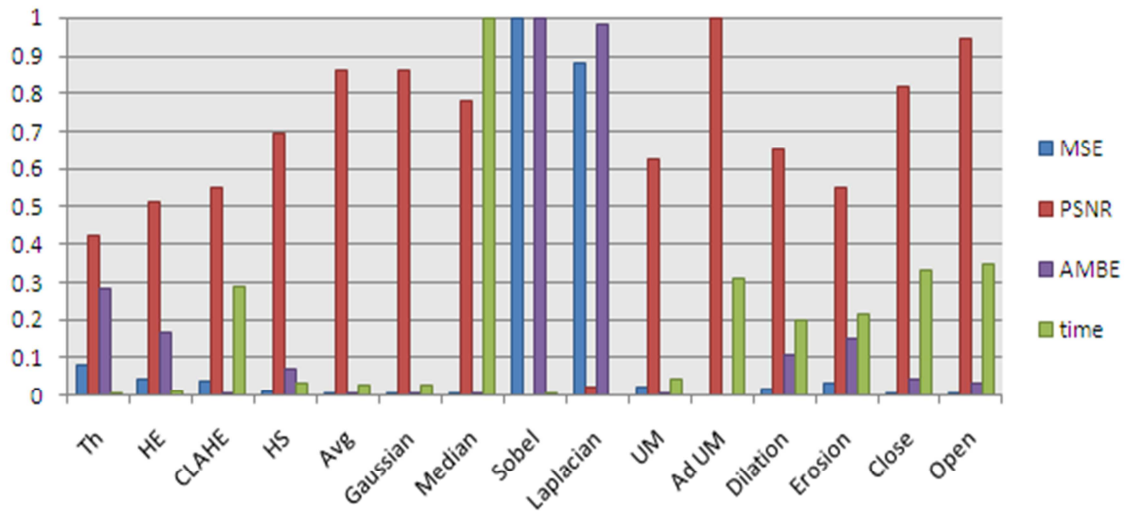
Figure 4.29 – Objective measurements on image enhancement obtained by each algorithm implemented.

Table 4.2 – Legend of Figure 4.29, explaining the parameters chosen for each algorithm.

Legend	Algorithm Name	Parameters
Th	Threshold window	$T_1 = 0.1 - T_2 = 0.7$
HE	Histogram Equalization	--
CLAHE	Contrast-Limited Adaptive Histogram Equalization	No. tiles = [40 40], Clip Limit = 0.01
HS	Histogram Stretching	--
Avg	Average Filter	Mask size = [10 10]
Gaussian	Gaussian Filter	Mask size = [10 10], sigma=20
Median	Median Filter	Mask size = [10 10]
Sobel	Sobel Filter	--
Laplacian	Laplacian Filter	--
UM	Unsharp Masking	Gaussian [10 10], sigma = 20
Ad UM	Adaptive Unsharp Masking	Gaussian [10 10], sigma = 20 Median filter [5 5]
Dilation	Morphological dilation	Shape = disk, size = 5
Erosion	Morphological erosion	Shape = disk, size = 5
Close	Morphological close	Shape = disk, size = 5
Open	Morphological open	Shape = disk, size = 5

From these results, it could be concluded that for the test image used, the best method of image enhancement was the Adaptive Unsharp Masking. However, according to the aim desired in this study, there are other algorithms suitable and good to use in the image preprocessing step, and it should be made an agreement between enhancement and the posterior segmentation process. Having this in mind, the CLAHE algorithm, whose output image has a more homogeneous background, the Histogram Stretching, that clearly enhances contrast, the smoothing algorithms (average, Gaussian and median), that smooths the background variations and eliminates noise, and morphological operations, in particular open/close that can eliminate noise, are important methods that could be used to enhance the object of interest.

Until now, the enhancement methods were applied to one test image. However, to evaluate the performance of the algorithms explored, they were applied to more two endoscopic images, displayed in Figure 4.30. Thus, the best algorithms will be those which demonstrate more coherence on the enhancement result when applied to different images.
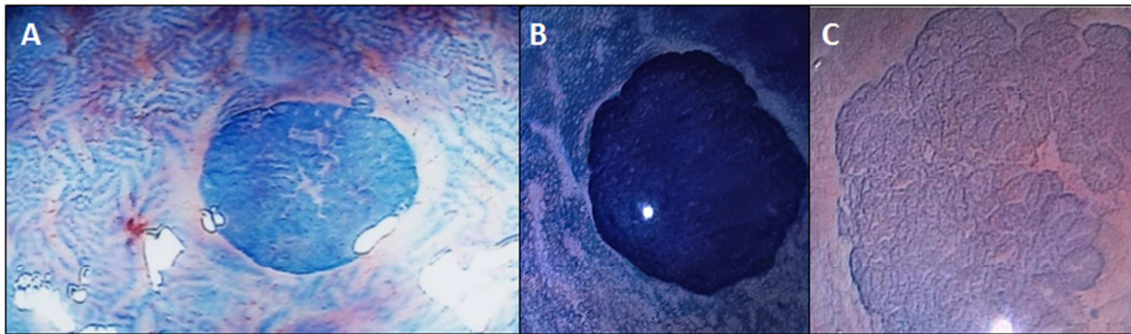
Figure 4.30 – Endoscopic images representing the ACF lesion which are used to apply image processing algorithms.

In Figure 4.31, the best results correspond to the highest values of PSNR, which happened for Adaptive Unsharp Masking (Ad UM) and the smoothing filters, average, median and Gaussian. Although the Ad UM presented more coherence between the three images, it is a sharpening algorithm which will be problematic for the image segmentation algorithms since it enhances high intensity noise. Thus, the smoothing filters revealed as the best option.

Moreover, another important objective of image enhancement is contrast, which results are shown in Figure 4.32. The best contrast achieved was obtained by the Histogram Stretching algorithm, which had higher values in almost every image tested.
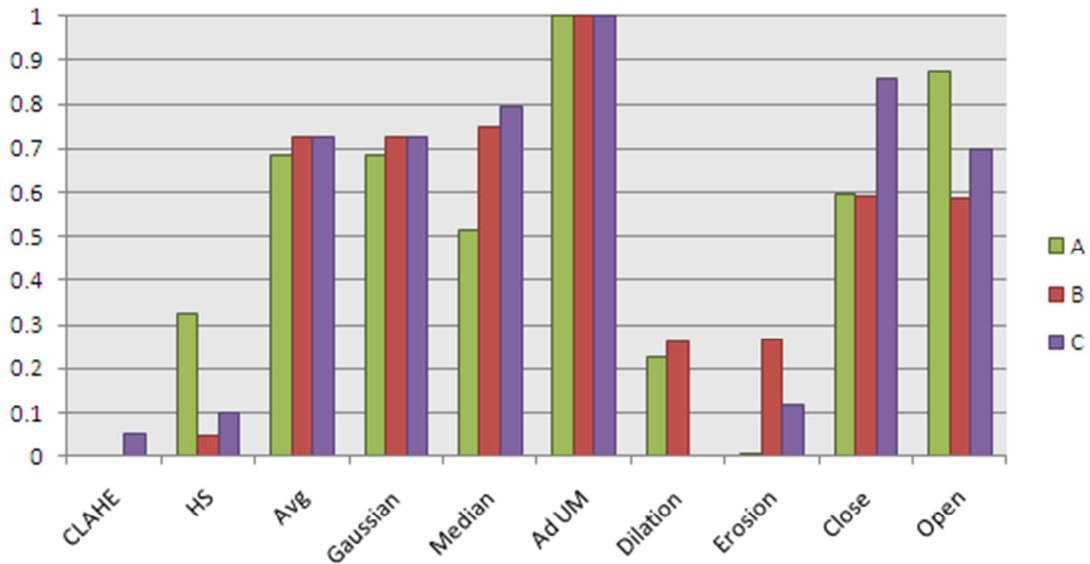
Figure 4.31 – Comparison of the Peak signal to noise ratio of image enhancement algorithms applied on different endoscopic images.
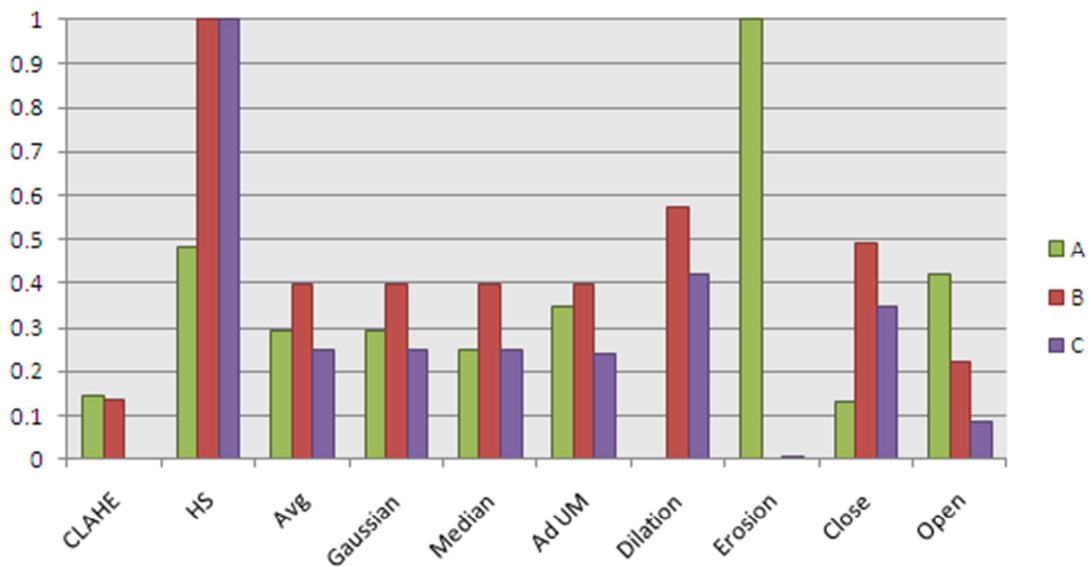
Figure 4.32 – Comparison of contrast values of image enhancement algorithms applied on different endoscopic images.

However, it is always important to evaluate not just the objective measurements but the visual perception of enhanced images. The results of Histogram Stretching can be seen in Figure 4.33, where the contrast enhancement is evident when compared to original images, Figure 4.30.

Considering the results from PSNR measurements and looking for the existence of "salt and pepper" noise in the three endoscopic images, the median filter revealed to be the best option considering the smoothing algorithms studied, as can be seen in Figure 4.34, where it was

applied with a 10x10 window size. However, the resultant contrast was poor. Thus, it was developed a hybrid method, which includes Histogram Stretching and Median filter, taking profit of the advantages of both techniques, Figure 4.37.
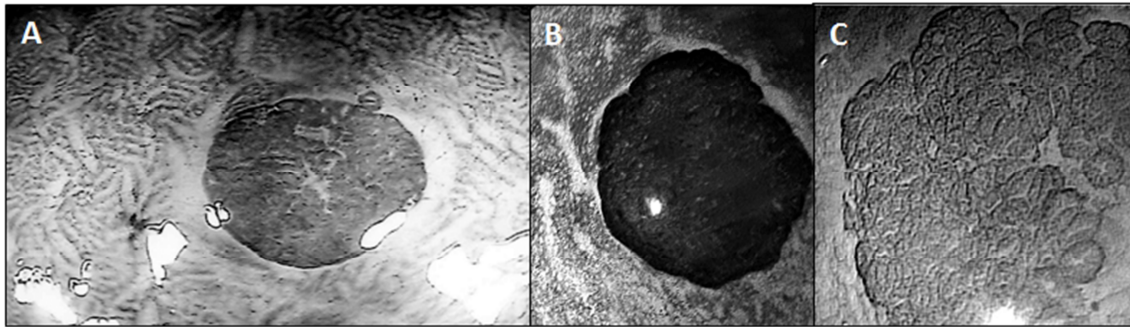
Figure 4.33 – Results of the Histogram Stretching algorithm applied to the test endoscopic images.
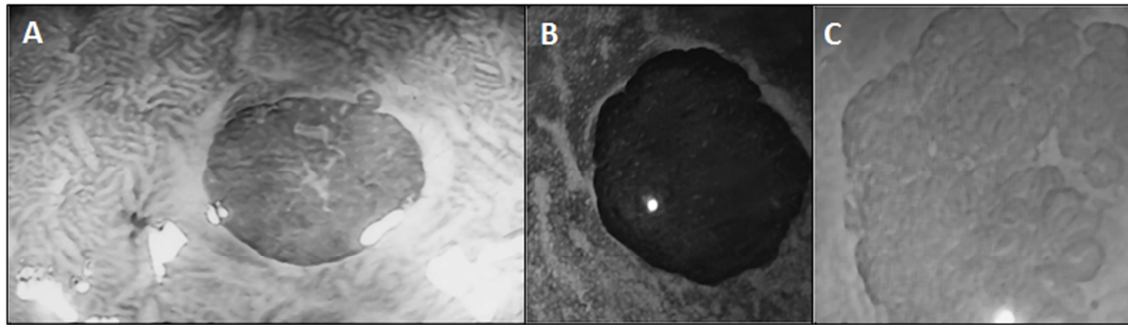
Figure 4.34 – Results of the median filter on the test endoscopic images.

The application of the hybrid method to the endoscopic images in the gray scale and HSI model is shown in Figures 4.35 and 4.36, respectively. When the enhanced images are compared to the original, Figure 4.30, the ACF lesion is more evident due to better contrast, and because the background is smoother.

In the next section, these images will be used as inputs to the image segmentation algorithms with the purpose of detecting the ACF structures.
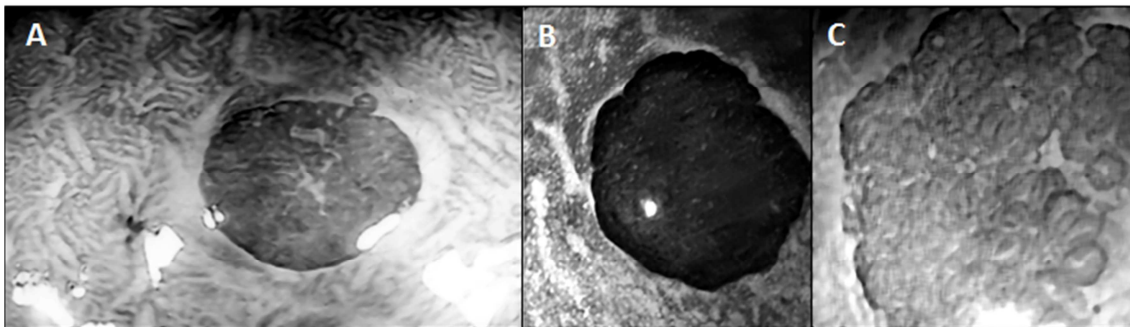
Figure 4.35 – Results of the hybrid method on the test endoscopic images.
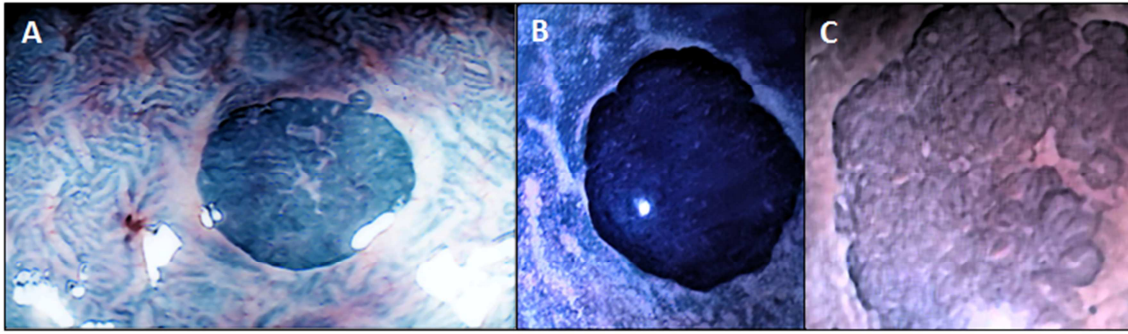
Figure 4.36 – Result of the hybrid method, using HSI model, on test endoscopic images.
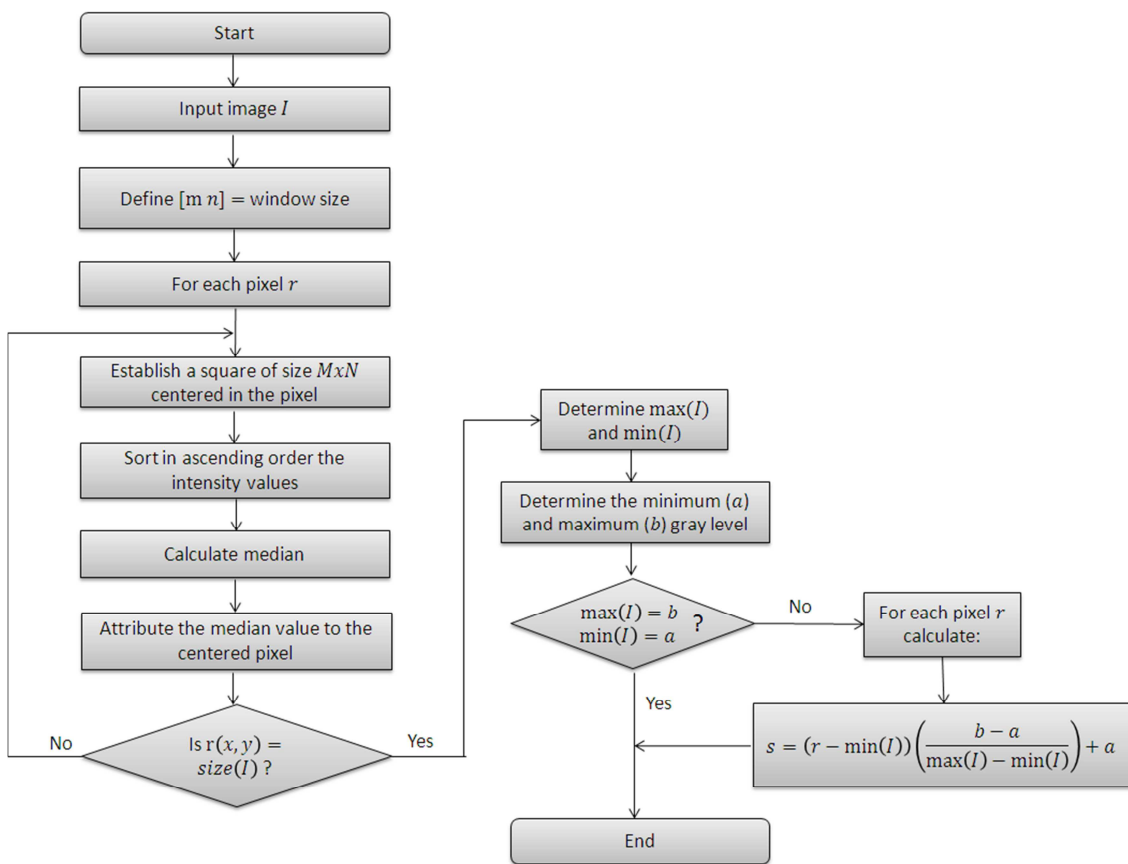
Figure 4.37 – Block diagram of the hybrid method developed: Median filter and Histogram Stretching.

4.3. Image Segmentation

When the preprocessing step is completed, the images are prepared for the next step in which the objects of interest are detected and segmented. In this project, the purpose was to detect ACF lesions and determine their boundaries, separating them from the image background. As mentioned in Chapter 3, there are a large number of algorithms available to perform this segmentation, based on boundaries, regions or thresholding. Hence, some of those methods were chosen and applied on the enhanced test endoscopic images, Figure 4.36, and their results are presented and discussed in this section.

4.3.1. Thresholding

The threshold algorithm divides the image into two or more groups, according to their intensity levels. Their basic and global operation was mentioned in sections 3.4.1. and 4.2.1.4 in a perspective of image enhancement. It was concluded that global thresholding applied on the test endoscopic images did not segment well the ACF lesions. Hence, it is here detailed a locally approach proposed by Wellner (1993), called quick adaptive thresholding.

This algorithm runs through the image and calculates a moving average of the last s pixels seen. When the value of a pixel is significantly lower than this average, it is set to black, otherwise it is left white. Let p_n represent the value of a pixel at point n and $f_s(n)$ be the sum of the values of the last s pixels at point n:

$$f_s(n) = \sum_{i=0}^{s-1} p_{n-i}.$$

(4.29)

The value of the resulting image $T(n)$ is either black or white (0 or 1) depending on whether it is t percent darker than the average value of the previous s pixels:

$$T(n) = \begin{cases} 1 & if \ p_n < \left(\frac{f_s(n)}{s}\right)\left(\frac{100-t}{100}\right) \\ 0 & otherwise \end{cases},$$

(4.30)

The values of t should be defined, and another approach is to calculate the median instead of average of the s previous pixels.

The Matlab® implementation, based on the Wellner's algorithm, was developed by Peter Kovesi (2008). This algorithm has three important inputs: Filter size, used to determine the local weighted mean or local median, t percentage and filter type, which could be Gaussian or median.

66

The default values to these three parameters were:

- filter size of one twentieth of the maximum image dimension;
- *t* percentage of 15;
- Gaussian filter type.

They were used to perform adaptive thresholding in an enhanced test endoscopic image and the results are shown in Figure 4.38.
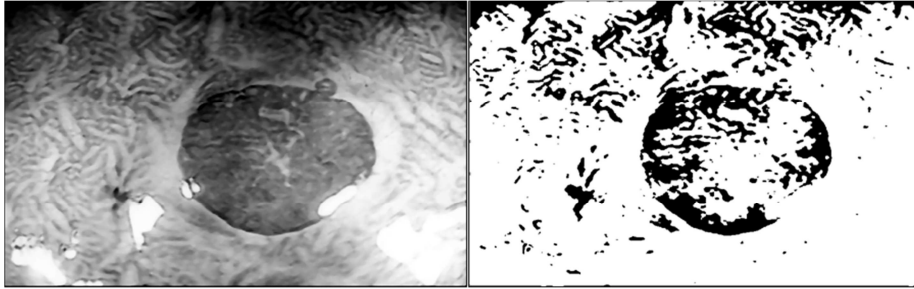
Figure 4.38 – Result of adaptive thresholding using default values: Input enhanced image (left) and output image(right).

The used adaptive thresholding segmentation algorithm divided the image into two regions according to its intensity levels. Since the input image, resulting from the image enhancement mentioned in section 4.2.3, did not present different gray levels in the background and foreground, the result was not satisfactory.

To understand the effect of the three parameters mentioned previously, they were varied and the results are here presented, using the enhanced image as input.
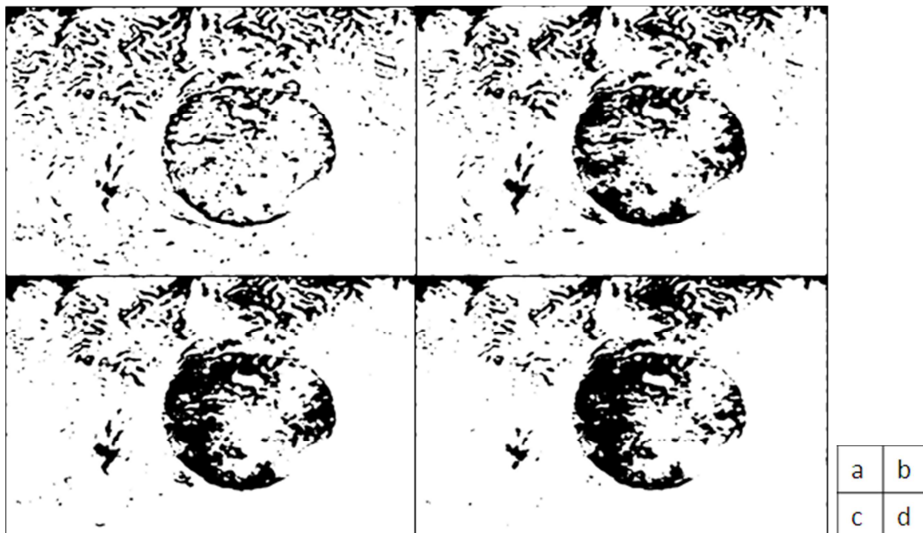
Figure 4.39 – Results of Adaptive thresholding with different filter size: a) 20, b) 58, c) 100, d) 150.

Initially, it was chosen lower and higher values of filter size, varying from 20 to 150; the results are represented in Figure 4.39. As the filter size increased, the object became more evident than the background, but it was not fully separated. In what concerns to t percentage, the higher values led to less detection, that is, the threshold was more restricted, as can be seen in Figure 4.40.
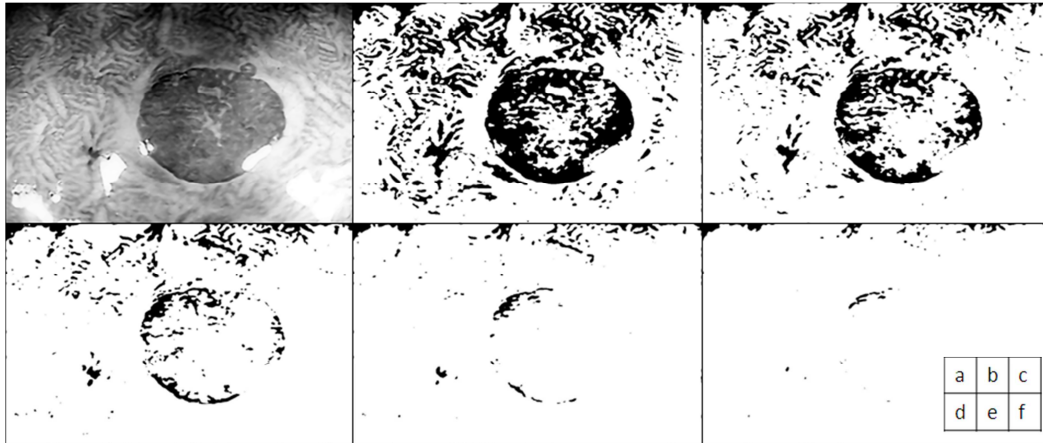
Figure 4.40 – Results of adaptive thresholding with variable t percentages: a) input image, b) $t = 5$, c) $t = 15$, d) $t = 30$, e) $t = 50$, f) $t = 75$.

Finally, when the algorithm focuses on the local pixels, there are two types of analysis: average intensity or median. As such, the thresholding process can be based on the mean intensity occurring locally or, instead, it can use the median value. The results of both filter types are presented in Figure 4.41. The median filter type produced an output image with more evidence to background variations, that is, a noisy image.

Figure 4.41 – Results of adaptive thresholding with Gaussian (b) and median (c) filters.

Concluding, the proposed aim was not accomplished with any parameter changes since the ACF lesion was not separated from the image background. Moreover, the adaptive threshold, as global threshold, was not the best option concerning ACF detection since the images present a variable background and are characterized by similar intensity levels between background and foreground.

4.3.2. Boundary-based

This section introduces algorithms that based their performance in finding boundaries through edge detectors or using deformable models that use curve evolution to determine the limits of objects of interest, i.e., ACF lesions.

4.3.2.1. Edge-based

There are several possible approaches in edge-based algorithms, as Sobel, Laplacian, Roberts, Prewitt and Canny. However, the performance of Canny's (1986) edge detector is in general superior when applied to image segmentation, and, as such, it is the only filter studied in this section. Nevertheless, the Sobel operator is suitable to preprocessing stages, as is discussed later.

Canny's method is based on four fundamental steps. At first, to avoid the influence of noise in edges detection, a Gaussian filter is applied, smoothing the image. This method, as Sobel, is based on gradient calculation. Hence, the second step is characterized by the calculation of the gradient magnitude and direction (angle), according to the equations 4.31 and 4.32, where $g_x = \partial f_s / \partial x$ and $g_y = \partial f_s / \partial y$ are the first order derivative functions in the horizontal and vertically directions of the smoothed image $f_s(x, y)$, respectively.

$$M(x, y) = \sqrt{g_x^2 + g_y^2}, \tag{4.31}$$

$$\propto (x, y) = tan^{-1} \left[\frac{g_y}{g_x} \right] \tag{4.32}$$

Being the edges detected by the gradient function, it typically contains wide ridges around local maxima. Thus, the next step is to thin those ridges by computing nonmaxima suppression. Considering a 3x3 region, it could be defined four orientations for an edge passing in the central pixel of the region: horizontal, vertical, +45° and -45° and the edge direction is determined through the function $\propto (x, y)$. Thus, establishing that d_1, d_2, d_3 and d_4 correspond to the four basic directions: horizontal, -45°, vertical and +45°, respectively, the nonmaxima suppression scheme for a 3x3 region centered at every point (x, y) in $\propto (x, y)$ is given by the following stages:

1. Find the direction d_k that is closest to $\propto (x, y)$;

2. If the value of $M(x, y)$ is lower than at least one of its two neighbors along d_k, let $g_N(x, y) = 0$ (suppression); otherwise, let $g_N(x, y) = M(x, y)$, where $g_N(x, y)$ is the nonmaxima suppressed image.

Finally, it is performed a threshold to reduce false edge points. Using a simple threshold, if it is set too low, there will still be some false edges, and if it is set too high, actual valid edges will be eliminated. Thus, Canny's algorithm attempts to improve on this situation by using hysteresis thresholding which uses two thresholds: a low (T_L) and a high (T_H). Hence, it creates two images, based on:

$$g_{NH}(x, y) = g_N(x, y) \geq T_H, \tag{4.33}$$

$$g_{NL}(x, y) = g_N(x, y) \geq T_L. \tag{4.34}$$

After thresholding, all the nonzero pixels are eliminated from $g_{NL}(x, y)$ by letting:

$$g_{NL}(x, y) = g_{NL}(x, y) - g_{NH}(x, y). \tag{4.35}$$

Finally, all strong pixels in $g_{NH}(x, y)$ are assumed to be valid edge pixels. However, if the threshold T_H was set too high, the edge defined by the valid strong pixels could have gaps. As such, the values in $g_{NL}(x, y)$ are useful to fill those gaps, according to the following procedure:

1. Locate the next unvisited pixel, p, in $g_{NH}(x, y)$;

2. Mark as valid edge pixels all the weak pixels in $g_{NL}(x, y)$ that are connected to p using 8-connectivity, i.e., that are in one position in the 8 pixels surrounding p;

3. If all nonzero pixels in $g_{NH}(x, y)$ have been visited, set to zero all pixels in $g_{NL}(x, y)$ that were not marked as valid edge pixels; Otherwise, return to step 1.

The final image is obtained by adding all nonzero pixels of $g_{NL}(x, y)$ to $g_{NH}(x, y)$.

The Matlab® image processing toolbox comprises the Canny's algorithm implementation, and it was used to evaluate the effect of this technique when applied on the test endoscopic image. Since it uses the Gaussian filter to smooth and then uses two thresholds, the Canny's implementation is dependent on threshold and sigma value chosen.

In Figure 4.42, the detection was performed directly in the enhanced image (resulting from section 4.2.3) using default values of threshold and sigma, that is a maximum threshold corresponding to the maximum magnitude gradient value, a minimum threshold equal to 40%

of the maximum threshold and a sigma value of $\sqrt{2}$. The edge detection was followed by a dilation morphologic operation to better visualize the result.
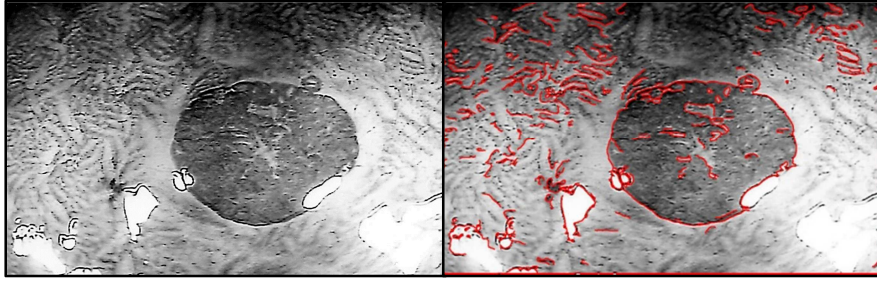
Figure 4.42 – Canny edge detector applied on an enhanced test image.

Although the ACF lesion was detected there are also few particles evidenced from the image background.

In order to understand the effect produced by threshold and sigma parameters, different values were considered. Initially, setting the sigma value as $\sqrt{2}$, it was used a threshold of 0.1, 0.2, 0.3 and 0.4. As the threshold value increased, less edge detection was produced, as shown in Figure 4.43.
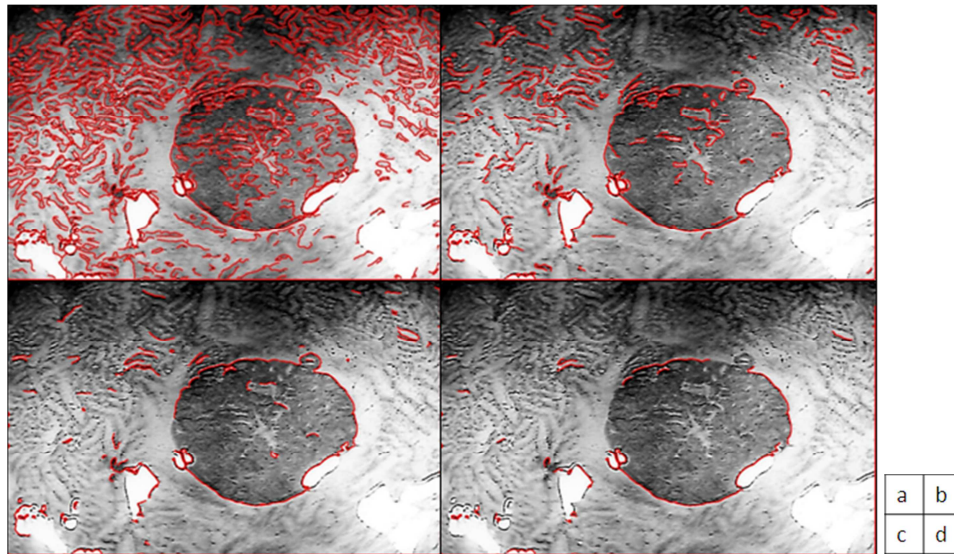
Figure 4.43 – Results of the Canny's edge detector with different values of threshold:
a) 0.1, b) 0.2, c) 0.3, d) 0.4.

Considering a threshold value of 0.2, the sigma coefficients were varied from 0.5 to 2. The effect of this parameter is shown in Figure 4.44, where the increase of sigma values led to more background detection, what is undesired.
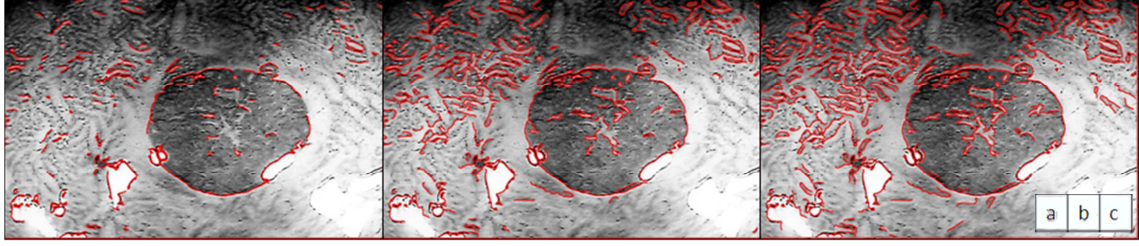
Figure 4.44 – Results of the Canny's edge detection with different values of Gaussian sigma: a) 0.5, b) $\sqrt{2}$, c) 2.

Concluding, there should be established a compromise between the two parameters cited in order to segment successfully the region of interest, i.e. the ACF lesion.

4.3.2.2. Deformable models-based

The deformable models are recognized by their ability to segment, match and track objects in images by exploiting constraints derived from the image data together with a priori knowledge about the objects' location, size and shape. Furthermore, they are capable of detecting biological structure differences over time and from different individuals due to their capability of overcoming significant variability (McInerney and Terzopoulos 1996). There are two fundamental methods included in this section that are here described: original active contour algorithm, usually known as Snake algorithm, and Active Contours without Edges (ACWE) technique.

a) *Active Contour Snake*

The snake algorithm was first developed by Kass et al (1988) and is based on image forces and external constraint forces. The image forces push the snake toward salient image features like lines, edges, and subjective contours. The external constraint forces are responsible for positioning the snake near the desired local minimum. Hence, representing the parametric position of a snake by $v(s) = (x(s), y(s))$, its energy function is given as:

$$E_{snake}^* = \int_0^1 E_{snake}(v(s))ds = \int_0^1 E_{ext}(v(s)) + E_{int}(v(s)) + E_{image}(v(s))ds. \quad (4.36)$$

where E_{int} represents the internal energy, E_{ext} the external energy of the contour due to bending or discontinuities, and E_{image} is the external image forces. The evolution from an initial contour to the contour of the object is expressed by an energy minimization process.

The internal energy can be written as:

$$E_{int} = \propto (s) \left| \frac{dv(s)}{ds} \right|^2 + \beta(s) \left| \frac{d^2 v(s)}{ds^2} \right|^2 . \tag{4.37}$$

It is composed of a first-order term controlled by $\propto (s)$ and a second-order term controlled by $\beta(s)$. The values used in these two parameters will define the extent to which the contour is allowed to stretch or bend at that point, since the relative sizes of $\propto$ and β control the influence of the corresponding constraints.

The first term of the equation 4.37 represents the elastic energy (continuity), where a high value implies a high rate of change of the contour. The second term represents the curvature energy and measures the energy due to bending. For instance, the choice of $\propto (s)$ and $\beta(s)$ values controls the shape of the snake. Low values of $\propto (s)$ results in considerable changes of points in space, while higher values imply that the snake aims to attain evenly spaced contour points (Williams and Shah 1992). In what concerns to $\beta(s)$ parameter, low values imply that curvature is not minimized, and the contour can form corners, whereas higher values predispose the snake to smooth contours.

The external energy can be repulsive or attractive, Figure 4.45, in order to repel or attract the active contour to the image. Hence, the formulation of attractive external image is given by:

$$E_{ext}(x) = k|i - x|^2 . \tag{4.38}$$

This energy is minimal when $x = i$, and it assumes the value of k when $i - x = \pm 1$. The repulsive external energy is formulated as:

$$E_{ext}(x) = \frac{k}{|i-x|^2} . \tag{4.39}$$

The repulsive energy is maximal when $x = i$ and it is unity when $i - x = \pm k$. However, since this is a division operation, the repulsion term must be clipped as the denominator approaches zero.

(a) Attractive Energy   **(b) Repulsive Energy**
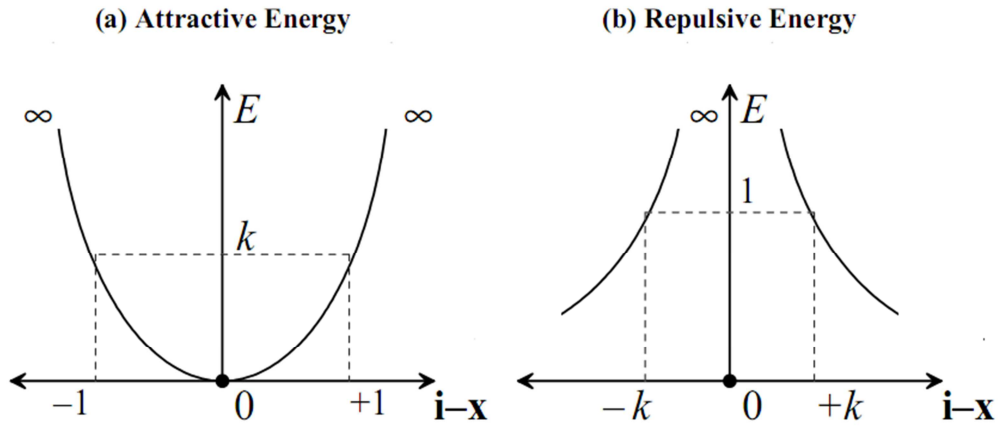
Figure 4.45 – Attraction and repulsion energy (from (Ivins and Porrill 2000)).

The image energy E_{image}, generated by processing an image $I(x, y)$ produces a force that can be used to drive snakes towards features of interest. It consists of three different energy functionals that attract snakes to lines, edges, and terminations. The total energy can be expressed as a weighted combination of the three energy functionals:

$$E_{image} = w_{line}E_{line} + w_{edge}E_{edge} + w_{term}E_{term}.$$

(4.40)

The simplest functional correspond to E_{line}, which is the image intensity itself. Thus, depending on the w_{line} value, the snake will be attracted either to light lines or dark lines.

The edge energy functional represents the image edges and is defined as:

$$E_{edge} = -|\nabla I(x, y)|^2,$$

(4.41)

where $I(x, y)$ represents the input image. Thus, the snake will be attracted to contours with large image gradients.

Finally, in order to find terminations of line segments and corners, the E_{term} is used and defines the curvature of the contour. Hence, to express this energy functional it is considered $C(x, y) = G_\sigma(x, y) * I(x, y)$ as a slightly smoothed version of the image. Then, it is considered that $\theta = tan^{-1}(C_y/C_x)$ is the gradient angle and $n = (cos\theta, sin\theta)$ and $n_\perp = (-sin\theta, cos\theta)$ are unit vectors along and perpendicular to the gradient direction.

The curvature of the level contour in $C(x, y)$ can be written as:

$$E_{term} = \frac{\partial \theta}{\partial n_\perp} = \frac{C_{yy}C_x^2 - 2C_{xy}C_xC_y + C_{xx}C_y^2}{(C_x^2 + C_y^2)^{3/2}}.$$

(4.42)

The weight values attributed to each energy functional determine the contour moving and detection (Kass, Witkin et al. 1988). Moreover, E_{image}, is multiplied by the parameter $\gamma(s)$ that influences the effect of this energy in the overall snakes contour.

The Kass et al.(1988) algorithm implementation in Matlab® was developed by Ritwik Kumar (2010), from Harvard University. The method works only when the initial contour is defined outside the object. The coefficients $\propto$, β, γ, k, W_{line}, W_{edge}, W_{term} and number of iterations can be defined in order to obtain the final contour in the objects' boundaries. The values chosen for each parameter is crucial for the convergence of the initial contour with the ACF edge. As such, different values were tested, Table 4.3, and the results obtained are shown in Figure 4.46.

Initially, all coefficient values were defined equal and low and the result exhibited a final contour not well adjusted to the ACF boundary. Considering that the edge is a fundamental characteristic in this segmentation process, the weight of edge energy was set higher and the results demonstrated an improvement since the final contour was outside the ACF structure.

Table 4.3 – Coefficient values used in the Snake algorithm.

Parameters	a)	b)	c)	d)	e)	f)
α	0.1	0.1	0.6	0.6	0.6	0.6
β	0.1	0.1	0.1	0.1	0.1	0.1
γ	0.1	0.1	0.1	1	1	1
k	0.15	0.15	0.15	0.15	0.15	0.15
W_{line}	0.1	0.1	0.1	0.1	0.1	0.1
W_{edge}	0.1	1	1	1	1.5	1.5
W_{term}	0.1	0.1	0.1	0.1	0.1	0.1
No. iterations	300	300	300	300	300	500

Afterwards, since the contour was highly rigid, the α was increased, but as it became the predominant energy between the three, equation 4.36, it did not stop at the ACF boundary. To overcome this problem, the γ value was set higher, so that the E_{image} could have more weight in the overall snake energy. As such, it was obtained a final contour almost totally fit to the ACF boundary. Finally, one last adjustment was made in the E_{edge} and iterations number, being obtained a good relation between the snake detection and the real ACF boundary.
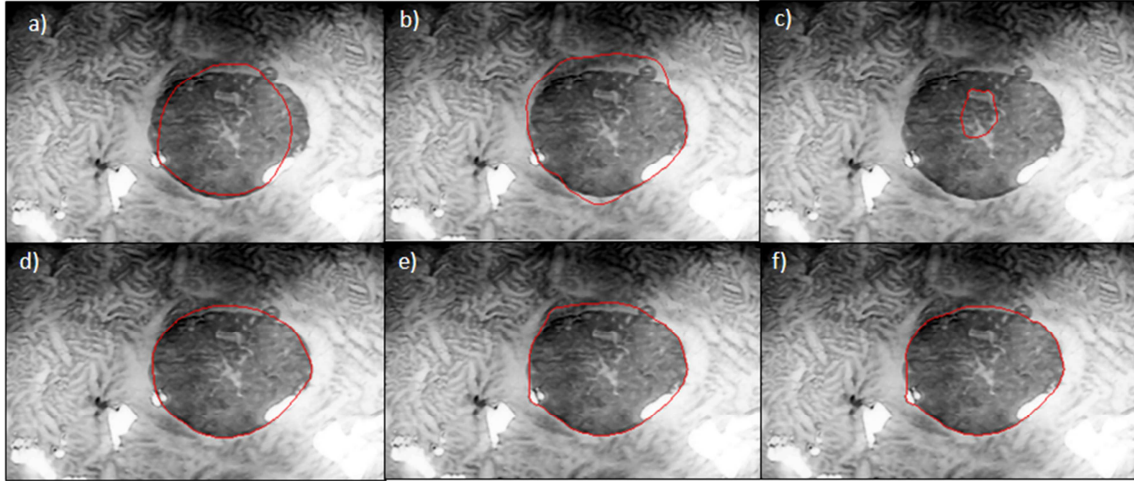
Figure 4.46 – Results of the Snake algorithm using the coefficients indicated in Table 4.3.

b)   *Active Contour without Edges*

The active contours without edges (ACWE) follows the same principle as snakes, that is, it starts with a curve around the object to be detected, and then the curve moves toward its interior normal until it reaches the object boundary and stops. In common deformable models, it is used an edge detector, as the gradient, to indicate where to stop the evolving curve. However, Chan and Vese (1999) (CV) proposed a different ACWE model without a stopping edge-function, i.e., a model which is not based on the gradient of the image for the stopping process. Thus, it is based on an energy minimization problem, which can be reformulated in the level set formulation, leading to an easier way to solve the problem. This is the main advantage of this method which is here detailed (Wang, Huang et al. 2010).

Considering the evolving curve C in Ω, as the boundary of an open subset ω of Ω, the inside of C denotes the region ω, and the outside denotes the region $\Omega \backslash \varpi$. The aim of this method is the minimization of the image energy. To understand better the model principles, it will first be explained the basic idea in a simple case (Chan and Vese 2001).

Assume that the image u_0 is formed by two regions of approximately piecewise-constant intensities, of distinct values u_0^i and u_0^o. Assume further that the object to be detected is represented by the region with the value u_0^i and the boundary C_0 . Then one have $u_0 \approx u_0^i$ inside the object [or inside (C_0)], and $u_0 \approx u_0^o$ outside the object [or outside (C_0)].

Afterwards, the "fitting" term is given as:

$$F_1(C) + F_2(C) = \int_{inside(C)} |u_0(x,y) - c_1|^2 dxdy + \int_{outside(C)} |u_0(x,y) - c_2|^2 dxdy, \quad (4.43)$$

where C is any other variable curve, and the constants c_1, c_2, depending on C, are the averages of u_0 inside and outside C, respectively. In this simple case, it is obvious that C_0, the boundary of the object, is the minimizer of the fitting term:

$$\inf\{F_1(C) + F_2(C)\} \approx 0 \approx F_1(C_0) + F_2(C_0). \quad (4.44)$$

The variation of the parameters is depicted in Figure 4.47, where the minimization of $F_1(C) + F_2(C)$ corresponds to the object boundary detect, that is, $C = C_0$.

To enhance the correct curve evolution, Chan and Vese method introduces the level set method that allows the detection of cusps, corners and automatic topological changes.
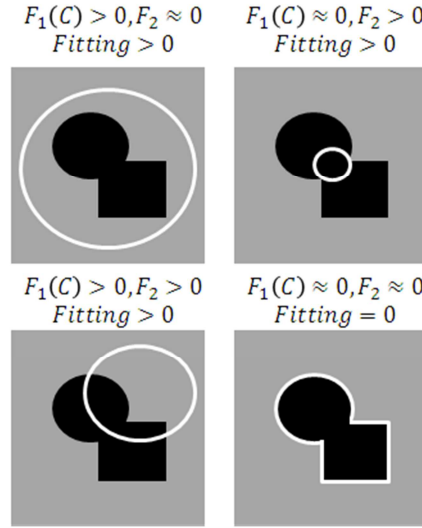
Figure 4.47 – The minimization process of the fitting term (from (Chan and Vese 2001)).

The CV model implementation is based on minimizing the above fitting term with some regularizing terms added. Therefore, it is introduced an energy functional $F(c_1, c_2, C)$ defined as:

$$F(c_1, c_2, C) = \mu \cdot Lenght(C) + v \cdot Area(inside(C)) +$$
$$\lambda_1 \int_{inside(C)} |u_0(x,y) - c_1|^2 dxdy + \lambda_2 \int_{outside(C)} |u_0(x,y) - c_2|^2 dxdy, \quad (4.45)$$

where $\mu \geq 0, v \geq 0, \lambda_1, \lambda_2 > 0$ are fixed parameters. Usually, the values used in these terms are: $\lambda_1 = \lambda_2 = 1$ and $v = 0$.

The new objective is to find the c_1, c_2, C values that will be the solution to the minimization problem:

$$inf_{c_1,c_2,C} F(c_1, c_2, C). \tag{4.46}$$

The level set formulation redefines the problem and considers $C \subset \Omega$ as the zero level set of some Lipschitz function $\phi: \Omega \to \mathbb{R}$, such that:

$$\begin{cases} C = \partial\omega = \{(x,y) \in \Omega: \phi(x,y) = 0\}, \\ inside(C) = \omega = \{(x,y) \in \Omega: \phi(x,y) > 0\}, \\ outside(C) = \Omega\backslash\varpi = \{(x,y) \in \Omega: \phi(x,y) < 0\}. \end{cases} \tag{4.47}$$

In Figure 4.48, it is illustrated the above assumptions and notations on the level set function ϕ, defining the evolving curve C.
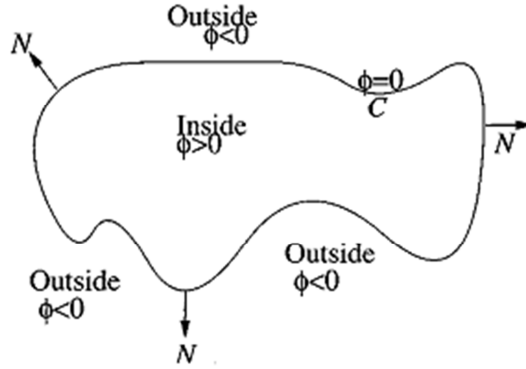
Figure 4.48 – Curve $\boldsymbol{C} = \{(\boldsymbol{x}, \boldsymbol{y}): \boldsymbol{\phi}(\boldsymbol{x}, \boldsymbol{y}) =\}$ propagating in normal direction (from (Chan and Vese 2001)).

Therefore, the unknown variable C is replaced by the unknown variable ϕ and the new energy, still denoted by $F(\phi, c_1, c_2)$, becomes:

$$F(\phi, c_1, c_2) = \mu \cdot length\{\phi = 0\} + v \cdot area\{\phi \geq 0\} + \lambda_1 \int_{\phi \geq 0} |u_0 - c_1|^2 dxdy + \lambda_2 \int_{\phi < 0} |u_0 - c_2|^2 dxdy. \tag{4.48}$$

Using the Heaviside function H defined by:

$$H(x) = \begin{cases} 1, & if \ x \geq 0 \\ 0, & if \ x < 0' \end{cases} \tag{4.49}$$

and the one-dimensional Dirac measure δ concentrated at 0 (zero) and defined (in the sense of distributions) by:

$$\delta(x) = \frac{d}{dx}H(x), \tag{4.50}$$

the terms in the energy F is expressed as:

$$\begin{cases} length\{\phi = 0\} = \int_\Omega |\nabla H(\phi)| = \int_\Omega \delta(\phi)|\nabla\phi|, \\ area\{\phi \geq 0\} = \int_\Omega H(\phi)dxdy, \end{cases} \tag{4.51}$$

and

$$\begin{cases} \int_{\phi \geq 0}|u_0 - c_1|^2 dxdy = \int_\Omega |u_0 - c_1|^2 H(\phi)dxdy \\ \int_{\phi < 0}|u_0 - c_2|^2 dxdy = \int_\Omega |u_0 - c_2|^2 (1 - H(\phi))dxdy \end{cases} \tag{4.52}$$

Then the energy $F(\phi, c_1, c_2)$ can be written as:

$$F(\phi, c_1, c_2) = \mu \cdot \int_\Omega \delta(\phi)|\nabla\phi| + v \cdot \int_\Omega H(\phi)dxdy +$$

$$\lambda_1 \int_\Omega |u_0 - c_1|^2 H(\phi)dxdy + \lambda_2 \int_\Omega |u_0 - c_2|^2 (1 - H(\phi))dxdy. \tag{4.53}$$

Keeping ϕ fixed and minimizing the energy $F(\phi, c_1, c_2)$ with respect to the constants c_1 and c_2, it is easy to express these constants function of ϕ by:

$$c_1(\phi) = \frac{\int_\Omega u_0 H(\phi)dxdy}{\int_\Omega H(\phi(x,y))dxdy} \quad \text{(the average of the image } u_0 \text{ in } \{\phi \geq 0\}), \tag{4.54}$$

$$c_2(\phi) = \frac{\int_\Omega u_0 (1-H(\phi))dxdy}{\int_\Omega (1-H(\phi(x,y)))dxdy} \quad \text{(the average of the image } u_0 \text{ in } \{\phi < 0\}). \tag{4.55}$$

The evolution of the curve is influenced by two terms: the "region term" $\lambda_1 (u_0 - c_1)^2 + \lambda_2 (u_0 - c_2)^2$ which affects the motion of the curve and the term $\mu \cdot \int_\Omega \delta(\phi)|\nabla\phi|$ which is the penalty on the total length of the curve C. For example, if the boundaries of the image are

smoothed, it should be chosen a larger value of μ, to prevent C from being a complex curve. The value of v is usually set to zero.

λ_1 and λ_2 affect the desired uniformity inside and outside C, respectively. Hence, it would be advisable to set $\lambda_1 < \lambda_2$ when it is expected a uniform background and varying grayscale in the foreground of the image.

Since the aim is to minimize the energy $F(\phi, c_1, c_2)$, it is used Euler-Lagrange equations and the gradient-descent method, where $\phi(x,y)$ satisfies them Partial Differential Equation (PDE) for the artificial time t:

$$\begin{cases} \frac{\partial \phi}{\partial t} = \delta(\phi) \left[\mu div \left(\frac{\nabla \phi}{|\nabla \phi|} \right) - v - \lambda_1 (u_0 - c_1)^2 + \lambda_2 (u_0 - c_2)^2 \right] in \ \Omega \\ \qquad\qquad \frac{\delta(\phi)}{|\nabla \phi|} \frac{\partial \phi}{\partial n} = 0 \ \ on \ \partial \Omega \end{cases} . \qquad (4.56)$$

In practice, it is necessary to consider regularized versions of the functions H and δ, denoted here by H_ε and δ_ε, such that $\delta_\varepsilon(x) = H'_\varepsilon(x)$. Thus, the analytical approximation using Heaviside and dirac delta functions is given by:

$$H_{1,\varepsilon}(x) = \begin{cases} 1, if \ x > \varepsilon \\ 0, if \ z < -\varepsilon \\ \frac{1}{2}\left[1 + \frac{x}{\varepsilon} + \frac{1}{\pi} sin\left(\frac{\pi x}{\varepsilon} \right) \right] \ if \ |x| \le \varepsilon \end{cases}, \qquad (4.57)$$

$$\delta_{1,\varepsilon}(x) = H'_{1,\varepsilon}(x) = \begin{cases} 0, if \ |x| > \varepsilon \\ \frac{1}{2\varepsilon}\left[1 + cos\left(\frac{\pi x}{\varepsilon} \right) \right], if \ |x| \le \varepsilon \end{cases}. \qquad (4.58)$$

However, the Chan and Vese proposal introduces the Heaviside approximation described as:

$$H_{2,\varepsilon}(x) = \frac{1}{2}\left(1 + \frac{2}{\pi} arctan\left(\frac{x}{\varepsilon} \right) \right). \qquad (4.59)$$

As $\varepsilon \to 0$, both approximations converge to H and δ_0. However, with the second approximation the algorithm has the tendency to compute a global minimizer, which could be due to the fact the Euler-Lagrange equation for ϕ acts only locally, on a few level curves around $\{\phi(x,y) = 0\}$ using $H_{1,\varepsilon}(x)$ and $\delta_{1,\varepsilon}(x)$, while in $H_{2,\varepsilon}(x)$ and $\delta_{2,\varepsilon}(x)$ the equation acts on all level curves. To further explanation of the algorithm and its fundamental steps it is recommended to see (Chan and Vese 2001).

The algorithm used in this project was developed by Yue Wu (2009) and was applied in the test endoscopic image in order to segment the ACF lesions.

The three variable parameters are μ, number of iterations and mask type, which could be a small, medium or large circle or approximated 160 circles all over the image, as can be seen in Figure 4.49. Thus, the influence of these coefficients was studied and the results are presented in Figure 4.50.
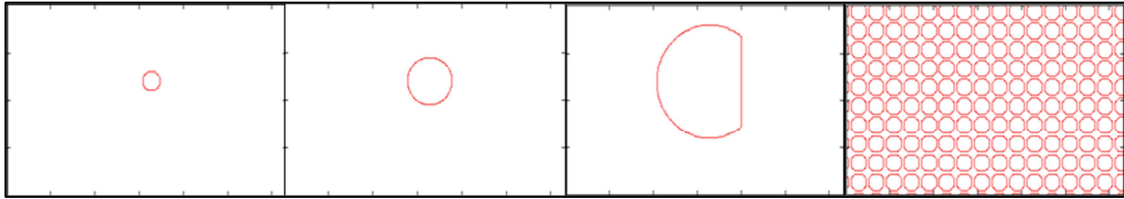
Figure 4.49 – Chan and Vese algorithm mask types; From left to right: Small, Medium, Large, Whole.

The results represent the global-region based segmentation obtained at the end of the contour moving. There were no significant differences between the mask types chosen, but when the whole type was used (Figure 4.51), the ACF became more evident.

Figure 4.50 – Results of the Chan and Vese method using different mask types: small (left), medium (middle), large (right).

Finally, considering that the parameter μ influences the weight of contour length in the energy function, it was used μ values varying from 0.01 to 0.5. In Figure 4.51, it is visible that the increasing of μ led to smoothed segmentation and less evidence of the ACF lesion.

Concluding, this method did not present satisfactory segmentation results, since it was not able to segment successfully the region of interest in the test image used.
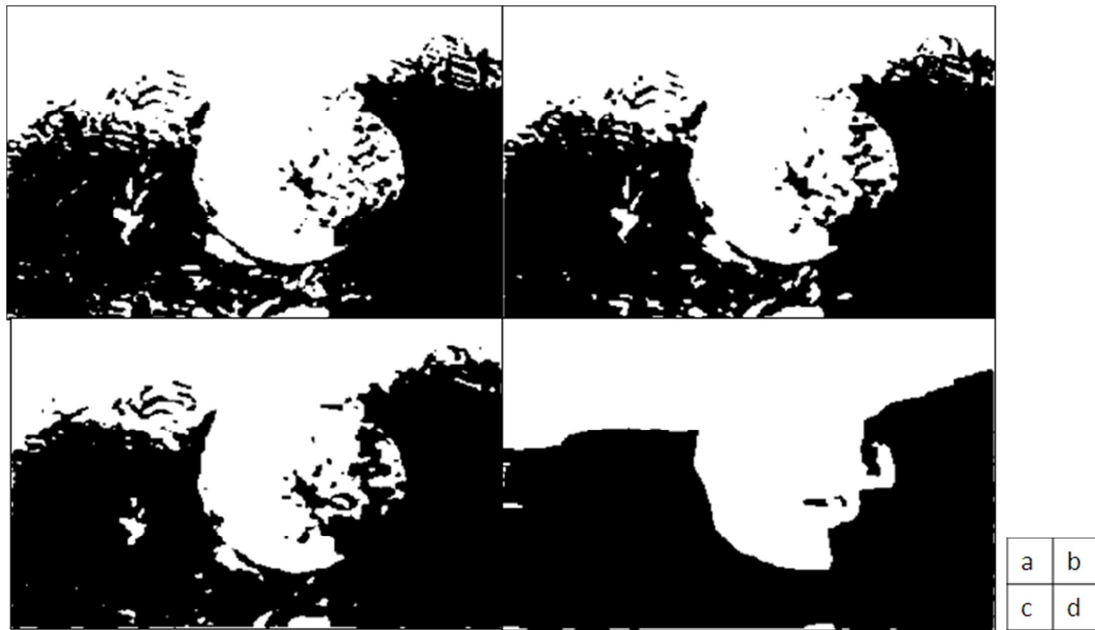
Figure 4.51 – Results of the Chan and Vese method using different μ values:
a) 0.01, b) 0.2, c) 0.3, d) 0.5.

4.3.3. Region-based

In this section, the algorithms based their approach on finding boundaries between image regions according to the discontinuities in pixels' intensity. These methods rely on the postulate that neighboring pixels within a region have similar values. Hence, it is a procedure that subdivides the image into its constituent parts or objects, called regions, using image attributes.

Region-based segmentation algorithms may be divided into three groups: Region Growing, Splitting and Merging and Watershed transform. However, only the first and the last ones were studied, since they are more suitable for our purpose.

4.3.3.1. Region Growing

The region algorithm, first proposed by Adam and Bischof (1994), is a procedure that groups pixels or sub-regions into larger regions based on predefined criteria for growth. The selection of similarity criteria relies on the problem to be solved and the type of available image data. Thus, they can be intensity, color, texture, shape, or size.

The fundamental steps involved in this algorithm are schematized in Figure 4.52. The region growing process starts with a seed point, which is manually or automatically selected, depending on the algorithm implemented. After that, the region grows by annexing to the

seed point those neighboring pixels that show similarity in a certain criterion, such as intensity. There are two important criteria that should be defined: intensity threshold and distance threshold. The process is iterated until it meets a stopping rule. Generally, the region growing should stop, when no more pixels satisfy the criteria for inclusion in that region.

The main advantage of this technique is its simple and easy implementation. However, since the basic algorithm includes manual selection of the seed point, it suffers from the manual initialization problem. The success of the region growing technique depends on the proper selection of this seed point.

Kroon (2009) implemented this algorithm in Matlab®, and it was used in this project to segment the test endoscopic image. However, it presents one significant difference when compared to the algorithm detailed in Figure 4.53. Instead of comparing the minimum difference intensity levels with a threshold, it always selects the neighbor pixel which has the intensity level closer to the region mean. Hence, the stop criterion is only based on a distance threshold, which could have different values, leading to different output images, as can be seen in Figure 4.52.

As the distance threshold value increases, more distant neighbours could be included, and, as such, the region becames larger (region in white). On the other hand, higher threshold values do not segment the region of interest so well. Hence, it should be made an equilibrium to obtain the object detected. Studying, in particular, the test endoscopic image, the ACF was not detected using different theshold values, since this technique is based on intensities, which is not a good approach, as has been concluded.
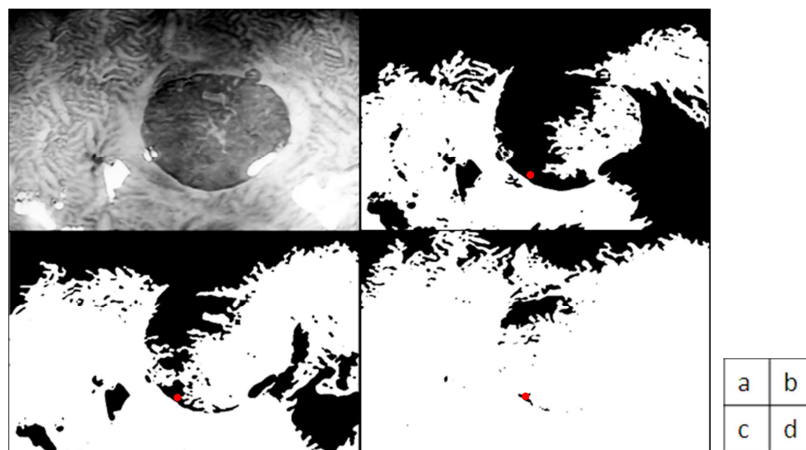
Figure 4.52 – Results of the region growing algorithm using the seed point in red and varying the threshold value: a) input image, b) threshold value of 0.2, c) 0.3, and d) 0.4.

Considering the segmentation results obtained, one could conclude that the region growing method was unsuitable to detect and segment the region of interest, that is, the ACF structure.
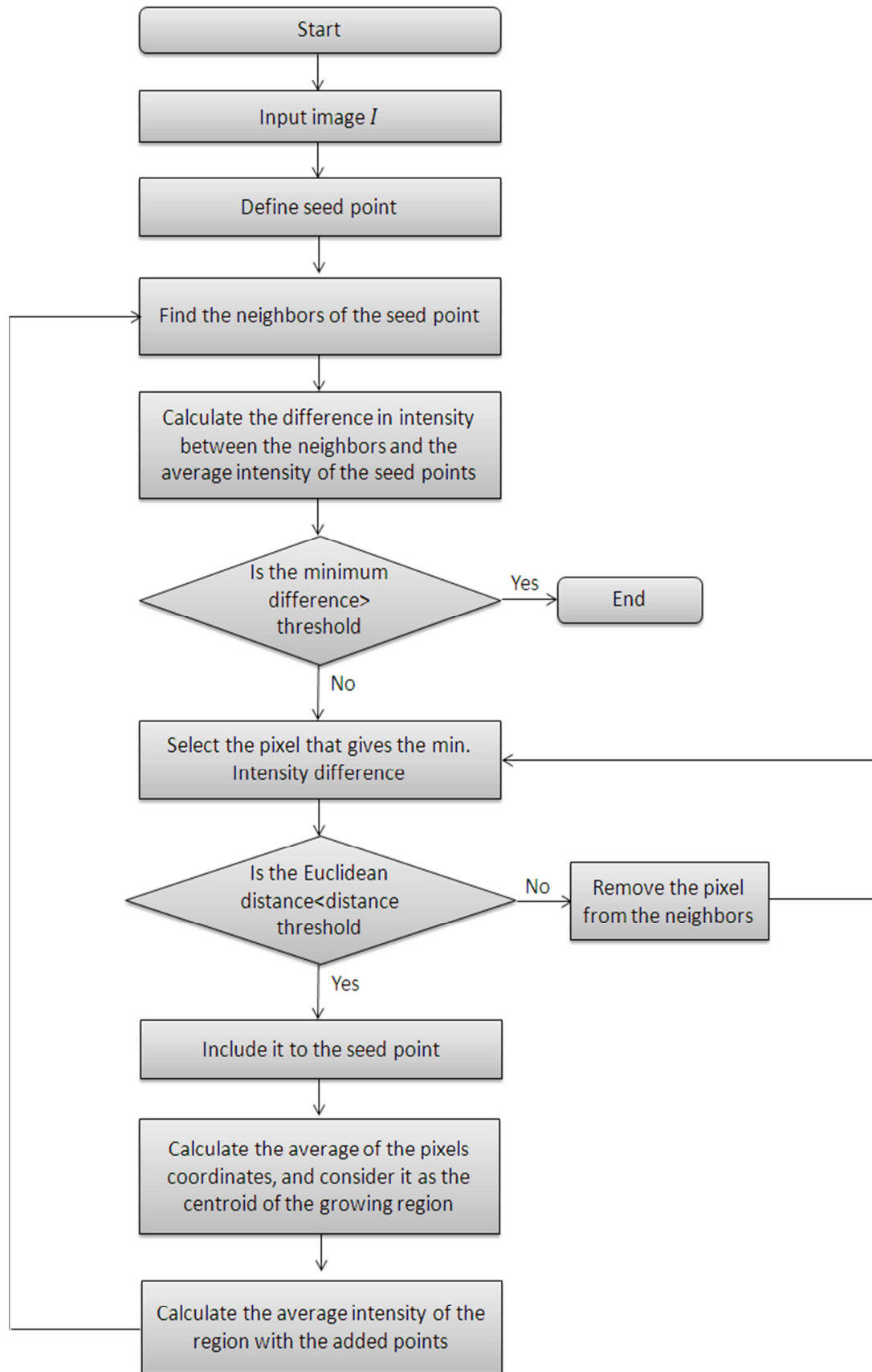
Figure 4.53 – Flowchart of the region growing algorithm used (adapted from (Wahba 2008)).

4.3.3.2. Watershed

In hydrology concepts, a watershed is an area of land that drains into a body of water, Figure 4.54. The boundaries of a watershed are defined by the points of highest elevation (designated in Figure 4.54 with a dotted line labeled divide).

Based on this natural environment found in nature, watershed segmentation based their technique considering an image in three dimensions, that is, two spatial coordinates and intensity. Then, it is considered three types of points:

- Points belonging to a regional minimum (river);
- Points at which a drop of water would fall with certainty to a single minimum (valley) – catchment basin;
- Points at which water would be equally likely to fall to more than one such minimum – watershed lines.
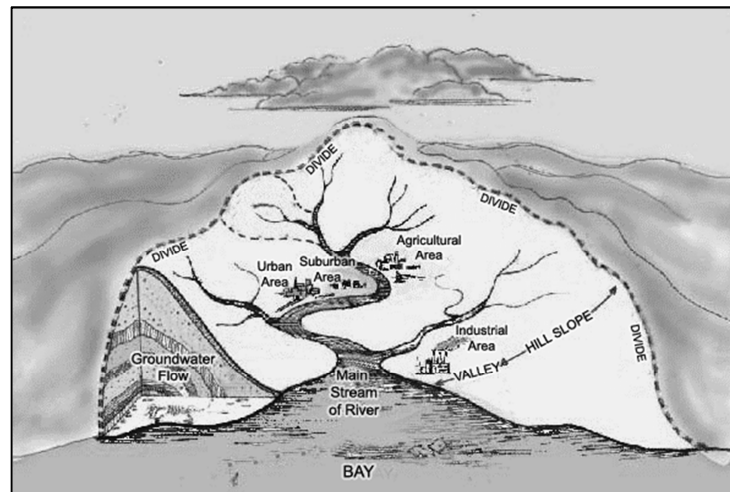
Figure 4.54 – Diagram of the watershed effect in hydrology studies (from (Foundation 2001)).

The main objective of this segmentation algorithm is to find watershed lines. Considering an image in 3D, where the height of the "mountains" is proportional to intensity values, the basic idea is that the image will be flooded from below by letting water rises through the holes at a uniform rate. When the rising water in distinct catchment basins is about to merge, a dam is built to prevent the merging. The flooding will eventually reach the watershed lines, when only dam boundaries will be visible, and they correspond to the boundaries extracted by the watershed segmentation algorithm.
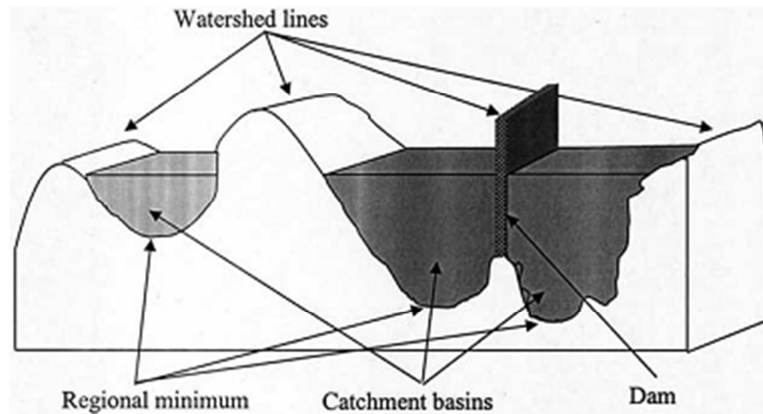
Figure 4.55 – Topographic view of watershed transformations (from (Huang and Chen 2004).

Watershed transformation is often applied on the gradient magnitude of an image in order to guide the watershed lines to follow the divide lines and the real boundaries of objects. It adopts the flooding process to simulate water flood, Figure 4.55. One of the most popular approaches was proposed by Vincent and Soille (1991), where watersheds are based on a morphological gradient, that is, gradient performance using mathematical morphologic operations. It includes two stages: sorting and flooding. The first step is based on pixel sorting in increasing order according to their gradient. At the flooding step, the pixels are accessed in increasing gradient order (immersion) using the sorted images and labels are assigned to catchment basins. However, there have been proposed many different approaches in what concerns to watershed segmentation, and those can be seen in (Roerdink and Meijster 2000).

Meyer (1994) suggested a watershed transform definition established on topographical distance and that was subject of study in this project. This algorithm is based on the successive flooding of the grey value relief, where watersheds with adjacent catchment basins are constructed. This flooding process is performed on the gradient image, i.e. the basins should emerge along the edges.

Considering a gray scale image $F(x)$, it is defined a set M of markers with different labels corresponding to the minimum values of $F(x)$, where the flooding should start. The fundamental steps are:

1. Each marker defined is labeled;
2. The neighboring pixels of each marked area are inserted into a priority queue with a priority level corresponding to the gray level of $F(x)$;
3. A pixel x with the highest priority level is extracted from the priority queue. If the neighbors of x, that have already been labeled, contains only points with the same

label, then x is marked with their label. All non-marked neighbors that are not yet marked are put into the priority queue;

4. Redo step 3 until the priority queue is empty.

The watershed lines set are the non-labeled pixels. This algorithm does neither label nor propagate watershed pixels, which "stop" the flooding. Thus, the watershed lines produced by Meyer's algorithm are always thinner than lines produced by other watershed algorithms (Najman and Couprie 2003).

The main disadvantage of these techniques described is over-segmentation. This happens when the image is partitioned into too many regions, that is, over-segmentation occurs because every regional minimum, even if tiny and insignificant, forms its own catchment basin.

Hence, a practical solution to this problem is to limit the number of allowable regions by incorporating a preprocessing stage. The usual approach used to control over-segmentation is the use of markers. A marker is a connected component belonging to an image and could be internal, when associated with objects of interest, or external when related to background.

This segmentation algorithm is included in the Matlab® image processing toolbox and is described in (Eddins). When the method was applied to the enhanced test endoscopic image, it results in over-segmentation, as was expected, Figure 4.56.
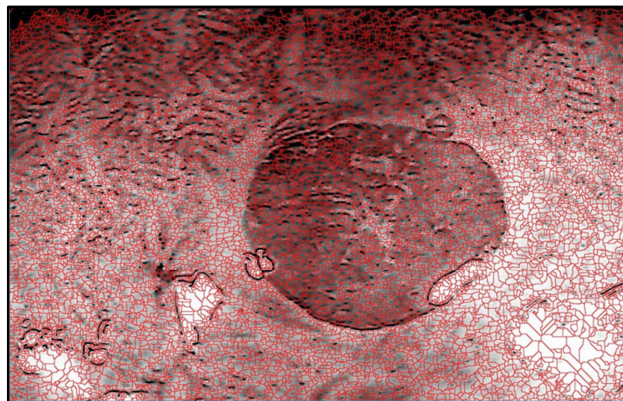
Figure 4.56 – Results of the wathershed algorithm on the enhanced test image.

To solve this problem, it was necessary to smooth the image, diminishing the variations of background and enhancing the edge of the ACF lesion, which will act as a marker to watershed. Hence, the image was smoothed using a median filter of size 10x10. Then, the ACF edge was identified using Sobel magnitude gradient image and a threshold of 0.12 was used to suppress minimum gradient values. Before using the watershed algorithm, the edges detected were eroded, to eliminate noise, and then dilated to link the edges, using a structuring

element with square shape and size 6 for erosion and 4 for dilation. Then, they were imposed as minimum values in the smoothed image, establishing the external markers. The result of watershed implementation after this preprocessing is represented in Figure 4.57.

Some experiments were made using Canny's edge detector instead of Sobel, and for this particular test image there was an improvement. However, when implemented in different test images, it did not work successfully. Hence, although Sobel operator detects some other regions in background, it demonstrates more homogeneity when used in different test endoscopic images.
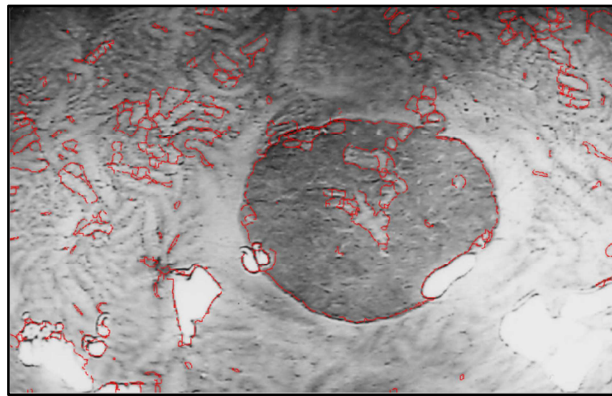
Figure 4.57 – Results of the Watershed algorithm after preprocessing the enhanced test image.

4.3.4. Comparison among the results of the segmentation algorithms on endoscopic images

Once again, the problematic of variance between endoscopic images is an essential and conditional characteristic to evaluate the capacity of each segmentation algorithm used. Hence, some methods experienced were not capable of successfully ACF segmentations. As such, each method with reasonable results were used on the three endoscopic images A, B and C shown in Figure 4.30 and also on the enhanced test images, Figure 4.36 (in gray scale) and Figure 4.37 (in the RGB domain).

4.3.4.1. Canny

The Canny's edge detector is very sensitive to high intensity noise, as concluded in the section 4.3.2.1. Hence, the use of this algorithm was performed on enhanced images after being smoothed by an additional double median filter with 10x10 window size. Furthermore,

the Canny's filter was used with a threshold of 0.2 and sigma 2 and the results obtained are presented in Figure 4.58.

The application of this algorithm to the three enhanced test images revealed that it was capable of detecting the boundary of ACF but it was not exclusive, i.e., the variations of image background were also pointed out by the Canny's detector. It is also important to refer that during the acquisition of endoscopic images the light is sometimes reflected in the liquid present in the colon. This reflection appears as light spots in the image, affecting the segmentation process, as can be seen in the images A and B from Figure 4.58.
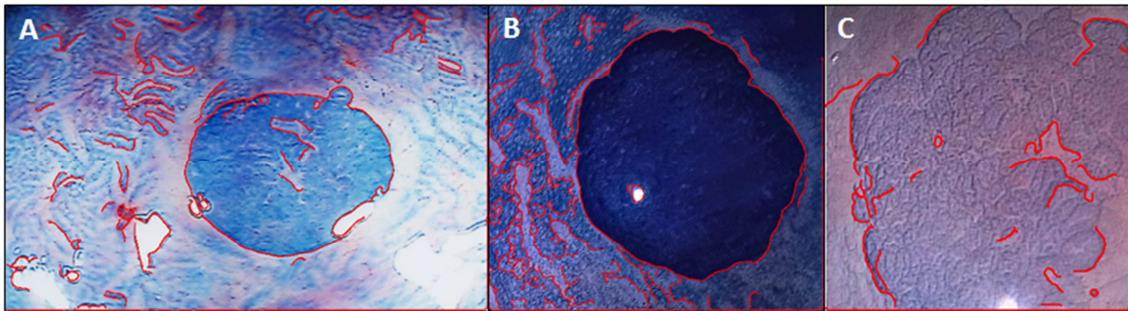
Figure 4.58 – Results of the Canny's edge detector applied on different test endoscopic images.

4.3.4.2. Snakes

The Snakes algorithm used depends on the initial contour, which is defined by the user. This is a disadvantage in the overall methods, since the process is not fully automatic. However, it could be useful to detect ACF boundaries and further extract features from these structures. This algorithm was applied to the same three images, but since the image C (from Figure 4.36) has the ACF edge in the limit of the image, the algorithm did not function successfully.
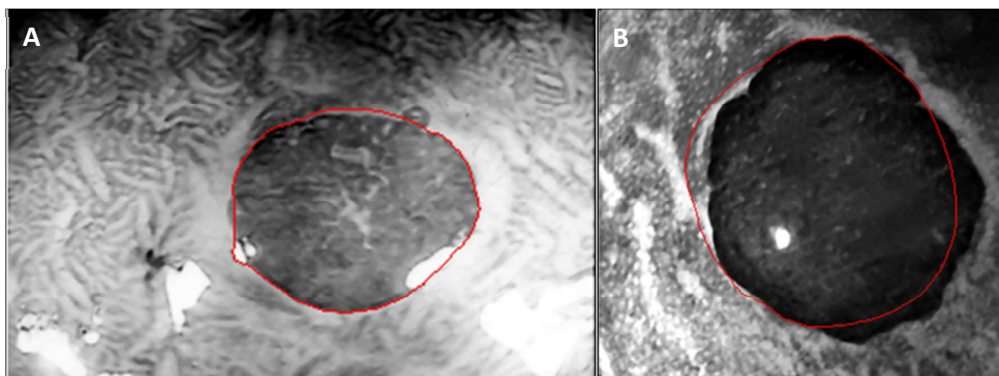
Figure 4.59 – Results of the Snake algorithm applied on two endoscopic images using the same parameters.

The best coefficient values chosen for image A, described in Table 4.3, were also used to find the contour of the AFC in image B, but the results (Figure 4.59) were not satisfactory since the contour did not stop at the AFC boundary.

4.3.4.3. Watershed

The Watershed algorithm was used after some preprocessing steps developed and implemented. The overall process can be described as:

1. Median filter of enhanced image using 10x10 window size;
2. Sobel filtering, calculating the magnitude gradient;
3. Thresholding of the Sobel magnitude with a threshold value of 0.12;
4. Morphological operation of erosion followed by dilation, using a structuring element of square shape and size 6 and 4, respectively;
5. Impose the binary image obtained as the minimum of the input image;
6. Watershed segmentation.

This image processing algorithm was applied on the three test endoscopic images and the results are represented in Figure 4.60.

Figure 4.60 – Results of the Watershed algorithm on three test endoscopic images.

Similar to what happened when the Canny's edge detector was used, the watershed algorithm was capable of detecting the ACF lesion, in particular, on the images A and B of Figure 4.59. However, the variations of image background were also identified, and, in the case of the image C of Figure 4.59, the segmentation was not so effective.

4.3.4.4. Chan and Vese ACWE

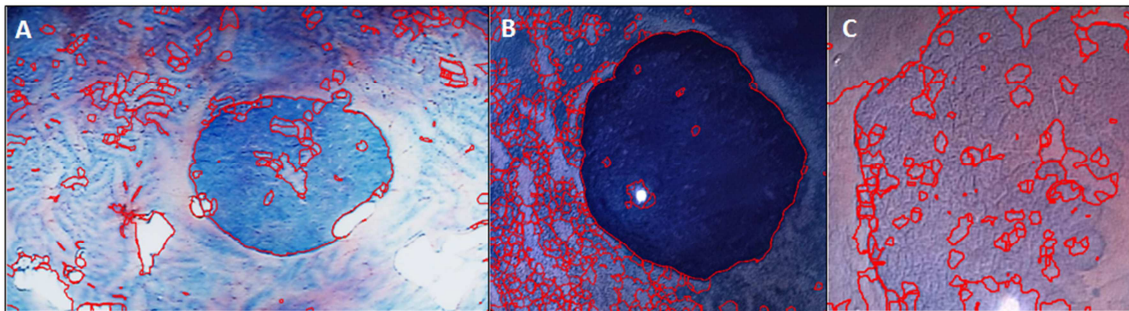The Chan and Vese model was also applied on the three test endoscopic images, and the results revealed poor segmentation, as can be seen in Figure 4.61, which was due to small differences between intensity levels of the image background and foreground.
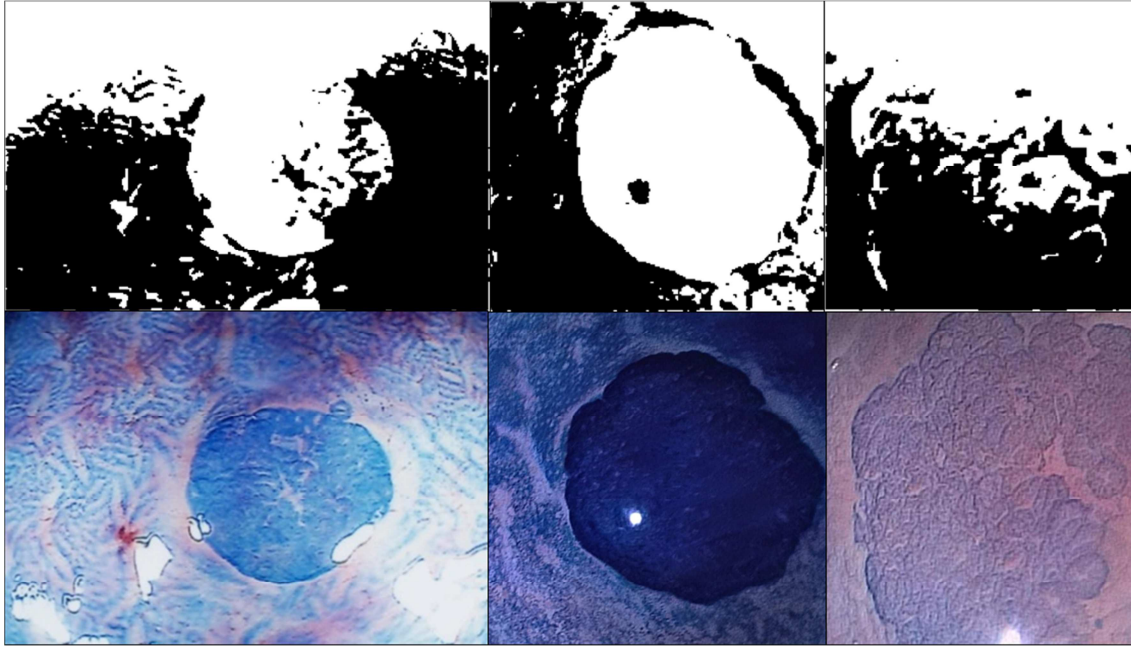
Figure 4.61 – Results of the Chan and Vese method on three endoscopic images, where the 1st row corresponds to the output images and the 2nd row represents the corresponding original images.

4.4. Conclusion

The processing of endoscopic images was divided into two fundamental steps: Enhancement and Segmentation. Each step can be composed by several algorithms that have been described in the literature. However, in this Dissertation, only those which are normally applied on medical images were studied.

From the methods used in image enhancement, the median filter and histogram stretching were the best options in order to achieve high intensity noise elimination and contrast enhancement from the endoscopic images tested. To take profit from the advantages of these two methods, it was proposed a hybrid algorithm. Since the original images were in the RGB domain, the processing was performed in gray scale and in the intensity matrix obtained from

conversion to HSI model. The results obtained had shown that when it is used the HSI model, the images processed had higher quality.

The second step used the enhanced image as input. From the algorithms tested, the Canny's edge detector, watershed and Snake algorithms were the best techniques capable of detecting the ACF boundary in the endoscopic images tested. However, the first two were affected by the background variation, and the Snake algorithm had important parameters that did not work well for all test endoscopic images.

Considering these results, it will be necessary to develop new algorithms based, or not, on these here described to accomplish the objectives proposed, that is, to obtain ACF lesion detection in endoscopic images.

Chapter 5

CONCLUSIONS AND FUTURE PERSPECTIVES

The colorectal cancer is a problematic disease which motivates several research projects in order to promote diagnosis, treatment and possibly cure. It has been suggested that the Aberrant Crypt Foci (ACF) could be a possible cancer precursor, and its early detection potentiates the treatment of this cancer type. Considering this, the aim of this dissertation was to study image processing algorithms that would be capable of automatic detection of these crypts, using endoscopic images. Thus, it would help physicians in their diagnosing process, which is usually slow. The image processing techniques include a first step of enhancement and posterior segmentation.

The purpose of image enhancement is to improve the quality of the original image. After implementing different algorithms, those who produced best results were median filtering and histogram stretching, since the first eliminate high intensity noise while the second enhances contrast. Thus, it was proposed a hybrid method which aggregates the advantages presented from the two methods.

As the first step was concluded, the purpose of image segmentation was to locate boundaries or objects of interest in the image. In this project, the aim was to detect the ACF from different endoscopic images and several approaches were explored and evaluated in order to highlight the present of these crypts from the image background. Although none of the methods proposed were able to achieve this aim fully successfully, the canny edge detector and the watershed transform were capable of detecting the ACF boundary, as well as other regions from the image background with no clinical relevance. Moreover, the active contour (snake) algorithm was able to define a final contour near the boundary, but it is very sensitive to parameter coefficients chosen.

Considering these results, it can be concluded that this dissertation introduces the first steps in the recent research field of ACF detection from endoscopic images. It was an initially attempt in the development of computational algorithms capable of efficient and robust ACF detection from different endoscopic images.

In the future, it would be interesting to apply color image segmentation algorithms, taking advantage from the color information present in endoscopic images. Thus, since the ACF are detected by methylene blue application to the colon, their blue intensity can potentiate the

segmentation process. Furthermore, after performing an optimization method to detect these crypts, it would be advantageous to extract features as texture and color to posteriorly classify the images and finish the automatic detection. Another approach is to continue the work performed by Figueiredo et. al (2010), in which the level sets method is being adjust to better identify the ACF lesions.

In the process of optimization, it will be relevant to consider more endoscopic images and the results of image segmentation should be validated by specialized medical doctors in order to verify if the detection was done correctly.

REFERENCES

Adams, R. and L. Bischof (1994). "Seeded region growing." Pattern Analysis and Machine Intelligence, IEEE Transactions on 16(6): 641-647.

Adler, D. G., C. J. Gostout, et al. (2002). "Endoscopic identification and quantification of aberrant crypt foci in the human colon." Gastrointestinal Endoscopy 56(5): 657-662.

Adler, D. G. and C. J. Goustout (2003). "Wireless capsule endoscopy." Hosp Physician 39(5): 14-22.

Ahmed, Q. (2008). Homomorphic Filtering. I. The Mathworks.

Akshay, K. G., P. Paul, et al. (2009). "Reliability and accuracy of the endoscopic appearance in the identification of aberrant crypt foci." Gastrointestinal endoscopy 70(2): 322-330.

Amerongen, H. M. (2010). Anatomy and Histology of the Digestive Tract. Comprehensive Toxicology. A. M. Charlene. Oxford, Elsevier: 3-15.

Badamchizadeh, M. A. and A. Aghagolzadeh (2004). Comparative study of unsharp masking methods for image enhancement. Image and Graphics, 2004. Proceedings. Third International Conference on.

Bae, U., V. Shamdasani, et al. (2003). "Fast adaptive unsharp masking with programmable mediaprocessors." J Digit Imaging 16(2): 230-239.

Baillie, J. (2007). "The endoscope." Gastrointestinal Endoscopy 65(6): 886-893.

Bansal, A., R. Bajpai, et al. (2007). Simulation of Image Enhancement Techniques Using Matlab. Modelling & Simulation, 2007. AMS '07. First Asia International Conference on.

Baopu, L. and M. Q. H. Meng (2007). Analysis of wireless capsule endoscopy images using chromaticity moments. Robotics and Biomimetics, 2007. ROBIO 2007. IEEE International Conference on.

Bird, R. P. (1987). "Observation and quantification of aberrant crypts in the murine colon treated with a colon carcinogen: Preliminary findings." Cancer Letters 37(2): 147-151.

Bird, R. P. (1995). "Role of aberrant crypt foci in understanding the pathogenesis of colon cancer." Cancer Letters 93(1): 55-71.

Bosco, J. J., A. N. Barkun, et al. (2003). "Gastrointestinal endoscopes: May 2003." Gastrointestinal Endoscopy 58(6): 822-830.

Canny, J. (1986). "A Computational Approach to Edge Detection." Pattern Analysis and Machine Intelligence, IEEE Transactions on PAMI-8(6): 679-698.

Carpi, F., S. Galbiati, et al. (2007). "Controlled Navigation of Endoscopic Capsules: Concept and Preliminary Experimental Investigations." Biomedical Engineering, IEEE Transactions on 54(11): 2028-2036.

Castleman, K. R. (1996). Digital Image Processing. New Jersey, Prentice Hall.

Chan, T. and L. Vese (1999). An Active Contour Model without Edges. Proceedings of the Second International Conference on Scale-Space Theories in Computer Vision, Springer-Verlag: 141-151.

Chan, T. F. and L. A. Vese (2001). "Active contours without edges." Image Processing, IEEE Transactions on 10(2): 266-277.

Cheng, H. D., X. H. Jiang, et al. (2001). "Color image segmentation: advances and prospects." Pattern Recognition 34(12): 2259-2281.

Davis, L. S. (1975). "A survey of edge detection techniques." Computer Graphics and Image Processing 4(3): 248-270.

Dias, R. A., J. H. Correia, et al. (2007). CMOS Optical Sensors for being incorporated in Endoscopic Capsule for Cancer Cells Detection. Industrial Electronics, 2007. ISIE 2007. IEEE International Symposium on.

Doucas, H. and D. P. Berry (2006). "Basic principles of the molecular biology of cancer I." Surgery (Oxford) 24(2): 43-47.

Eddins, S. "Strategies for Image Segmentation." Retrieved 24.June, 2011, from http://www.mathworks.com/company/newsletters/news_notes/win02/watershed.html.

Edwards, C. (1997). "Physiology of the colorectal barrier." Advanced Drug Delivery Reviews 28(2): 173-190.

Ellis, H. (2011). "Anatomy of the caecum, appendix and colon." Surgery (Oxford) 29(1): 1-4.

Eskicioglu, A. M. and P. S. Fisher (1995). "Image quality measures and their performance." Communications, IEEE Transactions on 43(12): 2959-2965.

Figueiredo, I. N., P. N. Figueiredo, et al. (2010). "Variational Image Segmentation for Endoscopic Human Colonic Aberrant Crypt Foci." Medical Imaging, IEEE Transactions on 29(4): 998-1011.

Figueiredo, P., M. Donato, et al. (2009). "Aberrant crypt foci: endoscopic assessment and cell kinetics characterization." International Journal of Colorectal Disease 24: 441-450.

Foundation, A. F. (2001). "What is a Watershed? Beyond the Definition." Retrieved 23.June, 2011, from http://www.fergusonfoundation.org/btw/watershed.shtml.

Fulmanski, P., A. Laurain, et al. (2008). "Level set method with topological derivatives in shape optimization." Int. J. Comput. Math. 85(10): 1491-1514.

Garg, R., B. Mittal, et al. (2011). "Histogram Equalization Techniques For Image Enhancement." International Journal of Electronics and Communication Technologies 2(1).

Gelas, A., O. Bernard, et al. (2007). "Compactly Supported Radial Basis Functions Based Collocation Method for Level-Set Evolution in Image Segmentation." Image Processing, IEEE Transactions on 16(7): 1873-1887.

Gonzalez, R. C. and R. E. Woods (2002). Digital Image Processing, Prentice Hall.

Gouveia, J., M. P. Coleman, et al. (2008). "Improving cancer control in the European Union: Conclusions from the Lisbon round-table under the Portuguese EU Presidency, 2007." European Journal of Cancer 44(10): 1457-1462.

Grady, W. M. (2004). Cancer, Overview. Encyclopedia of Gastroenterology. J. Leonard. New York, Elsevier: 256-264.

Harrington, K. J. (2008). "Biology of cancer." Medicine 36(1): 1-4.

Hawk, E. T., A. Umar, et al. (2004). "Colorectal cancer chemoprevention--an overview of the science." Gastroenterology 126(5): 1423-1447.

Horowitz, S. L. and T. Pavlidis (1974). "Picture segmentation by a directed split-and-merge procedure." Proceedings of the 2nd International Joint Conference on Pattern Recognition: 424-433.

Huang, Y.-L. and D.-R. Chen (2004). "Watershed segmentation for breast tumor in 2-D sonography." Ultrasound in Medicine & Biology 30(5): 625-632.

Iakovidis, D. K., S. Tsevas, et al. (2010). "Reduction of capsule endoscopy reading times by unsupervised image mining." Computerized Medical Imaging and Graphics 34(6): 471-478.

Iddan, G., G. Meron, et al. (2000). "Wireless capsule endoscopy." Nature 405(6785): 417-417.

Ivins, J. and J. Porrill (2000). Everything you always wanted to know about snakes (But were afraid to ask). England, University of Sheffield.

Jemal, A., R. Siegel, et al. (2008). "Cancer Statistics, 2008." CA Cancer J Clin 58(2): 71-96.

Jun, T. (2010). A color image segmentation algorithm based on region growing. Computer Engineering and Technology (ICCET), 2010 2nd International Conference on.

Junqueira, L. C. and J. Carneiro (2004). O Trato Digestivo. Histologia Básica. . Editora Guanabara Koogan S.A: 284-316.

Kass, M., A. Witkin, et al. (1988). "Snakes: Active contour models." International Journal of Computer Vision: 321-331.

Kida, M., K. Kobayashi, et al. (2003). "Routine chromoendoscopy for gastrointestinal diseases: indications revised." Endoscopy 35(7): 590-596.

Kovesi, P. (2008). "MATLAB and Octave Functions for Computer Vision and Image Processing." Retrieved 25.June, 2011, from http://www.csse.uwa.edu.au/~pk/research/matlabfns/.

Krishnan, S. M. and P. M. Y. Goh (1997). Quantitative parametrization of colonoscopic images by applying fuzzy technique. Engineering in Medicine and Biology Society, 1997. Proceedings of the 19th Annual International Conference of the IEEE.

Krishnan, S. M., Y. Xin, et al. (1999). Region labeling of colonoscopic images using fuzzy logic. [Engineering in Medicine and Biology, 1999. 21st Annual Conf. and the 1999 Annual Fall Meeting of the Biomedical Engineering Soc.] BMES/EMBS Conference, 1999. Proceedings of the First Joint.

Kroon, D.-J. (2009). Region Growing. I. The Mathworks.

Kumar, R. (2010). Snakes: Active Contour Models. I. The Mathworks.

Labianca, R., G. Beretta, et al. (2004). "Colon cancer." Critical Reviews in Oncology/Hematology 51(2): 145-170.

Liedlgruber, M. and A. Uhl (2009). Endoscopic image processing - an overview. Image and Signal Processing and Analysis, 2009. ISPA 2009. Proceedings of 6th International Symposium on.

Limburg, P. J. and D. A. Ahlquist (2004). Colorectal Adenocarcinoma. Encyclopedia of Gastroenterology. J. Leonard. New York, Elsevier: 457-466.

Ma, Z., J. M. R. S. Tavares, et al. (2009). "A review of algorithms for medical image segmentation and their applications to the female pelvic cavity." Computer Methods in Biomechanics and Biomedical Engineering.

MacFarlane, A. J. and P. J. Stover (2008). Gastrointestinal Disorders: Overview. International Encyclopedia of Public Health. H. Kris. Oxford, Academic Press: 9-19.

Mackiewicz, M., J. Berens, et al. (2008). "Wireless Capsule Endoscopy Color Video Segmentation." Medical Imaging, IEEE Transactions on 27(12): 1769-1781.

Maini, R. and H. Aggarwal (2010). "A Comprehensive Review of Image Enhancement Techniques." Journal of Computing 2(3).

Mathworks. (2011). "Morphology Fundamentals: Dilation and Erosion." Retrieved 17.June, 2011, from http://www.mathworks.com/help/toolbox/images/f18-12508.html.

Mazzucchelli, L. and C. Maurer (2004). Colon, Anatomy. Encyclopedia of Gastroenterology. J. Leonard. New York, Elsevier: 408-412.

McInerney, T. and D. Terzopoulos (1996). "Deformable models in medical image analysis: a survey." Medical Image Analysis 1(2): 91-108.

Meyer, F. (1994). "Topographic distance and watershed lines." Signal Processing 38(1): 113-125.

Michel, D. and G. Gérard (2008). "Capsule endoscopy: Technique and indications." Best practice & research. Clinical gastroenterology 22(5): 813-837.

Mishkin, D. S., R. Chuttani, et al. (2006). "ASGE Technology Status Evaluation Report: wireless capsule endoscopy." Gastrointest Endosc 63(4): 539-545.

Mitry, E. (2008). Colorectal Cancer. International Encyclopedia of Public Health. H. Kris. Oxford, Academic Press: 765-772.

Moreira Jr, H. and S. D. Wexner (2005). ANATOMY AND PHYSIOLOGY OF THE COLON AND RECTUM. Current Therapy in Colon and Rectal Surgery (Second Edition). W. F. Victor, Mb, Mset al. Philadelphia, Mosby: 113-123.

Mori, H., Y. Yamada, et al. (2004). "Aberrant crypt foci and [beta]-catenin accumulated crypts; significance and roles for colorectal carcinogenesis." Mutation Research/Reviews in Mutation Research 566(3): 191-208.

Mumford, D. p. and J. p. Shah (1989). "Optimal approximations by piecewise smooth functions and associated variational problems\par." Communications on Pure and Applied Mathematics\par 42\par(5\par): 577\par-685\par.

Najman, L. and M. Couprie (2003). Watershed Algorithms and Contrast Preservation. Discrete Geometry for Computer Imagery: 62-71.

Natalin, R. A. and J. Landman (2009). "Where next for the endoscope?" Nat Rev Urol 6(11): 622-628.

Nucci, M. R., C. R. Robinson, et al. (1997). "Phenotypic and genotypic characteristics of aberrant crypt foci in human colorectal mucosa." Human pathology 28(12): 1396-1407.

Osher, S. and J. A. Sethian (1988). "Fronts propagating with curvature-dependent speed: Algorithms based on Hamilton-Jacobi formulations." Journal of Computational Physics 79(1): 12-49.

Otsu (1979). "A Threshold Selection Method from Gray-Level Histograms." Systems, Man and Cybernetics, IEEE Transactions on 9(1): 62-66.

Pinto, C., A. Paquete, et al. (2010). "Colorectal cancer in Portugal." The European Journal of Health Economics 10(0): 65-73.

Pitas, I. (1993). State of the art of morphological and nonlinear digital image processing. Morphological and Nonlinear Image Processing Techniques, IEE Colloquium on.

Pizer, S. M., E. P. Amburn, et al. (1987). "Adaptive histogram equalization and its variations." Computer Vision, Graphics, and Image Processing 39(3): 355-368.

Pizer, S. M., R. E. Johnston, et al. (1990). Contrast-limited adaptive histogram equalization: speed and effectiveness. Visualization in Biomedical Computing, 1990., Proceedings of the First Conference on.

Polesel, A., G. Ramponi, et al. (1997). Adaptive unsharp masking for contrast enhancement. Image Processing, 1997. Proceedings., International Conference on.

Porrett, T. and A. McGrath (2005). Anatomy and Physiology of the Bowel and Urinary Systems. Stoma Care. B. Publishing, Wiley-Blackwell: 1-16.

Pretlow, T. P., B. J. Barrow, et al. (1991). "Aberrant Crypts: Putative Preneoplastic Foci in Human Colonic Mucosa." Cancer Research 51(5): 1564-1567.

Rangayyan, R. M. (2005). Biomedical Image Analysis. Canada, CRC Press.

Reza, A. M. (2004). "Realization of the Contrast Limited Adaptive Histogram Equalization (CLAHE) for Real-Time Image Enhancement." The Journal of VLSI Signal Processing 38(1): 35-44.

Roerdink, J. B. T. M. and A. Meijster (2000). "The watershed transform: definitions, algorithms and parallelization strategies." Fundam. Inf. 41(1-2): 187-228.

Roncucci, L., S. Modica, et al. (1998). "Aberrant crypt foci in patients with colorectal cancer." British journal of cancer 77(12): 2343-2348.

Rudolph, R. E., J. A. Dominitz, et al. (2005). "Risk Factors for Colorectal Cancer in Relation to Number and Size of Aberrant Crypt Foci in Humans." Cancer Epidemiology Biomarkers & Prevention 14(3): 605-608.

Russ, J. C. (2002). The Image Processing Handbook, CRC Press.

Sakuldee, R. and S. Udomhunsakul (2008). Objective measurements of distorted image quality evaluation. Computer and Communication Engineering, 2008. ICCCE 2008. International Conference on.

Schoen, R. E., M. Mutch, et al. (2008). "The natural history of aberrant crypt foci." Gastrointestinal endoscopy 67(7): 1097-1102.

Schonfeld, D. (1991). Morphological processing of medical images: an introduction. Circuits and Systems, 1991., IEEE International Sympoisum on.

Schwartz, J. J. and G. R. Lichtenstein (2004). "Magnification endoscopy, chromoendoscopy and other novel techniques in evaluation of patients with IBD." Techniques in Gastrointestinal Endoscopy 6(4): 182-188.

Shpitz, B., Y. Bomstein, et al. (1998). "Aberrant crypt foci in human colons: distribution and histomorphologic characteristics." Human pathology 29(5): 469-475.

Sternberg, S. R. (1983). "Biomedical Image Processing." Computer 16(1): 22-34.

Stevens, R. G., H. Swede, et al. (2007). "Aberrant crypt foci in patients with a positive family history of sporadic colorectal cancer." Cancer letters 248(2): 262-268.

Swain, P. (2003). "Wireless capsule endoscopy." Gut 52(Suppl 4): iv48-iv50.

Takayama, T., S. Katsuki, et al. (1998). "Aberrant Crypt Foci of the Colon as Precursors of Adenoma and Cancer." New England Journal of Medicine 339(18): 1277-1284.

Tjoa, M. P., S. M. Krishnan, et al. (2002). Automated diagnosis for segmentation of colonoscopic images using chromatic features. Electrical and Computer Engineering, 2002. IEEE CCECE 2002. Canadian Conference on.

Vincent, L. and P. Soille (1991). "Watersheds in digital spaces: an efficient algorithm based on immersion simulations." Pattern Analysis and Machine Intelligence, IEEE Transactions on 13(6): 583-598.

Wahba, M. (2008). An Automated Modified Region Growing Technique for Prostate Segmentation in Trans-Rectal Ultrasound Image. Ontario, Canada, University of Waterloo. Master of Applied Science in Electrical and Computer Engineering.

Wang, P., S. M. Krishnan, et al. (2002). An adaptive segmentation technique for clinical endoscopic image processing. Engineering in Medicine and Biology, 2002. 24th Annual Conference and the Annual Fall Meeting of the Biomedical Engineering Society EMBS/BMES Conference, 2002. Proceedings of the Second Joint.

Wang, R. (2009). "Digital Convolution -- E186 Handout." Retrieved 16.June, 2011, from http://fourier.eng.hmc.edu/e161/lectures/convolution/index.html.

Wang, S. Y., K. M. Lim, et al. (2007). "A Geometric Deformation Constrained Level Set Method for Structural Shape and Topology Optimization." Computer Modeling in Engineering & Sciences 18(3): 155-182.

Wang, X.-F., D.-S. Huang, et al. (2010). "An efficient local Chan-Vese model for image segmentation." Pattern Recognition 43(3): 603-618.

Wellner, P. D. (1993). Adaptive Thresholding for the Digital Desk. R. X. Ltd. Cambridge, Rank Xerox Research Centre.

Widmaier, E. P., H. Raff, et al. (2004). Vander, Sherman, Luciano's Human Physiology: The Mechanisms of Body Function, The McGraw-Hill Companies, Inc.

Williams, D. J. and M. Shah (1992). "A fast algorithm for active contours and curvature estimation." CVGIP: Image Underst. 55(1): 14-26.

Wu, Y. (2009). Chan Vese Active Contours without edges. I. The Mathworks.

Yeganeh, H., A. Ziaei, et al. (2008). A novel approach for contrast enhancement based on Histogram Equalization. Computer and Communication Engineering, 2008. ICCCE 2008. International Conference on.

Yu, J. and J. Tan (2009). "Object density-based image segmentation and its applications in biomedical image analysis." Computer Methods and Programs in Biomedicine 96(3): 193-204.

Zuiderveld, K. (1994). Contrast Limited Adaptive Histograph Equalization. Graphic Gems IV, San Diego: Academic Press Professional: 474-485.